



ACADEMIC
PLATFORM

e-ISSN: 2717-8714

APJHAD

Academic Platform

Journal of Natural Hazards

And Disaster Management

Volume: 1

Issue: 2

December 2020

**Academic Platform Journal of Natural Hazards and Disaster Management
(APJHAD) Editorial Boards**

Editor-in-Chief

Prof. Dr. Naci ÇAĞLAR, Sakarya University, Turkey

Associate Editors

Asst. Prof. Dr. Abdulkadir ÖZDEN, Sakarya University of Applied Sciences, Turkey

Editors

Asst. Prof. Dr. A. Can ZÜLFİKAR, Gebze Technical University, Turkey

Dr. Ana Mafalda MATOS, University of Porto, Portugal

Assoc. Prof. Dr. Ertan BOL, Sakarya University, Turkey

Asst. Prof. Dr. Beytullah EREN, Sakarya University, Turkey

Prof. Dr. Hasan ARMAN, United Arab Emirates University, United Arab Emirates

Asst. Prof. Dr. İlyas SARIBAŞ, Alparslan Türkeş University of Science and Technology, Turkey

Assoc. Prof. Dr. Junwon SEO, South Dakota State University, United States

Prof. Dr. Murat PALA, ADIYAMAN UNIVERSITY, Turkey

Assoc. Prof. Dr. Mehmet İshak YÜCE, Gaziantep University, Turkey

Asst. Prof. Dr. Matteo PICOZZI, Università degli Studi di Napoli 'Federico II, Italy

Assoc. Prof. Dr. Neritan SHKODRANI, Polytechnic University of Tirana, Albania

Prof. Dr. Osamu TAKAHASHI, Tokyo University of Science, Japan

Dr. Tuba TATAR, Sakarya University, Turkey

Dr. Nikolaos THEODOULIDIS, Institute of Engineering Seismology and Earthquake Engineering
Research and Technical Institute, Greece

English Language Editor

Asst. Prof. Dr. Hakan ASLAN, Sakarya University, Turkey

Technical Editor

Asst. Prof. Dr. Caner ERDEN, Sakarya University of Applied Sciences, Turkey

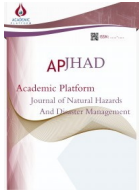
Academic Platform Journal of Natural Hazards and Disaster Management (APJHAD)

Volume 1 Issue 2 December 2020

Contents


Research Articles


Title	Authors	Pages	
Teleseismic Source Process of The October 30, 2020 Kuşadası Gulf – İzmir (Turkey) Earthquake (Mw=6.8)	Murat Utkucu, Emrah Budakoğlu, Şefik Ramazanoğlu	66	73
Research of Seismic Brace Using Aramid Fiber Rope to Retrofit Building	Yuho Inoue, Osamu Takahashi	74	88
Sight Distance on Road Safety According Albanian Code	Iralda Xhaferaj, Neritan Shkodrani	89	95
Urban Mobility In Covid-19: How We Adapted to Change and How Should We Respond	Abdulkadir Özden, Süleyman Nurullah Adahi Şahin	96	109
Review Articles			
Review: Understanding of Natural Disaster Risk Management and Where Turkey Stands in the Picture	Tuba Tatar	110	121




Research on the Development of the Semi-Rigid Column Base of Reinforced Concrete: Experimental and Analytical Study on the Column Base with Cross Section Reduced Portion

Osamu Takahashi^{1*}, Hirona Yoshida², Minoru Od³

¹ Tokyo University of Science, 6-3-1, Nijuku, Katsushika-ku, Tokyo 125-8585, Japan 

² Tokyo University of Science, Nijuku, Katsushika-ku, Tokyo 125-8585, Japan 

³ Sumitomo Mitsui Construction Co., Ltd., Japan 

Received: / Accepted: 03.05.2020/05.06.2020

Abstract

Generally, in reinforced concrete buildings, joints have been planned as a rigid state due to the characteristics of their construction. In such a building, the stress of the first story column becomes nonuniform since the bending stress at the time of the earthquake is concentrated on the rigid joints of the foundation structure such as the column base at the first story. This paper proposed making the column base at the first story shape semi-rigid to reduce the stress concentrating on the column base at the first story. In order to realize semi-rigid column base, we performed structural experiments and FEM analysis on the column base with cross section reduced portion. As a result, it was concluded that the best structure shape is one with the cross section reduced portion and the taper at the column base as the semi-rigid column base with bending rigidity reduction and structural performance stability.

Key words: Reinforced concrete, column, semi-rigid, bending rigidity, burst stress

1. Introduction

1.1. Background

In order to design a structure rationally, it is desirable to have a frame that avoids localized collapse and concentration of deformation and resists well in balance over the building. The stress state of the structure subject to external force depends mainly on the rigidity of the member in the minute deformation region and the strength of the member in the large one. Since ordinary RC buildings adjust the cross-section area and the amount of reinforcement as members such as columns and beams against the existing stress, the rigidity and strength cannot be changed easily. If the rigidity and the strength of each member can be easily changed, it can be possible to design the building in a more rational stress state.

As a previous study carried out with such a purpose, there is the research ^[1] to make the connections of pile head semi-rigid. In the semi-rigid pile head method, the bending stress generated in the pile is equalized with respect to the entire pile by reducing the pile head rigidity,

* Corresponding Author,
e-mail: o.taka@rs.tus.ac.jp

realizing improvement in functionality and economical design. Here we develop the RC columns realizing a reasonable RC building by focusing on the 1st column of RC structure, controlling the bending stress state of it by reducing the column base rigidity.

1.2. Overview of Construction

Fig. 1 shows overview of this construction method. We compare the case of the ordinary column base, the case with semi-rigid spring and the case of actually designing it about the 1st column. In a high-rise building or the like, of the bending stress exists considerably on the column top. If a semi-rigid spring is provided on the column base without changing the shear force for design, the inflection point goes down and the bending stress of the column top and the column base approaches each other. However, from the viewpoint of seismic safety of the structure, it is necessary that as the actual semi-rigid detail, the strength of the column base does not decrease excessively.

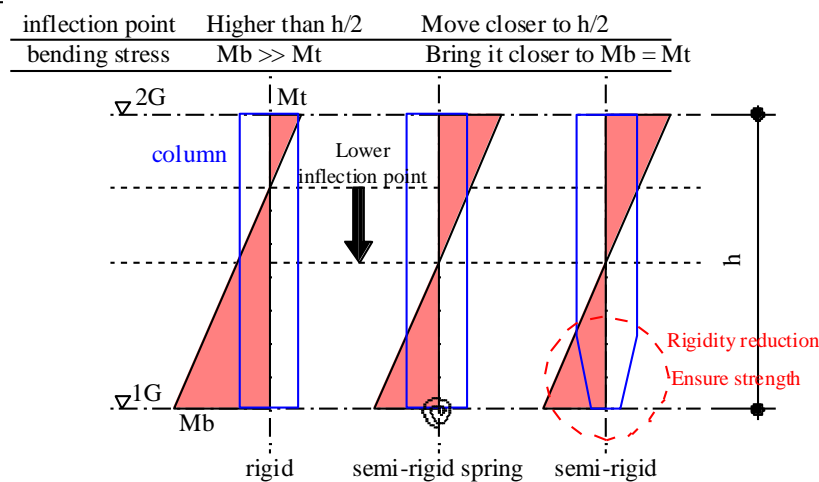


Figure 1. Overview of this construction

Fig. 2 shows an example of a stress diagram when the column base is rigid and semi-rigid. As in this example, when the height of the inflection point is fairly high, the bending stress of the column base is reduced by about 27% by the semi-rigid spring with the rigidity of 0.5. In actual design, stress reduction of 27% produces a significant difference on the reinforcement.

Fig. 3 shows the problems with previous columns. In the case where the inflection point is high and the column bending stress is large, there are roughly two ways to deal with it. From the figure, the case 1 is to change the cross section of the column against the existing stress on the first and second floors. In this case, a cross section switching part is required in the connection of column and beam on the second floor, so the reinforcement details become complicated. Thus, problems in construction tend to occur. The case 2 is to make the cross section of the column on the first floor and the second floor same. In this case, in order to cope with the existing stress, it is necessary to increase the amount of the reinforcing of the 1st column base, which makes it difficult to secure the main reinforcement interval and the like. For avoiding this problem, the cross-section area must be increased. In this construction method, the cross-section area of the column base is reduced and high strength concrete or the like is used, thereby reducing the rigidity of the column without excessively reducing strength.

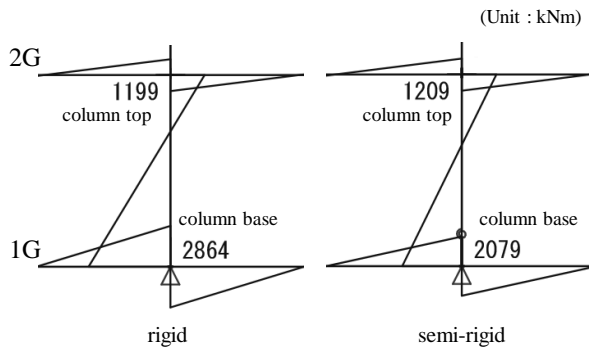


Figure 2. Example of bending stress diagram

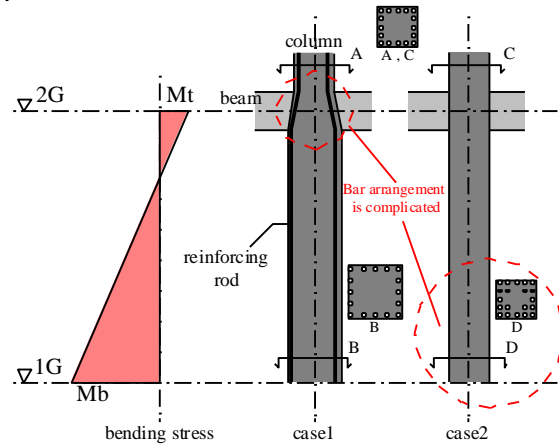


Figure 3. Problems of rigid columns

1.3. Effective scope

In order to understand the effective building with this construction method, elasticity analysis of the frame model was performed when the height and length of the building were changed, and the inflection point ratio of the representative intermediate column on the first floor was calculated.

Fig. 4 shows the relationship between the aspect ratio of each building and the inflection point ratio of the representative intermediate column on the first floor. Also, in the figure, the values of the actual design projects are plotted. The case where the inflection point ratio shows 0.5 is the case where the bending stress of the column top and the column base are equal, and all the analysis results are the inflection point ratio of 0.5 or more.

From the figure, there is a positive correlation between the aspect ratio and the inflection point ratio, and as the aspect ratio increases, the inflection point tends to rise. A similar tendency is seen also in the actual design example, and this construction method can be effectively applied to buildings with large aspect ratio and large influence of overall bending deformation. Especially, when the aspect ratio is 1.0 or more, the ratio of the inflection point ratio is about 0.75 or more, so the usefulness of this construction method is likely to be high.

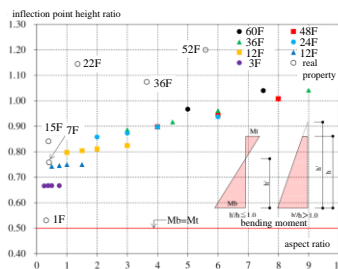


Figure 4. Relationship between aspect ratio and inflection point ratio

2. Experimental Study on RC Columns with Reduced Cross Section

In order to obtain the effect of reducing the rotational rigidity of the column base, a column specimen with a reduced part at the base was prepared and a bending shear experiment was conducted.

2.1. Specimen and method

Fig. 5 shows the specimen diagram and loading method, Table 1 the specimen list, and Table 2 shows the material test results. The specimen consists of a total of five bodies, a general column No. 1 having the same cross section in the axial direction, and columns No. 2 to 5 having a reduced part in the base. All the specimens were planned so that bending yield would precede.

In No. 2, there are two pairs of shear reinforcement (D6, SHD685), No. 3 and No. 5 steel pipes (STKR400, t=9mm) on the outer circumference of the reduced part, No. 4 steel plates (SS400, t=19mm) as two sheets. Here the high strength grout (Fc100) was filled in No. 2 itself, the steel pipe of No. 3 and 5, the lower surface of steel plate of No. 4 and the main reinforcement hole. In No. 5, the adhesion of the main reinforcement fixed in the column part was removed 300 mm by using a vinyl tube, thereby further reducing the rotational rigidity.

Table 3 shows the force cycle. The force was given a constant vertical force corresponding to the axial force ratio of 0.25 in the column part to the top, and positive and negative alternating loading was performed in the horizontal direction according to the loading cycle shown in the table.

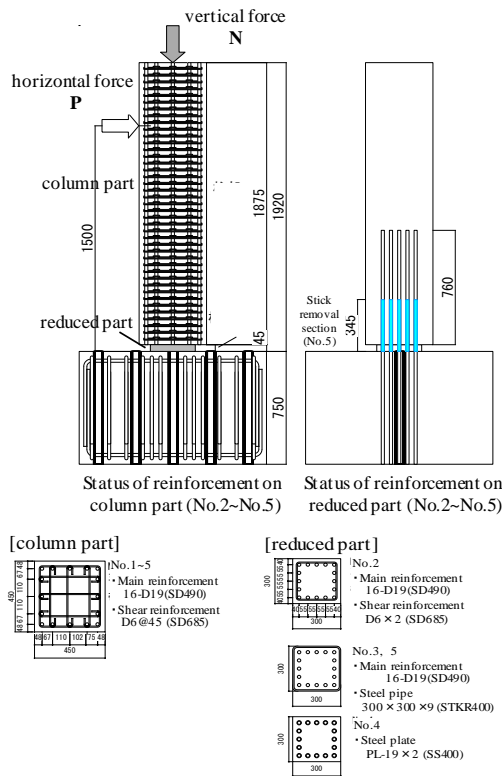


Figure 5. Specimen diagram and Loading method

2.2. Result and discussion

Fig. 6 shows the column base cracks of No. 1 and 3, Fig. 7 left shows the shear force - deformation angle relationship (considering the P-Δ effect) of No. 3 and the envelope of the shear force - deformation angle relationship of all specimens (considering the P-Δ effect), and Table 4 shows experimental result and calculated value of strength. Bending yield was preceded in all specimens and showed stable hysteretic properties until about 1/18 rad of large deformation. In the following, the experimental process of each specimen will be described.

Table 1. List of specimens

specimen	cross section B × D (mm)	concrete strength Fc (N/mm ²)	column part reinforcement		axial force ratio η
			main p _c (%)	shear p _v (%)	
No.1					0.25
No.2	450	60	16-D19 (SD490)	5-D6@45 (SHD685)	N
No.3	×				N
No.4	450		p _c =2.16	p _v =0.79	B × D × σ _c / σ _B
No.5					

specimen	cross section Br × Dr (mm)	concrete strength g Fc (N/mm ²)	reduced part reinforcement		constitution of cross section
			main p _c (%)	method	
No.1	—	—	—	—	—
No.2	300	100	16-D19 (SD490)	2-D6 × 2 (SHD685)	grout
No.3	×			300 × 300 × 9 (STKR400)	steel pipe
No.4	300			PL-19 × 2 (SS400)	steel plate
No.5				300 × 300 × 9 (STKR400)	steel pipe + stick removal section

Table 2. Material test results

part	type material	yield point (N/mm ²)	yield strain (× 10 ⁻⁶)	elastic coefficient (× 10 ⁴ N/mm ²)
main reinforcement	D19 (SD490)	540	3182	1.93
shear reinforcement	D6 (SHD685)	745	5957	1.90
steel pipe	PL9 (STKR400)	391	3750	2.06

type material	compressive stress (N/mm ²)	bursting stress (N/mm ²)	elastic coefficient (× 10 ⁴ N/mm ²)
concrete	57.7	3.05	3.53
grout	117.5	3.35	4.81

Table 3. Force cycle

R(rad)	Cycle
1/800	±2
1/400	±2
1/200	±2
1/100	±2
1/50	±2
1/25	±1

In No. 1, bending cracks (①) at the column base at $1/400$ rad, shear cracks (②) $1/2 D$ (D : column part vertical width) away from the dangerous cross section position at $1/200$ rad, and lengthwise cracks (③) in the corner occurred. After that, rigidity declined, and the main reinforcement compression yielded at $1/50$ rad and the load became almost constant. In No. 3 using a steel pipe in the reduced part, lengthwise cracks (①) occurred at the center position of the lower in the column part at $1/200$ rad, the main reinforcement compression yielded at $1/100$ rad, then width cracking occurred, rigidity beginning to decline, and as the main reinforcement tension yielded at $1/50$ rad, the load became almost constant. Lengthwise cracks (①) occurred in all specimens with reduced part.

Fig. 7 right shows the initial rigidity (evaluation at $1/800$ rad from the origin) of each specimen. The rigidity reduction effect of the specimens No. 2 to 5 with the reduced part was about 54 to 69%. Among them, the rigidity reduction effect of No. 5 without the adhesion was 54%, which was larger than the other specimens.

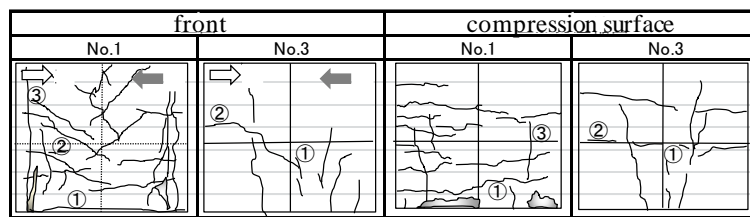


Figure 6. Crack of the column base

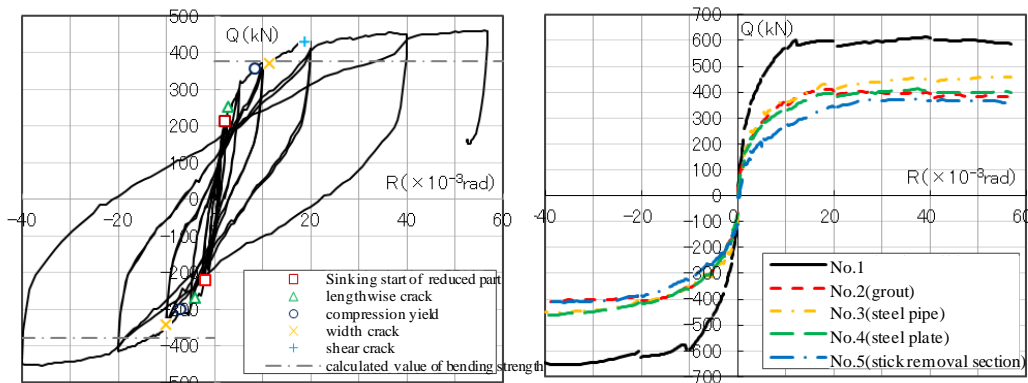


Figure 7. Shear force – deformation angle relationship (left: No.3, right: envelope)

Fig. 8 shows the transition of axial deformation. Axial deformation is the vertical displacement on the displacement meter placed at a height of 1500 mm from the base. In all specimens, axial deformation tended to increase due to the progress of the deformation angle and repetition with the same deformation after $1/100$ rad. Increase in axial deformation from the elastic state before given horizontal force to the end of $1/50$ rad was 0.54 mm (No. 1), 0.70 mm (No. 2), 1.04 mm (No. 3), 1.04 mm (No. 4), 0.87 mm (No. 5). From these values, in particularly No. 3 to 5 using a steel for the reduced part were larger than No. 1, which seemed to be contributed to the local crash at the contact between the steel and the concrete. In addition, lengthwise cracks generated in all specimens with reduced parts were due to tensile stress orthogonal to the local compressive stress, which confirmed this fact.

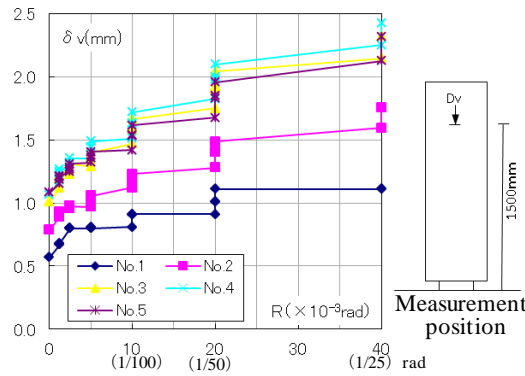


Figure 8. Transition of axial deformation

Table 4. Experimental result and calculated value of strength

specimen	crack										yield main reinforcement				maximum strength				calculated value			
	bending (+)		bending (-)		shear (+)		shear (-)		lengthwise (+)		lengthwise (-)		compressive (+)		compressive (-)		(+)	(-)	bending	she		
	Q (kN)	R (rad)	Q (kN)	R (rad)	Q (kN)	R (rad)	Q (kN)	R (rad)	Q (kN)	R (rad)	Q (kN)	R (rad)	Q (kN)	R (rad)	Q (kN)	R (rad)	Q (kN)	R (rad)	cQmu (kN)	cQsu		
No.1	272	1.5	-288	-1.7	453	5.0	-403	-3.8	567	9.4	-542	-8.7	581	12.5	-582	-12.0	614	39.4	-652	-35.4	576	91
No.2	170	1.5	-166	-1.3	—	—	-407	-20.0	350	8.7	-328	-7.7	359	10.0	-354	-10.0	411	19.0	-412	-38.7	377	
No.3	—	—	—	—	429	18.7	-451	-38.0	251	2.9	-270	-4.0	356	8.4	-300	-7.0	460	56.1	-453	-36.0	377	
No.4	—	—	—	—	376	14.7	-414	-18.4	173	1.7	-175	-1.7	319	8.3	-301	-7.3	413	37.4	-461	-38.0	377	
No.5	—	—	—	—	—	—	—	—	122	1.6	-182	-1.6	370	25.4	-397	-24.0	376	36.1	-412	-40.0	377	

※1 : R (× 10⁻³) ※2 : (+)Positive force , (-)Negative force ※3 : lengthwise cracks of No. 1 are co

3. Analytical Study on Internal Stress

We describe the result of FEM analysis for the purpose of clarifying the cause of lengthwise cracks which was the subject of the experiment. Among the specimens mentioned in Chapter 2, one of the subject was the general column (No. 1) and the other had a reduced part in the column base (No. 2). In addition, we proposed a new structural shape to prevent lengthwise cracks and investigate effective reducing cross section method by analyzing it. For the analysis, MIDAS/iGen, structural analysis software, was used to perform static incremental loading applying horizontal force while exerting a constant vertical force.

3.1. Analysis model and method

Fig. 9 shows the outline of the analysis model, and Fig. 10 shows the list of analysis model including the new structural shape. We performed material nonlinear analysis by modeling concrete with solid elements and reinforcing rods with truss elements. The adhesion of concrete and reinforcing rods was assumed to be adequate, and reinforcing rods was not taken out. The breakdown criterion of Mohr-Coulomb was used for the yield survey of concrete, and the yield condition of Von Mises was used for that of reinforcing rods, and the rigidity of the reinforcing rods after the yield was 1/100 of the elastic rigidity.

As an analysis model, we prepared an experimental model that reproduced the specimens (No. 1, No. 2) to reproduce experiments of Chapter 4 and a real model to examine new structure shapes. For the real model, we used the composition rule that gained validity in the experimental model. As a new structural shape, we proposed the followings, No. 3 to reduce the bending stress of the lengthwise cracks generation position by raising the cross section switching part, No. 4 to eliminate abrupt cross-sectional change by providing the tapered part at the cross section switching part, and No. 5 to provide the tapered part on the foundation.

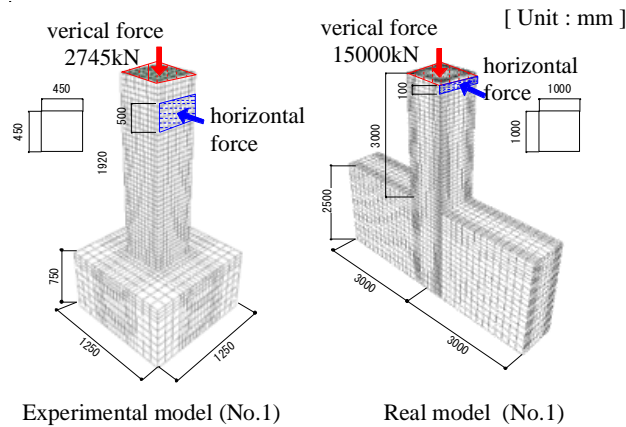


Figure 9. Analysis model

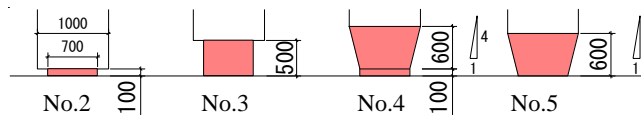


Figure 10. analysis models

3.2. Result and discussion

Fig.11 shows the comparison of shear force – deformation angle relationship between the experimental model and experimental results. In both No. 1 and No. 2, the experiment result and the analysis result are in good agreement, and the validity of the analysis model can be confirmed.

The lengthwise cracks occur at a position where tensile principal stress generating larger than the burst strength (tensile strength) in a direction orthogonal to the principal stress direction. As shown in Fig. 12, the lengthwise cracks of No. 2 occurred earlier in the analysis result. This is considered to have occurred earlier than the actual recording because it was determined visually in the experiment. In addition, it can be said that the reproducibility is high because the analysis result was in good agreement with the lengthwise cracks at the time of experiment such as occurrence place, direction.

Next, we compared and examined by the structure shape. Fig. 13 shows the comparison of shear force – deformation angle relationship by the structure shape. The effect of the reducing rigidity can be confirmed in all the semi-rigid models (No. 2 to 5) against No. 1. For No. 2 and No. 3 with the abrupt cross-sectional change, the occurrence of lengthwise cracks was delayed in No. 4 and 5 with a tapered part. In addition, lengthwise cracks were generated almost in the elastic range.

Therefore, in the next chapter, the difference in the occurrence of lengthwise cracks due to the structural shape will be quantitatively understood from the results of elastic analysis.

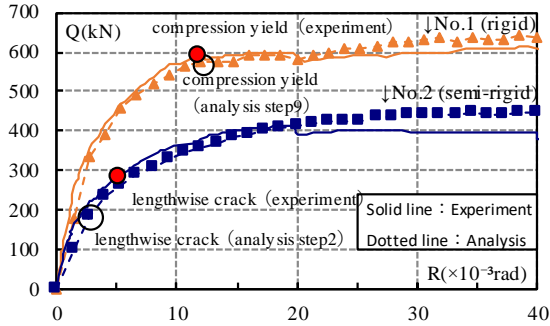


Figure 11. Comparison of shear force – deformation angle relationship

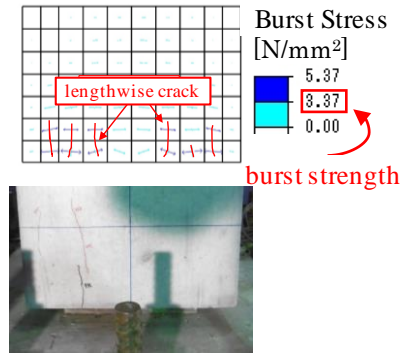


Figure 12. Comparison of length wise crack

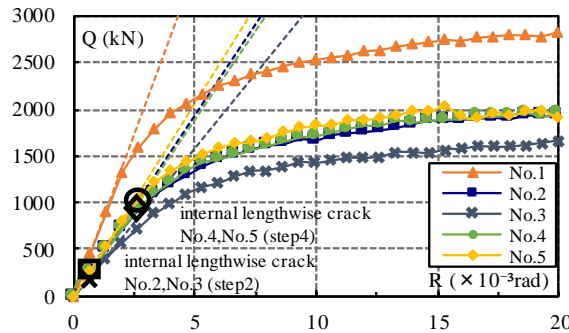


Figure 13. Comparison of shear force – deformation angle relationship by structure shape

3.3. Estimation of maximum bursting stress and comparison by shape

Fig. 14 shows the comparison of the maximum principal stress distribution. The burst stress that causes lengthwise cracks was distributed at the maximum immediately above the end of the reduced part on the compression side, which was common to all of No. 2 to 5. Also, in No. 4 and 5, the maximum burst stress was small and the occurrence of lengthwise cracks considered to be delayed, which was consistent with the result in the previous chapter. For this maximum burst stress (σ_{ymax}), elasticity analysis of 120 patterns was performed based on the analysis parameters shown in Fig. 15 to obtain an estimation equation (1)

$$\sigma_{ymax} = k_1 t_1 \frac{N}{A} + k_2 t_2 \frac{M}{Z} \quad (1)$$

Here, k_1 and k_2 are shape factor determined by the reduction ratio and the aspect ratio of the reduced part, and t_1 and t_2 are taper factor determined by the taper angle when taper is given (without taper, $t_1=t_2=1.0$). Each of them can be obtained by their structure shape using Fig. 16 and 17.

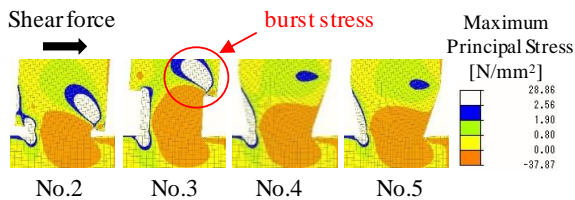


Figure 14. Comparison of maximum principal

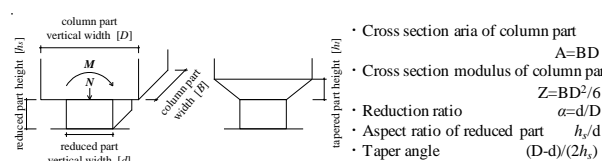


Figure 15. Analysis parameters

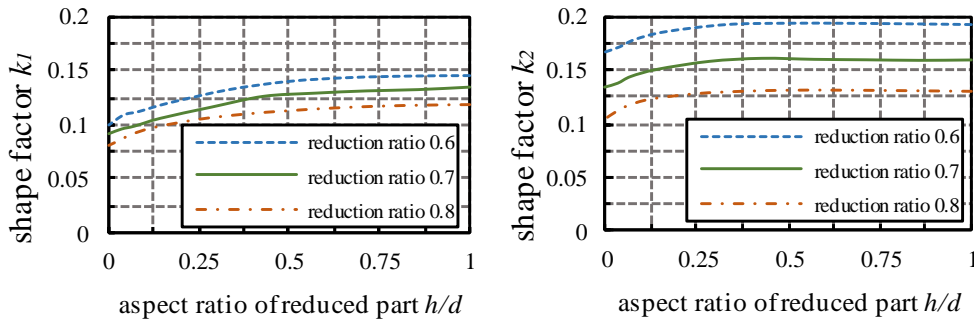


Figure 16. Relation between shape factor k and shape

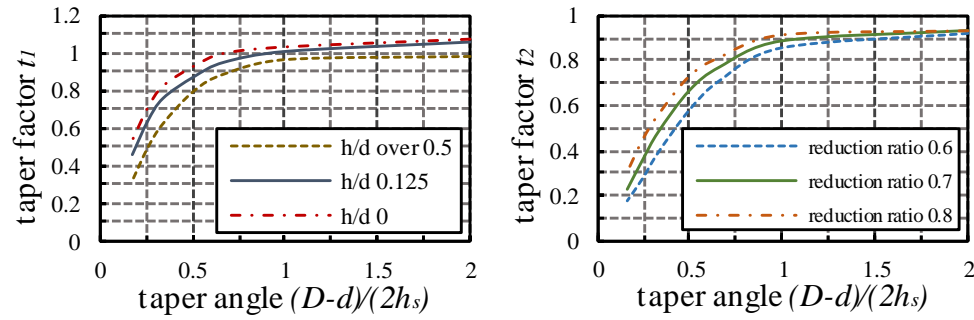


Figure 17. Relation between taper factor t and shape

The lengthwise cracks due to the difference in the structural shape was investigated by the equation (1). The axial force ratio was 0.25 with respect to the column part, and the lengthwise cracks criteria was 1.5 times the bending cracking moment. Now we compared the maximum burst stress for each structural shape determined by axial force and switching part moment at that time.

Fig. 18 shows the results of determination of occurrence of lengthwise cracks. It said that the effect of decreasing the maximum burst stress was small when the switching part was raised. Also, the difference due to the reduction ratio was small. On the other hand, it was found that the reduction effect was large when the tapered part was added and the taper angle was decreased. Especially, when the taper angle was 4/12 or less, the maximum burst stress was smaller than the burst strength, so lengthwise cracks could be suppressed.

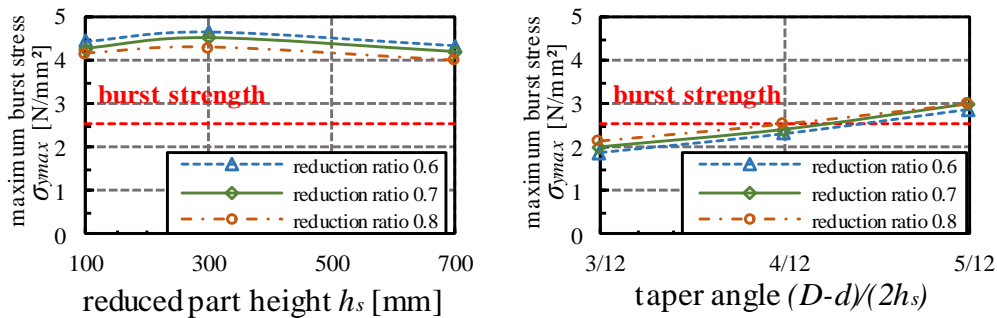


Figure 18. Determination of occurrence of lengthwise cracks

4. Experimental Study on RC Columns with Tapered Part

In the FEM analysis of the previous chapter, it was found that lengthwise cracks can be mitigated by providing a tapered part between the column part and the reduced part. Therefore, we conducted experiment aimed at grasping the control effect of lengthwise cracks and the rigidity reduction effect in the case where the tapered part is provided and the case where the

reduced part is extended in the height direction.

4.1. Specimen and method

Table 5 shows the list of specimens. The specimen consists of a total of three bodies, the two with the tapered part whose taper angle are changed and the one with the extended reduced part. Fig. 19 shows specimen diagram. The upper part of Fig. 19 shows the column part, and the lower part shows the tapered part and the reduced part.

As shown in Table 5 and Fig. 19, the reduction ratio in each specimen is 0.8. The taper angle of two specimens is 4/12 (No. 6) and 6/12 (No. 7). Each height of the reduced part is 45 mm.

Table 6 shows the material test results. The concrete strength is F_{c60} in the column part and F_{c100} in the reduced part and tapered part. The experiment method is the same with chapter 2.

4.2. Result and discussion

Table 7 shows the list of experimental results, Fig. 20 shows the occurrence of initial cracks, Fig. 21 shows the shear force – deformation angle relationship and the cracking situation at 1/50 rad.

In No. 6, firstly, bending cracks (①) occurred in the reduced part, secondly, lengthwise cracks (②) occurred in the corner of compression surface, and finally, lengthwise cracks (③) occurred in the column part and the tapered part at 1/186 rad, which is considerably larger than 1/400 of the previous specimens without taper. The initial rigidity was 10.72×10^4 kN/rad.

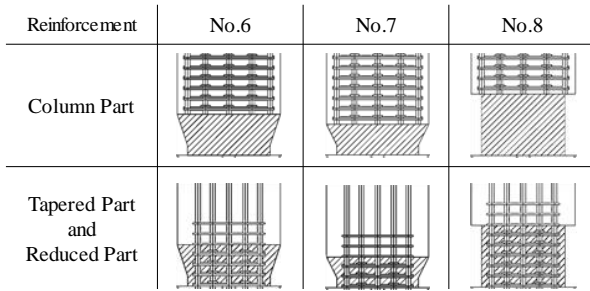
In No. 7 and 8, the order between cracks (②) and (③) was invers against No. 6. The deformation angle when lengthwise cracks occurred in the column part was 1/306 (No. 7) and 1/538 (No. 8). The initial rigidity was 10.90×10^4 kN/rad (No. 7) and 9.58×10^4 kN/rad (No. 8).

Table 5. List of specimens

specimen	column part						
	cross section			concrete strength Fc (N/mm ²)	reinforcement		other
	B (mm)	D (mm)	Lg (mm)		main p _t (%)	shear p _w (%)	
No.6	450	450	1740	60	16-D19 (SD490) p _t =0.79	5-D6@45 (SHD685) p _w =0.78	Same as previous experiment
No.7			1785				
No.8			1650				

specimen	reduced part						
	cross section			concrete strength g Fc (N/mm ²)	reinforcement		constitution of cross section
	Br (mm)	Dr (mm)	Ls (mm)		main p _t (%)	shear p _w (%)	
No.6	360	360	180	100	16-D19 (SD490) p _t =1.24	4-D6@45 (SHD685) p _w =0.78	Reduction ratio 0.8 , Taper angle 4/12
No.7			135				Reduction ratio 0.8 , Taper angle 6/12
No.8			270				Reduction ratio 0.8

Lg : The length from the part change point to the top of the specimen , Ls : The length from the column base to the part change point
 ※Set a height of 45 mm in the column base of No. 6 and No.7



※Shaded part is Fc100

Figure 19. Specimens diagram

Table 6. Material test result

part	type material	yield point (N/mm ²)	yield strain (× 10 ⁻⁶)	elastic coefficient (× 10 ⁵ N/mm ²)
main reinforcement	D19 (SD490)	533	2916	1.94
shear reinforcement	D6 (SHD685)	724	3888	1.86

part	compressive stress (N/mm ²)	bursting stress (N/mm ²)	elastic coefficient (× 10 ⁴ N/mm ²)
column	69.0	4.05	3.31
taperd and reduced	92.8	4.81	3.79

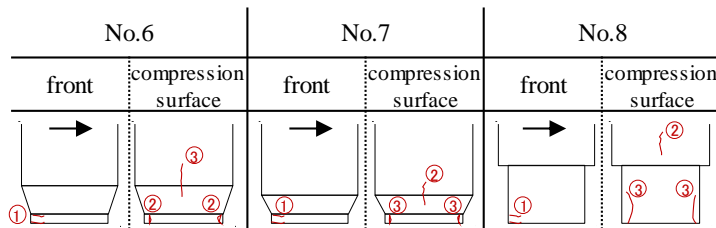


Figure 20. Initial crack progress diagram

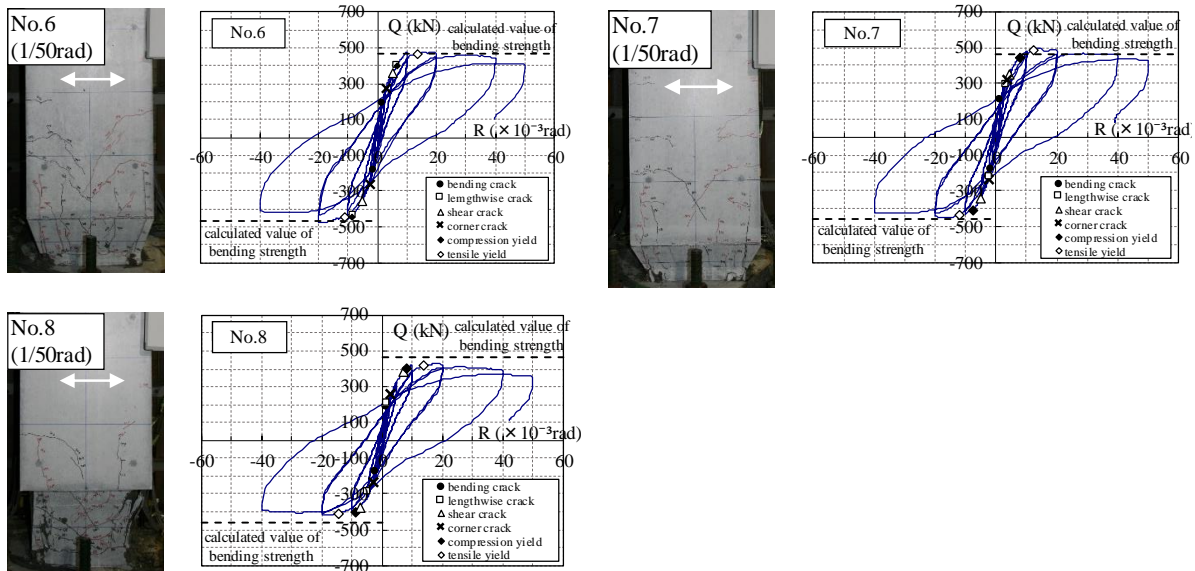


Figure 21. Shear force – Deformation angle relationship

Fig. 22 shows the comparison of envelopes. In the figure, a general column (No. 1) of previous specimen is superimposed as a reference value. From the figure, the rigidity and strength of each specimen are lower than No. 1. By providing the reduced part and the tapered part, the

rigidity of the column base was reduced.

Fig. 23 shows the transition of axial deformation. The axial deformation of each specimen was nearly equivalent. This value is about twice as large as that of No.1 without the reduced part. This axial deformation is an influence due to the reduction of the cross-section area, and the situation where the reduced part is pushed into the column part was not confirmed.

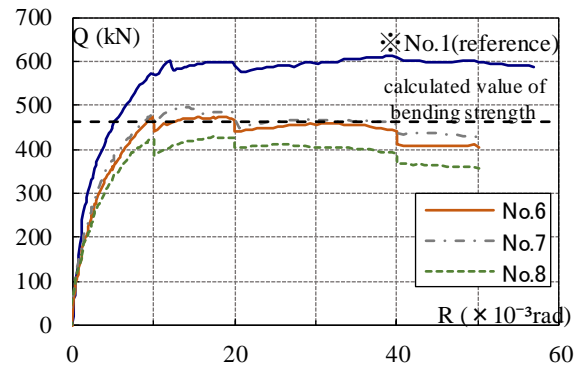


Figure 22. Comparison of envelopes

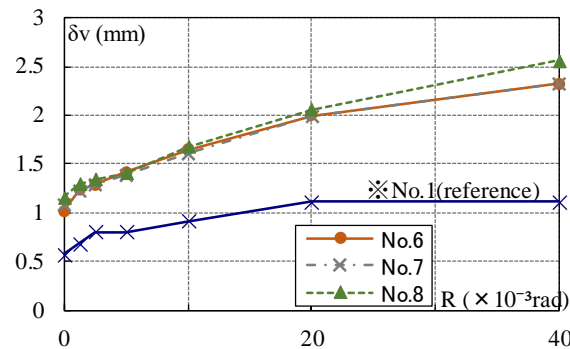


Figure 23. Transition of axial deformation

Conclusions

In this paper, the problems of the general design method are shown, and the semi-rigid base RC column is proposed as the solution. In addition, the following findings were obtained from experiments and analysis on the semi-rigid column base

- 1) By providing a reduced part on the column base, the initial rigidity can be reduced to 60~70% with respect to the general column.
- 2) When a steel is used for the reduced part, local crash occurs and axial deformation progresses.
- 3) When the reduced part is provided, burst stress occurs at the cross section switching part and lengthwise cracks occur. As a method to solve this problem, it is effective to provide a tapered part having a taper angle of 4/12 or more.

From the above findings, it is concluded that by providing the tapered part and the reduced part in the column base, it has stable structural properties and it is possible to reduce the rigidity.

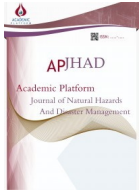
Acknowledgements

I wish to acknowledge Sumitomo Mitsui Construction Co., Ltd. for their assistance in

conducting this research. Also, I wish to thank Takei Sotaro for doing this research together and for teaching us many things.

References

- [1] Yoshimatsu Toshiyuki, Nishimura Noriyoshi, Konomi Mitsuo, Isemoto Noriaki, Yamaura Ichiro, Uozumi Masashi et al. "Development of Semi-rigid Connections for Cast-in-place Pile Head." Summaries of technical papers of annual meeting Architectural Institute of Japan. 2006; Structural 4: 349-366.
- [2] Nagashima Ryutaro, Oda Minoru, Hirata Yuichi, Tano Kenji, Ito Akira and Takaoka Yuji. "An Analytic Study on Semi-rigid Connections for Pile top, Foundation Beam and Column Bottom of First Floor." Summaries of technical papers of annual meeting Architectural Institute of Japan. 2015; Structural 4: 589-590.
- [3] Hirade Tsutomu, Sugimura Yoshihiro, Funayama Hikoshiro, Satio Tadashi and Murakami Masakatsu. "Experimental Study on Pile Head Joint of High Rotational Freedom System." Summaries of technical papers of annual meeting Architectural Institute of Japan. 1999; Structural 4: 527-528



A Mini-Review on Chemical and Biological Human Health Risk Assessment of Water Pollution Afterward of Earthquake

Ahmet Celebi^{1*} , Beytullah Eren¹

¹Department of Environmental Engineering, Sakarya University, 54050, Sakarya, Turkey

Received: / Accepted: 24.12.2019 / 08.06.2020

Abstract

Earthquakes are one of the biggest disasters in the world reality. As a result of earthquake many undesired problem come true. Water is vital for human and health. To protect and predict the water quality is essential all the time included disaster terms. Risk assessment tool is very important for management of disaster likewise many other applications of life. Today risk management and assessment still need more attention. Showing importance of human health risk assessment with considering the earthquakes, risk assessment methodologies, approaches, requirements are main purposes of the present study. As result, very big links were showed between water, health earthquakes along with their potential methodologies.

Key words: earthquake, human health, risk management, water pollution

1. Introduction

The risk assessment is important for clean-up of released pollutants, besides it has a very critical role in assessing the incident's possibly long-term negative health results. Chemicals has existed for a long time and has effects on human health. Although we do have information about most of chemicals, we still have limited knowledge about some chemicals. Therefore, new materials and new information are constantly being developed [1].

To identify true risk, important chemical information on human health is combined with exposure information. Some researchers have calculated for by their intended use a risk assessment of industrial products of many kind chemicals. We focus on lifetime exposures in this study. In the present, even no proper European guidance is applicable for the risk assessment about following chemical incidents or disasters [2].

Human health risk assessment in chemical incidents are different from all exposures up to a lifetime. To foresee to different health situation as take account of potential sensitive populations are important for chemical risk in terms of human health. Therefore the main purpose of this study is adding value of disaster management in terms of risk assessment methods and water quality relations and attract to decision makers about risk management.

* Corresponding Author,
e-mail: ahmetc@sakarya.edu.tr

2. Risk Assessment Approaches and Methodologies

The risk assessment is utilized in to many different states. The risk assessment about the process security is valid to all processes. That processes are risk analyzed, identity of risks, risk prediction and risk assessment [3]. Process safety will be able to referred as "result evaluation" in the future and the risk assessment can be used in a toxicological sense.

If we think a risk assessment about human health, this is calculated by the level of exposure to polluted environments. The negative effects on human health are examined. In this process, the nature, severity and probability of these effects are determined. Risk assessment steps are shown to be a four-step process in figure [4]

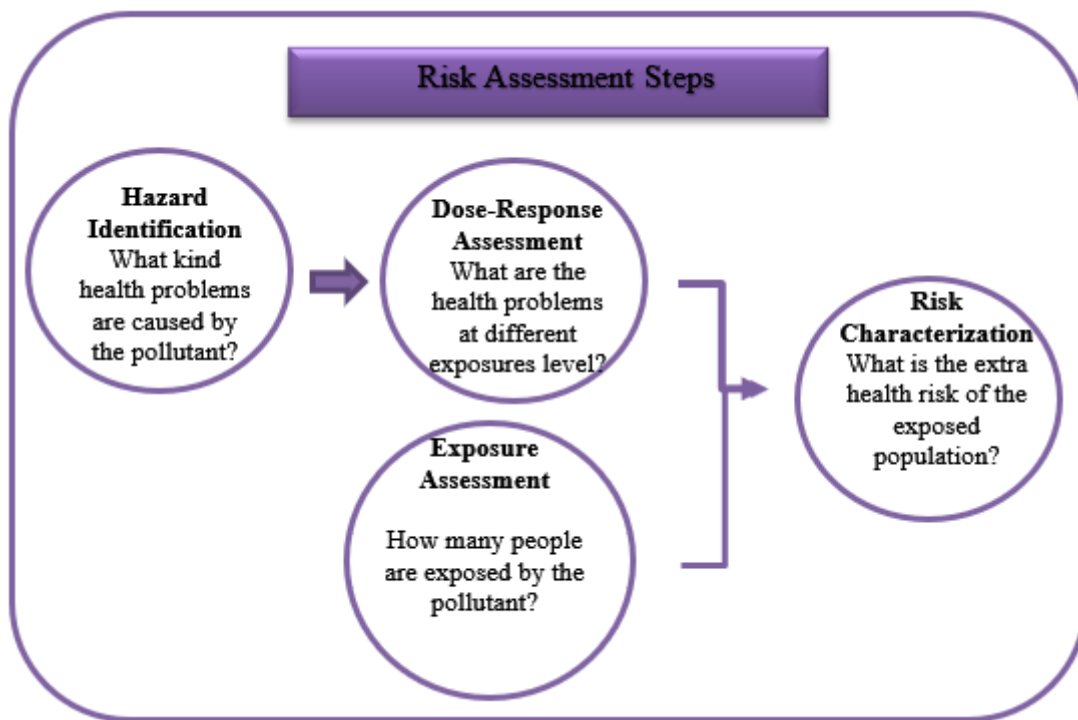


Figure 1. Risk assessment model

In the risk assessment on the avoiding stage, risks analysis and risks reduction are an important risk analyze factors. In particular, we should focus on the risks that could have serious consequences. The risk assessment is a scenario analyze factor of emergency response, planning and result assessment. Detection and warning systems are a sustained activity because of engage to collect of the chemical signals, also provide rapid timely alert. If the concentration of the chemical increases, the signal level may also increase. This event depends on risk assessment. Recovery can last for years with activities of to return to the previous state [1].

The harmful effects of pollutants depend on many factors. These are factors such as the transformation of molecular forms and valences. Chemical pollutants can be toxic at "physiological dose" may be stimulatory in very minute doses, depending upon age, sex, species differences, stress, relationships between chemical pollutants in biological systems [5]. Some chemicals are necessary and useful at low levels. Higher levels are toxic and some have no function. The likelihood of cancer over the course of exposure to potential carcinogens is expressed by the risk estimate for carcinogens. As quantitative level, USEPA has identified a risk level range of one in a million to one in a hundred thousand as an appropriate risk

management goal for the general population, as long as the most sensitive population is protected at 1 in 10,000 [6]. The occurrence of carcinogenic effects in the contaminated regions may not be clearly shown because it requires decades of sustained exposure to develop cancer [7, 8].

The Hazard Quotient (HQ) and Hazard Index (HI) of chemicals are easily can be calculated for both children and adults in terms of dermal, inhale and ingestion factors in the source of water. As formulas;

$$HQ_{\text{ingest}} = ADD / RfD_{\text{Dose}} \text{ (RfD)} \quad (\text{I})$$

$$ADD = C_w \cdot IR \cdot EF \cdot ED / BW \cdot AT \text{ (II)}$$

where units ADD (Average daily dose) is mg/kg-day

C_w (Chemical concentration in water) (mg/L)

IR(Ingestion rate) (L/day)

EF(Exposure frequency) (days/year)

ED(Exposure duration) (years)

BW(Body weight) (kg)

AT(Averaging time) (years)

Ingestion rate can be assumed to be 2 L/day for adults and 0.64 L/day for children; Exposure Frequency can be assumed to be 350 days/year and Exposure Duration 30 years for adults and 6 years for children. The mean Body Weight of adults and children living in the area can be used. Averaging Time is assumed to be equal to Exposure Duration.

For dermal quantitative risk assessment:

$$HQ_{\text{dermal}} = DAD/RfD_{\text{dermal}} \text{ (III)}$$

$$RfD_{\text{dermal}} = RfD \times GAF \text{ [8]} \quad (\text{IV})$$

where GAF = gastrointestinal absorption factor, a risk-based concentration

$$DAD = \text{Dermal absorbed dose (mg/kg-day)} = K_p \cdot C_w \cdot ET \cdot EF \cdot ED \cdot SA / BW \cdot AT \text{ (V)}$$

In addition;

K_p (Dermal permeability coefficient) (cm/h)

SA(Skin surface area) (cm²)

Carcinogenic risk is main problem and risk factor which can be determined by two factors. These are reference dose (RfD) and cancer slope factor (CSF). Most factors that cause cancer do not have these values yet. CSF is a measure of chemical potency and specific to each pollutants differently. A dose-response parameter, called CSF, is used for chemicals exhibiting toxic behavior. As rule, carcinogenic risk increases along with carcinogen pollutants. CSF reflects the health effects of certain levels of carcinogenic pollutants. RfD is the daily exposure

level without significant health risks. RfD is usually derived from an experimental "no observed adverse effect level" (NOAEL) [5]. Carcinogenic risk can be calculated in all kind water, using the formula;

$$CR = ADD.(CSF) (VI)$$

Disaster and especially earthquake can contribute huge amount of chemicals to the water sources. Many chemical has higher level of carcinogen and these Cw value can be very high in the following of earthquake.

3. Links between Earthquakes and Water Quality Systems

The environment and drinking water is polluted with various chemicals from the factories. For instance when the wastes of demolition having 12.5 pH value or more, it is a threat to water life completely. Before and after the earthquake, some measures must be taken to prevent all adverse effects. These can be divided into as two "Preparation Activities before the Earthquake" and "Activities to be done after the Earthquake" [2, 9]. Earthquake locations with their depth and strengths are shown in the figure below.

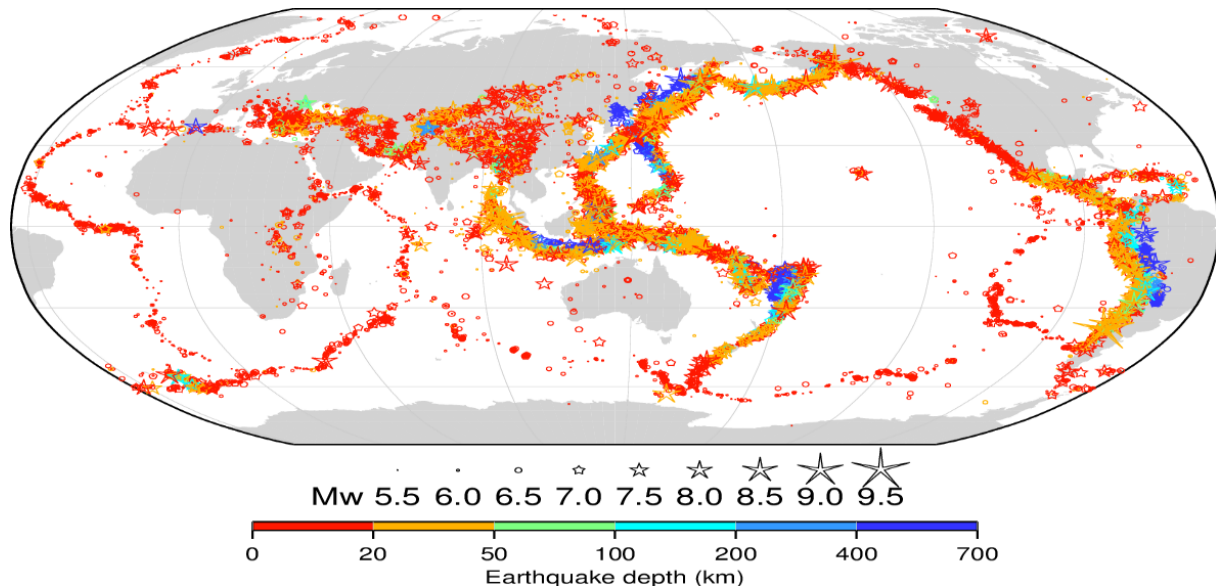


Figure 2. World earthquake locations with symbols (ISC)

Earthquake risk may be analyzed in two main ways; deterministic and probabilistic. In deterministic, usually most adverse earthquake scenario be taken into account. In probabilistic, the all potential earthquake scenario be taken into account with their probability of occurrence. Deterministic approaches are simple may be comprehended as conceptual. There are two main approaches to probabilistic earthquake risk analysis (time-dependent and independent). Periodic tendency of earthquake is calculated in the time-dependent approach. The probability of an earthquake is estimated, depending on the previous event and time. Instrumental and historical earthquake catalogs are combined with geological and geodetic evidence and a seismogenic model covering earthquakes have been produced for thousands of years [10].

Earthquakes are mainly affect to ground and groundwater structure. In a study which conducted the area where 2009 earthquake happened are illustrated in figure.

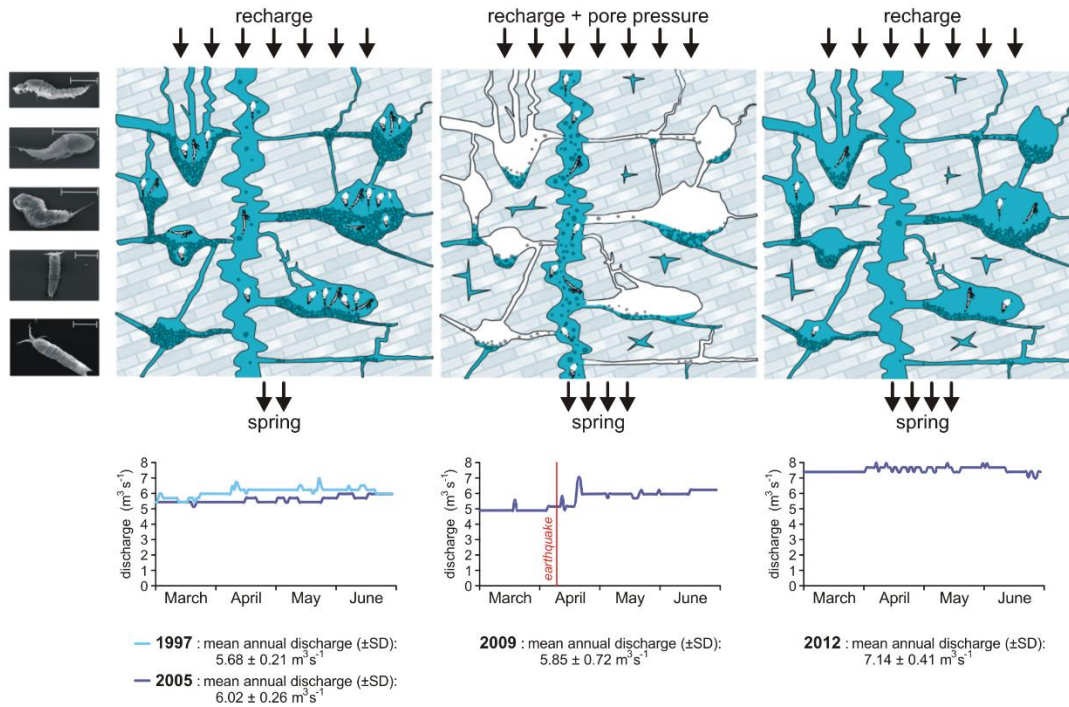


Figure 3. Reaction of groundwater diagram before and after the earthquake biodiversity with changes of aquifer hydrodynamics [11]

In the same study water quality changes were observed significantly different and earthquake almost affected all physical, chemical and biologic parameters in groundwater. pH decreases after seismic water because of as the CO_2 in the main faults increases. At the same time, there was a significant increase in Ca^{2+} (Fig. 4). In September 2009, previously clogged fractures were cleared after ionic enriched water crustal stress and ground shaking. So that electrical conductivity increased. Concentrations of very fine sand and Particulate Organic Matter increased at the main TS outlets due to the massive dehydrating of the conductive systems. Dissolved oxygen (DO) concentration increased significantly after the earthquake, because of groundwater flow paths in the aquifer due to a post-seismic higher hydraulic conductivity.

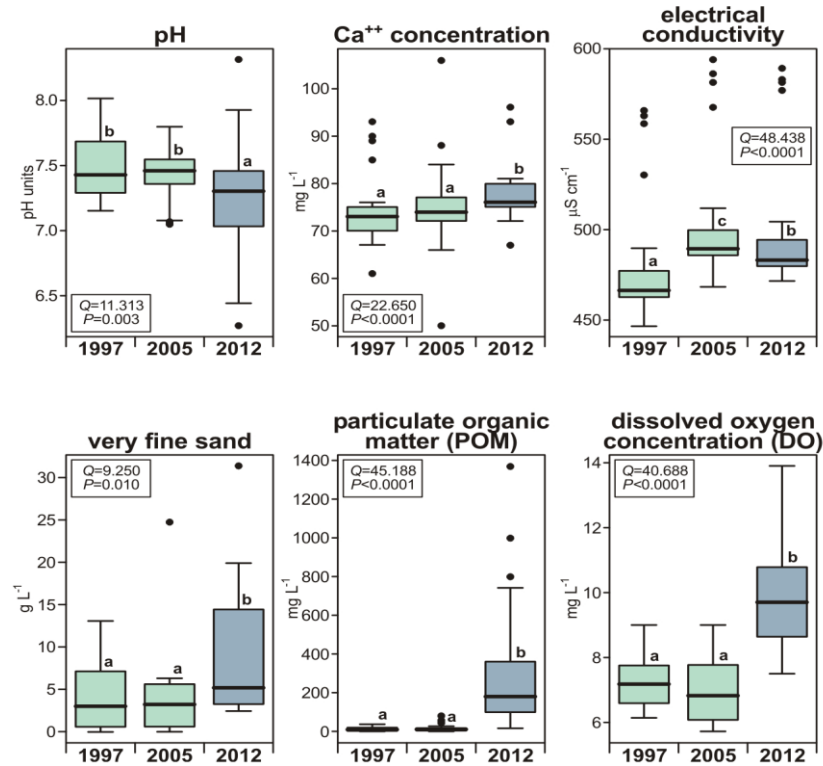


Figure 4. Water quality and sand variables recorded at the Springs before (1997, 2005) and after the 2009 earthquake (2012) [11]

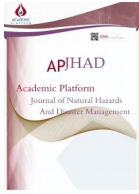
Several industrial facilities for instance oil refineries are in flames after the disaster. Oil and pesticide factories, iron, steel works and automotive, electronics, food processing, paper, plastics and pharmaceutical facilities are also factors. When cleaning work was done in the disaster area, next step problem is what to do with the chemical pollutants that were exposed by these damaged industrial facilities and other sources. These industrial main chemicals are listed in the international standards as carcinogen chemicals. Most are respiratory hazards, neurotoxic and / or carcinogenic chemicals. Many of them can be acutely toxic. Some of them are environmentally continuous effects. This can lead to constant pollution, especially in local soil and water. Chemical health risks that may arise from disasters are linked to environmental and local pollution levels. Risk assessment are very important in this stage to determine quantitatively “normal” or “safe” for residents and workers in the affected area [12].

Conclusions


It is simple true that majority of land in the world has earthquake problem. Earthquakes effect ground and all surface water structure. Water quality should be protected for human health. Decision makers should use risk assessment tools in terms of water contamination for the disaster areas. Many risk assessment approaches were developed and ready to apply for disaster managers. Especially chemical pollutants can be toxic and carcinogen afterward of the earthquake. Industrial lands are needed more attention in this management process. Water is source of life and should not neglect in disasters.

References

- [1] P.M.J. Bos et al. Human risk assessment of single exposure in chemical incidents Present situation and emerging scenarios. National Institute for Public Health and the Environment 2013; RIVM Report 320300001 2010.
- [2] Storchak, D.A., D. Di Giacomo, E.R. Engdahl, J. Harris, I. Bondár, W.H.K. Lee, P. Bormann and A. Villaseñor, 2015. The ISC-GEM Global Instrumental Earthquake Catalogue (1900-2009): Introduction, *Phys. Earth Planet. Int.*, 239, 48-63,
- [3] JRC (2006) Land use planning guidelines in the context of article 12 of the Seveso II directive 96/82/EC as amended by directive 105/2003/EC. Ispra: Joint Research Center
- [4] NRC (1996) National Research Council. Understanding Risk: Informing Decisions in a Democratic Society. Stern PC, Fineberg HV (eds). Washington, D.C.:National Academy Press
- [5] Khan, R.R. Environment and Metal Pollution. Jaipur, IND: Global Media 2010.
- [6] EPA Guidelines for Carcinogen Risk Assessment. Risk Assessment Forum, Washington, DC, 2005; EPA/630/P-03/001F.
- [7] Matzke, A.; Sturdevant D. & Wigal J. Human Health Criteria Issue Paper- toxics Rulemaking, State of Oregon Department of Environmental Quality 2011.
- [8] Çelebi A, Sengörür B, Kløve B. 2014 Human health risk assessment of dissolved metals in groundwater and surface waters in the Melen watershed, Turkey. *J Environ Sci Health A Tox Hazard Subst Environ Eng.* 49(2):153-61.
- [9] Günay Kocasoy 2009 Environmental Pollution Caused by Natural Disasters, www.iswa.org
- [10] UNISDR National Disaster Risk Assessment, Hazard Specific Risk Assessment, 2017.
- [11] Galassi, D.M.P. et al. Earthquakes trigger the loss of groundwater biodiversity. *Sci. Rep.* 2014; 4, 6273; DOI:10.1038/srep06273.
- [12] Chemical Aftermath, Contamination and Cleanup Following the Tohoku Earthquake and Tsunami Environmental Health Perspectives, 2011; volume 117, number 11.



Site Classification of Kocaeli Region Based on HVSR Method

Ali Yesilyurt^{1*} , M.Rizwan Akram¹ and A. Can Zulfikar²

¹PhD Candidate, Earthquake and Structural Eng. Department, Gebze Technical University, Turkey

²Asst. Prof. Dr., Civil Eng. Department, Gebze Technical University, Turkey

Received: / Accepted: 24.12.2019 / 08.06.2020

Abstract

Seismicity and global positioning system (GPS) map of the world displays that Turkey is one of the earthquakes affected region due to active tectonic plates. In current research, one of the highest seismic alert zones of Turkey i.e. Kocaeli district has been selected. The aim of this study is to classify the different sites of Kocaeli region depending on its predominant frequency ranges. More than 300 strong motion data with Moment (M_w) magnitude of 3.0 to 6.5 are available on Disaster and Emergency Management Authority (AFAD) site for Kocaeli. For current region, out of total 32 stations, data recordings from 16 stations have been taken into consideration. Strong ground motion records with $M_w \geq 3$ have been utilized to check the consistency of graphical results by using classical horizontal to vertical spectral ratio (HVSR) technique. Finally, the results of current method are compared with Eurocode8, NEHRP and the 2008 report of the microzonation work done by Kocaeli Metropolitan Municipality and Scientific and Technological Research Council of Turkey (TUBITAK). The procedure obtained from this study is expected to provide foreknowledge to the researchers who will work on this topic.

Key words: HVSR method, Site classifications, Earthquake, Seismic regions

1. Introduction

Civil engineering is the mother of all engineering that has changed the frame of this world into huge sky catching towers and buildings. The most of economical shares in advanced countries like USA, China, Japan, England and France etc. has been contributed to their infrastructure developments. Like other countries, Turkey has also devoted a huge amount in their construction network. As on one side, country's economy is based on their sustainability of their infrastructure, the other side is to protect them from natural disasters like earthquakes. In the Kocaeli devastating earthquake of 1999, approximately 20000 lives were died, and a hundred-million-dollar property was destroyed [1]. So, this serious issue has attracted a great attention of design and earthquake engineers for safety and rehabilitation.

In earthquake design engineering, primarily horizontal component (i.e. east-west or north-south) of input ground motion has been studied for assessment. However, the vertical component (i.e. up-down) contains remarkable information for structures in areas with high seismicity and not shallow bedrock depth. Both the horizontal and vertical component provide same information about the source and path which indicates that there is certain mutual

* Corresponding Author,
e-mail: aliyesilyurt@gtu.edu.tr

correlation between both components [2].

Although earthquake waves move hundreds of kilometers deep, they are influenced by the local site conditions. Many researchers have used HVSr technique to assessment these effects [3-5]. This method includes of using the spectral ratio of horizontal to vertical part of ground motion and approximates the Fourier amplitudes in various frequency range as given in Equation 1.

$$HVSr = \frac{A(f)_{Horizontal}}{A(f)_{Vertical}} \quad (1)$$

Figure-1 shows the common outline of the procedure which was initially employed to the S wave section of the earthquake recordings achieved at three sites in Mexico City [6].

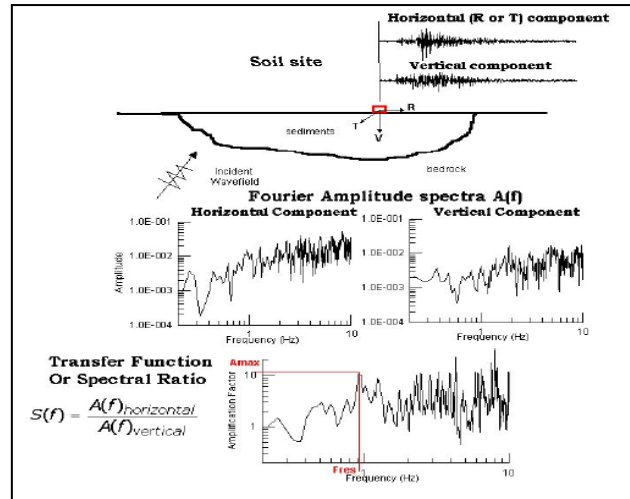


Figure 1. Explanation of the Horizontal to Vertical Spectral Ratio Method [6]

At the same time, the effects of local site conditions on earthquake waves in 1985 Michoacan-Mexico [7], 1989 Loma Prieta [8], 1994 Northridge [9], 1995 Kobe [10], 1999 Kocaeli [11-15], 1999 Chi-Chi [16] and 2000 Western Tottori [17] earthquakes occurring in various parts of the world have been revealed.

Opinions in latest earthquakes indicate that surface geology is one of the essential factors influencing shaking duration [18]. In current study, Kocaeli district has been selected because it is one of the densely populated and industrialized east Marmara regions. 32 stations data are available for Kocaeli state on AFAD website [19]. From total 32 stations, 16 stations are considered due to precise data availability and compatibility with HVSr technique. The purpose is to classify the dominant frequencies of the station regions through the acceleration data and to examine the site response uniformity. The research comprises of more than 300 strong motion records with diverging amplitudes. These data are thus applied to examine whether a traditional site response tool such as HVSr produce stable results all over the region of Kocaeli. Additionally, the dominant frequency values for current results have been compared with NEHRP, Eurocode 8 and with the description of the Microzonation work performed by Kocaeli Metropolitan Municipality and TUBITAK in 2008 [20].

2. Strong Ground Motion Data for Kocaeli Region

Firstly, strong ground motion data records of all 32 stations installed in the region of Kocaeli are carefully analysed and then screening procedure has been adopted. It is observed that data recordings from 16 stations are well presented and is more compatible with the current HVSr technique. Therefore, the strong motion records (approximately more than 300 data) from all

16 stations are saved in the directory for HVSR analysis. Figure-2 shows the locations of selected 16 stations on the seismic fault maps of Kocaeli region.

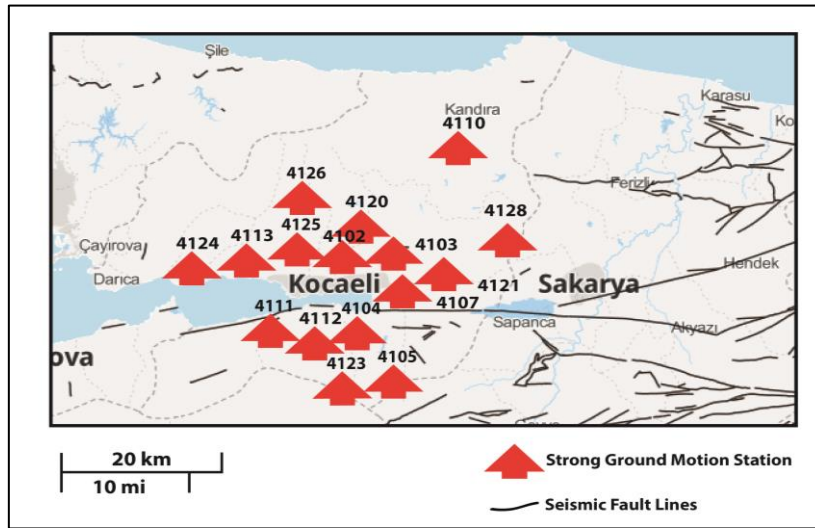


Figure 2. Selected strong ground motion stations of Kocaeli region in current study

Table-1 shows the station codes (SC), their latitude and longitude, installation date and total number of records available in each station used for evaluation of site classifications.

Table 1. Detail of selected stations

No	Station Code	Station Latitude	Station Longitude	Province	Installation Date	Number of Record
1	4102	40.78463	30.02649	Alikahya_Izaydas	2010-09-28	11
2	4103	40.78577	30.02504	Alikahya_Izaydas	2008-03-11	8
3	4104	40.68038	29.96998	Basiskele_Yuvacik	2010-09-28	36
4	4105	40.67441	29.96935	Basiskele_Yuvacik	2008-03-11	44
5	4107	40.76021	29.93244	Karabas	1999-09-12	33
6	4110	41.06910	30.15250	Kandira	2010-05-14	19
7	4111	40.68440	29.58880	Karamursel	2010-05-14	43
8	4112	40.72450	29.84000	Golcuk	2010-05-14	19
9	4113	40.77680	29.73350	Korfez	2010-06-10	24
10	4120	40.76761	30.02737	Alikahya	2012-04-25	15
11	4121	40.72277	29.96985	Kullar	2012-04-25	23
12	4123	40.71515	29.84794	Ihsaniye	2012-04-25	14
13	4124	40.78308	29.60625	Hereke	2012-06-06	8
14	4125	40.76650	29.91721	Kozluk_Meteor	2012-07-06	7
15	4126	40.76252	29.91485	Kozluk_Muze	2013-08-16	15
16	4128	40.72490	30.02435	Kartepe	2014-10-21	10

2.1. Local site classifications

The Metropolitan Municipality of Kocaeli and Marmara Research Center of TUBITAK have produced a seismic microzonation report in 2008 including soil classification map for seismic hazard prediction. Figure-3 shows site classification map for Kocaeli region produced by above two agencies.

In that report, a various, geophysical surveys and geological investigations have been done. These surveys contain macro level site investigations and measurements. Thus, site

classification map has been developed based on the average S wave velocity passing through 30 m depth of soil. For investigation of deep underground structure of the Izmit Basin, S wave profiles and gravity data from 327 points have been collected and from these data have been created 3D bedrock depth of the basin. It has been noticed that bedrock is available at the middle of the basin at a depth of 750-800 m [20]. In the study carried out by Ozalabey et al., thickness was given in the same basin in the range of 1200-1400 meters [21].

HVSr method has been adopted to obtain the site resonance frequency and horizontal to vertical amplification parameters. For this, a total of 422 three component micrometer measurements have been made.

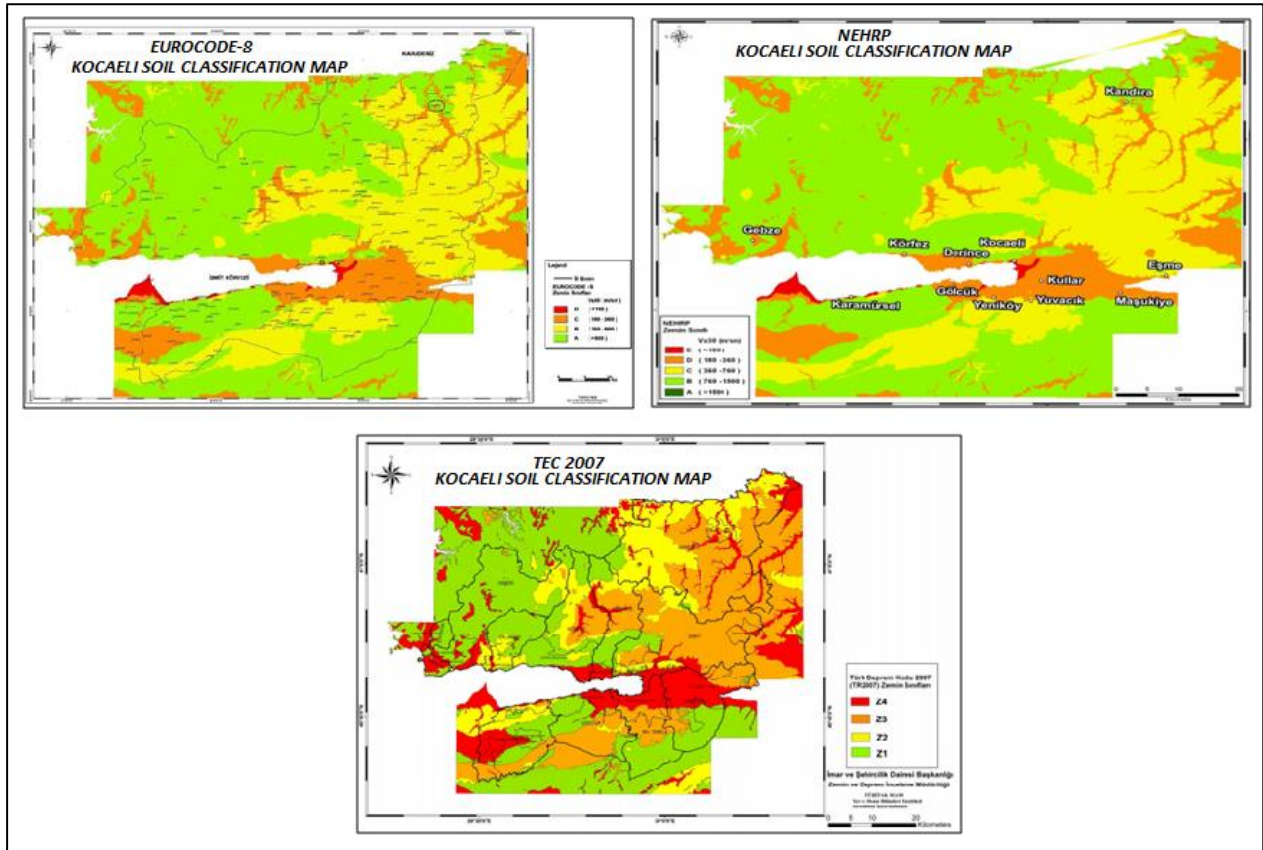


Figure 3. Kocaeli soil classification map according to Eurocode 8, NEHRP and TEC 2007 [22-24]

According to the Eurocode 8 procedure adopted by the Municipality of Kocaeli and TUBITAK Marmara Research Center soil classification has been divided into four categories (A-D site classes). Similarly, According to NEHRP, soil classification has been divided into five categories (A-E site classes). Whereas Turkish Earthquake Design Code 2007 classifies the soil (Z1-Z4 site classes). Figure-3 shows the soil classification map presented for Kocaeli region according to Eurocode 8, NEHRP and TEC 2007. The HVSr technique [25] is commonly used in seismic hazard evaluations since it is comparatively consistent, suitable, and valid for urban areas. To date, the use of the HVSr procedure for site seismic classification is still in progress [26]. For the current research, Figure-3 have been used as reference maps for comparison of the results. Total 16 stations have been considered for the current research to check their soil classifications. All three components (NS, EW, and UD) of records have been considered. Firstly, raw data is analyzed by using MATLAB code [27] and then most suitable records are selected for further processing. In data acquisition and processing, noisy waves with frequencies smaller than 1 Hz and higher than 70 Hz should be separated from the real data [28]. Therefore, a baseline linear correction and a band pass butter worth filtering, with a range

of 1 Hz and 70 Hz is applied. Fourier spectra graphs for data acquisition and processing is shown in Figure 4.

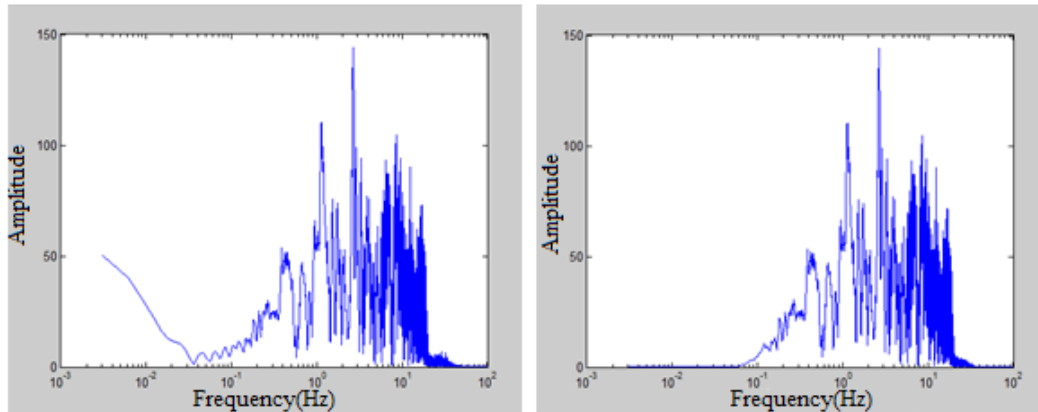


Figure 4. Unfiltered (a) and Filtered (b) Ground Surface Fourier Spectra

3. Results & Discussions

As discussed before, recordings from 16 stations have been considered to classify the site classes (A-D). The output obtained from HVSR ratios are shown in the Figure 5-8. The analysis shows that HVSR are consistent with each other. The obtained ratios are grouped in the following frequency ranges: $f_0 < 1.0$ Hz, $1.0 < f_0 < 2.0$ Hz, $2.0 < f_0 < 3.0$ Hz and $3.0 < f_0 < 5.0$ Hz [29]. In Figures 5-8, SC denotes station codes of selected stations. Different color of graphical curves in Figures 5-8 represents each strong ground motion data that is utilized in HVSR method.

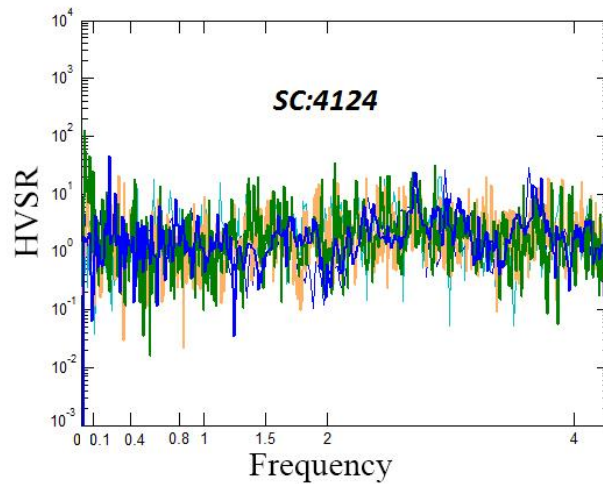


Figure 5. Distribution of the fundamental site frequencies for A site

According to Figure 5. the frequency ranges obtained from station SC4124 (Hereke region), HVSR technique outputs $f_0 < 1.0$ Hz. It is classified as fundamental frequency A class site.

Site Classification of Kocaeli Region Based on HVSr Method

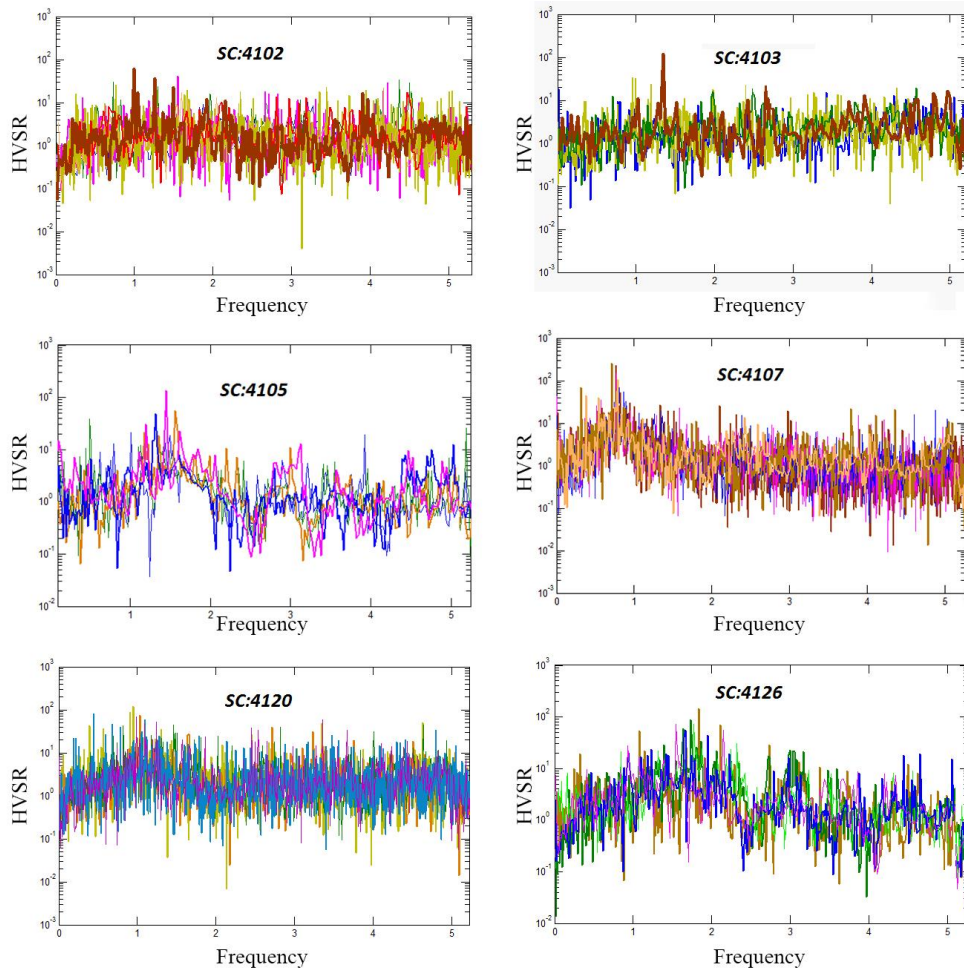


Figure 6. Distribution of the fundamental site frequencies for B site

It is observed in Figure 6 that for SC4102, SC4103, SC4105, SC4107, SC4120 and SC4126, the fundamental frequency ranges $1.0 < f_0 < 2.0$, Hence selected station sites are classified as B site.

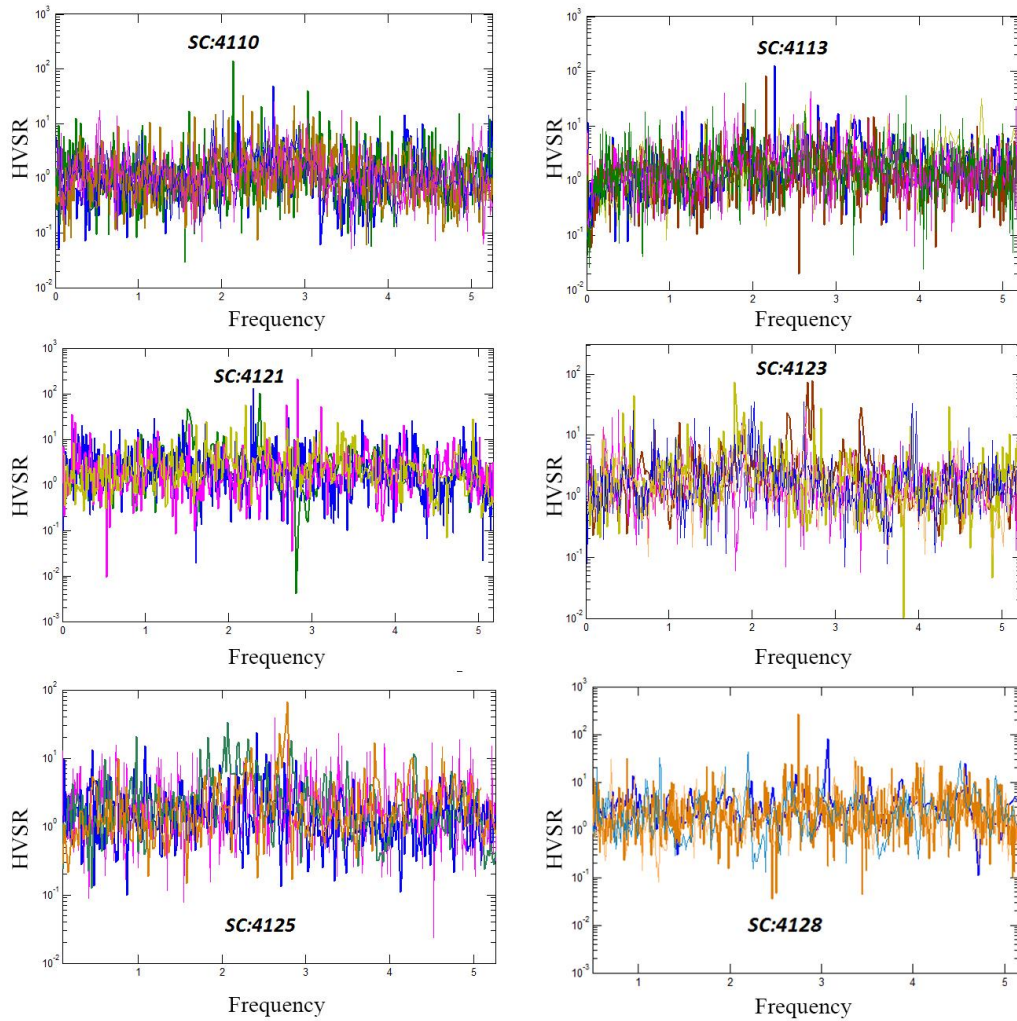


Figure 7. Distribution of the fundamental site frequencies for C site

It has been seen in Figure 7 that SC4110, SC 4113, SC4121, SC4123, SC4125 and SC4128 are within the range of $2.0 < f_0 < 3.0$, thus a site class C is assigned.

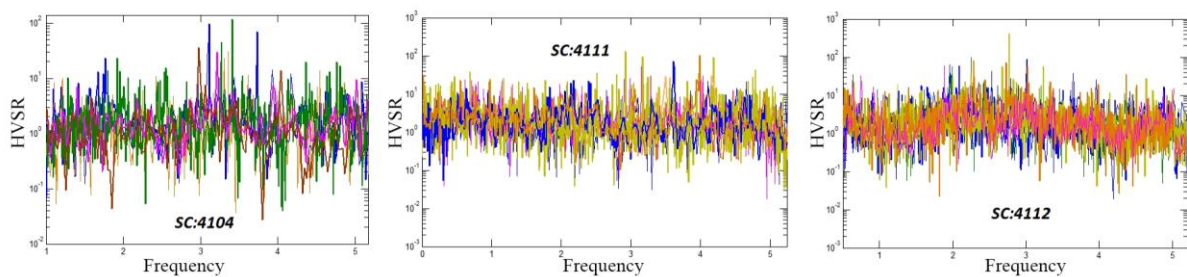


Figure 8. Distribution of the fundamental site frequencies for D site

Figure 8. presents the highest frequency ranges $3.0 < f_0 < 5.0$ Hz, thus according to classification rule, it is classified in site D.

To conclude, the strong ground motion recording station positioned at the site of Hereke possess fundamental frequency ranges less than 1 Hz. Similarly, stations of Alikahya, Basiskele, Karabas are found at fundamental sites frequency ranges of 1.0-2.0 Hz. Stations at Kozluk shows variability that defines the non-uniformity of site classed between B and C. Further, recording sites of Kandira, Korfez, Kullar, Ihsaniye, and Kartepe are found in 2.0-3.0 Hz. Like Kozluk, Basiskele also show non uniformity of soil sites and its stations vary from B and D

classes. However, Karamursel and Golcuk stations have ranges of 3.0-5.0 Hz, thus classified in D class.

3.1. Comparison of site fundamental frequencies with the site classes

The distribution of the fundamental site frequencies for the selected Kocaeli stations have been compared with the local site classes in different codes. Site classification maps given in Figure 3 have been used for comparison. Table-2 yields the comparison results and it can be seen that HVSR provides similar results like other techniques used before for site classification. Thus, HVSR method can also be recommended for the site classification because it is simple and quick method to evaluate fundamental frequency of a site.

In the Table-2, the site classification has been done for the current study in terms of A (frequency ranges: $f_0 < 1.0$ Hz), B (frequency ranges: $1.0 < f_0 < 2.0$ Hz), C (frequency ranges: $2.0 < f_0 < 3.0$ Hz) and D (frequency ranges: $3.0 < f_0 < 5.0$ Hz) respectively.

Table 2. Comparison of the results obtained from this study with previous studies

Station Code					This Study		
	$V_{S(30)}$	NEHRP	Euro Code 8	TUBITAK 2008	Dominant Frequency	Frequency Range	Site Classification
4102	1000	A	A	Z1	1.0	$1.0 < f_0 < 2.0$	B
4103	1013	A	A	Z1	1.0-2.0	$1.0 < f_0 < 2.0$	B
4104	770	C	B	Z3	3.0-4.0	$3.0 < f_0 < 5.0$	D
4105	-	C	B	Z3	1.0-2.0	$1.0 < f_0 < 2.0$	B
4107	305	D	C	Z3	1.0	$1.0 < f_0 < 2.0$	B
4110	380	D	C	Z3	2.0-3.0	$2.0 < f_0 < 3.0$	C
4111	300	E	D	Z4	3.0-4.0	$3.0 < f_0 < 5.0$	D
4112	352	D	C	Z3	2.0-3.0	$3.0 < f_0 < 5.0$	D
4113	300	D	C	Z1	2.0-3.0	$2.0 < f_0 < 3.0$	C
4120	-	A	A	Z1	1.0	$1.0 < f_0 < 2.0$	B
4121	-	D	C	Z4	2.0-4.0	$2.0 < f_0 < 3.0$	C
4123	-	D	C	Z3	2.0-3.0	$2.0 < f_0 < 3.0$	C
4124	-	A	A	Z1	0.2	$f_0 < 1.0$	A
4125	826	D	C	Z4	3.0	$2.0 < f_0 < 3.0$	C
4126	-	D	C	Z4	2.0	$1.0 < f_0 < 2.0$	B
4128	-	D	C	Z4	3.0	$2.0 < f_0 < 3.0$	C

Conclusions

In this study, data from the saved directory of 16 stations are utilized to investigate whether a classical site response tool such as HVSR yield consistent results throughout the region of Kocaeli. Therefore, the predominant frequency values for current results are evaluated and compared with NEHRP, Eurocode8, and the report of the Microzonation work conducted by Kocaeli Metropolitan Municipality and TUBITAK in 2008 to assign site classes.

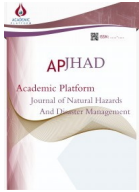
Analysis of earthquake ground motion records show that all the selected stations are located at sites that can be characterized by four fundamental frequency ranges. The obtained ratios can be grouped in the following frequency ranges: $f_0 < 1.0$ Hz, $1.0 < f_0 < 2.0$ Hz, $2.0 < f_0 < 3.0$ Hz and $3.0 < f_0 < 5.0$ Hz. Results shows that HVSR method gives reasonable similar results like other site classification techniques and can be used for the quick site response classification and analysis. Thus, HVSR method can also be recommended for the site classification because it is simple and quick method to evaluate fundamental frequency of a site.

For future works, the results evaluated in this study can be compared with the SSR method. This will allow the future researchers to examine the consistency, precision, and reliability of both techniques.

References


- [1] Muhammed Sahin and Ergin Tari. (2000). The August 17 Kocaeli and the November 12 Duzce earthquakes in Turkey, *Earth, Planets and Space* volume 52, pages 753–757.
- [2] Van Katsuhiko Shirao et al; World Conference on Earthquake Engineering Vancouver, B.C., Canada August 1-6, 2004 Paper No. 623.
- [3] Saman Yaghmaei-Sabegh and Rajesh Rupakhety. (2020). A new method of seismic site classification using HVSR curves: A case study of the 12 November 2017 Mw 7.3 Ezgeleh earthquake in Iran, *Engineering Geology* Volume 270, 5 June.
- [4] Gallipoli, Maria & Mucciarelli, Marco & Gallicchio, Salvatore & Tropeano, Marcello & Lizza, Carmine. (2004). Horizontal to Vertical Spectral Ratio (HVSR) Measurements in the Area Damaged by the 2002 Molise, Italy, Earthquake. *Earthquake Spectra - EARTHQ SPECTRA*. 20. 10.1193/1.1766306.
- [5] Stanko, Davor & Markušić, Snježana & Stelec, Stjepan & Gazdek, Mario. (2017). HVSR analysis of seismic site effects and soil-structure resonance in Varaždin city (North Croatia). *Soil Dynamics and Earthquake Engineering*. 72. 666-677. 10.1016/j.soildyn.2016.10.022.
- [6] Lermo and Chávez-García. (1993). Site effects evaluation using spectral ratios with only one station, *Bull. Seism. Soc. Am.*, 83, 1574 – 1594.
- [7] Seed HB, Sun JH.(1989).Implication of site effects in the Mexico City earthquake of September 19, 1985 for Earthquake-Resistant Design Criteria in the San Francisco Bay Area of California, Report No. UCB/ EERC-89/03, Earthquake Engineering Research Center, University of California, Berkeley
- [8] Seed RB, Dickenson SE, Riemer MF, Bray JD, Sitar N, Mitchell JK, Idriss IM, Kayen RE, Kropp AK, Harder LF, Power MS. (1990).Preliminary report on the principle geotechnical aspects of the October 17, 1989 Loma Prieta earthquake, Report No. UCB/EERC-90/05, Earthquake Engineering Research Center, University of California, Berkeley
- [9] Moehle J. (1994). Preliminary report on the seismological and engineering aspects of January 17, 1994 Northridge Earthquake. University of Calif, at Berkeley, Earthquake Engineering Research Center, Report No. UCB/EERC-94/01
- [10] Takemiya H, Adam M. (1997). Seismic wave amplification due to topography and geology in Kobe during Hyogo-Ken Nanbu Earthquake. *J Struct Mech Earthq Eng* 14(2):129–138
- [11] Erdik M, Doyuran V, Gulkan P, Akkas N. (1985). A probabilistic assessment of the seismic hazard in Turkey. *Tectonophysics* 117:295–344
- [12] Tezcan SS, Kaya E, Ball, Ozdemir Z. (2002). Seismic amplification at Avcılar, Istanbul. *EngStruct* 22:661–667
- [13] Ergin M, Ozalaybey S, Aktar M, Yakin MN.(2004).Site amplification at Avcilar, Istanbul. *Tectonophysics* 391:335–346
- [14] Ozel O, Sasatani T. (2004). A site effect study of the Adapazari basin, Turkey, from strong and weak-motion data. *J Seismol* 8(4):559–572
- [15] Cabalar AF, Cevik A. (2009).Genetic programming-based attenuation relationship: an application of recent earthquakes in Turkey. *Comput Geosci* 9:1884–1896
- [16] Pavlenko OV. (2008).Characteristics of soil response in near-fault zones during the 1999

- Chi–Chi, Taiwan Earthquake. *Pure Appl Geophys* 165(9–10):1789–1812
- [17] M. Rizwan Akram et al. 4th International Conference on Earthquake Engineering and Seismology, 11-13 October 2017, Anadolu University Eskisehir, Turkey
- [18] Randall W. Jibson and David K. Keefer. (1989). Statistical analysis of factors affecting landslide distribution in the new Madrid seismic zone, Tennessee and Kentucky, *Engineering Geology*, Volume 27, Issues 1–4, December, Pages 509-542
- [19] Disaster and Emergency Management Authority (AFAD). (2009). Retrieved from <https://www.afad.gov.tr/>
- [20] The Metropolitan Municipality of Kocaeli and Marmara Research Center of TÜBİTAK report towards Site Classification and Seismic Hazard Assessment of Kocaeli Province of Turkey (October, 2008) Retrieved from <https://www.kocaeli.bel.tr/>
- [21] Özalaybey, S., Zor, E., Ergintav, S., & Tapırdamaz, M.C. (2011). Investigation of 3-D basin structures in the İzmit Bay area (Turkey) by single-station microtremor and gravimetric methods. *Geophysical Journal*, Volume 186, Issue 2, pp. 883-894.
- [22] CODE, Price. Eurocode 8: Design of structures for earthquake resistance-Part 1: General rules, seismic actions and rules for buildings. Brussels: European Committee for Standardization, 2005.
- [23] National Earthquake Hazards Reduction Program (US), Building Seismic Safety Council (US), & United States. Federal Emergency Management Agency. (2001). NEHRP recommended provisions for seismic regulations for new buildings and other structures. Building Seismic Safety Council.
- [24] TEC2007, Turkish Earthquake Code. Specifications for Structures to be Built in Earthquake Areas, and appendix. The Ministry of Public Works and Settlement, 2007.
- [25] Nakamura, Y. (1989). A method for dynamic characteristics estimation of subsurface using microtremor on the ground surface. *Quarterly Report Railway Technical Research Institute*, 30(1): pp. 25 - 30.
- [26] McPherson, A. and Hall, L. (2007). Development of the Australian National Regolith Site Classification Map. *Geoscience Australia Record* 2007/07, 37 pp.
- [27] Guide, Matlab User's. The mathworks. Inc., Natick, MA, 1998, 5: 333.
- [28] William H.K. Lee, Paul Jennings, Carl Kisslinger, Hiroo Kanamori. (2002). *International Handbook of Earthquake & Engineering Seismology*, Part A
- [29] A.C Zulfikar, H Alcik and E Cakti. Analysis of Earthquake Records of Istanbul Earthquake Rapid Response System Stations Related to the Determination of Site Fundamental Frequency. 15 WCEE Lisbon 2012.



Design for wind comfort. The CFD assessment over a future outdoor public space

Elton Hala^{1*}, Neritan Shkodrani²

¹ Faculty of Architecture and Urban Design, Polytechnic University of Tirana, Albania 

² Faculty of Civil Engineering, Polytechnic University of Tirana, Albania 

Received: / Accepted: 26.02.2020 / 08.06.2020

Abstract

People's comfort depends also on the wind condition, which is strongly guided by urban spatial design. This paper focuses on climatic conditions and pedestrian behavior in an urban area. These studies emphasize the connection of people's attitudes with physical and climatic ambiance. The challenge of urban designers is to consider the surrounding structures and the topography to design a comfortable outdoor public space. Two criteria are used to assess the wind in a public space domain. The CFD was used as an instrument to analyze pedestrian wind comfort in the outlined environment. This study has come to important findings related to the air movement in and around the studied domain: High-velocity wind can be a nuisance for most creative activities in the outdoor public space. This paper provided a velocity map for future recreational activities inside the current building pattern. The effects of these architectural patterns were discussed.

Keywords: Outdoor public space, building configuration, wind velocity, CFD, comfort

1. Introduction

Nowadays, the concern in urban safety is raised globally, since the population living inside the urban area is increasing dramatically. More than half of the world population is living in cities or towns with a growing tendency in the upcoming years [1]. In the past 50 years it is observed an increase in cities and town population. By 2050 around 7 billion people or over 2/3 of the world population will be living in urban areas, consequently to the rapid economic growth [2]. Much research is focused on urban environment climate, finding solutions to improve the conditions to a better living habitat. Wind condition is also related to the performance of buildings in an urban area [3]. People's comfort also depends on the wind condition, which is strongly guided by man-made barriers and the urban spatial morphology [4]. City authorities are often obliged to find immediate and long-term solutions to improve microclimate quality in the physical layout of existing high-density cities. Particularly in new urban areas, they often order aerodynamic studies focused on wind comfort to the pedestrian level. Recently, many authorities have given permission to new development areas after wind comfort studies, focusing on pedestrian levels. Therefore, wind safety has always been an issue to consider for people's comfort, typically those living in cities influenced by high-speed wind.

* Corresponding Author,
Phone: +(00) 355 6730 62523 e-mail: tonihala@gmail.com

Every season, people living inside cities enjoy outdoor public areas hence, urban designers are interested in confronting their concepts also with microclimate issues. An interesting domain remains the implementation of comfortable spaces for people living in urban areas. Regularly, outdoor public spaces are conceived as places to walk, relax, interact, and perform between people. Cities reflect the societies that have shaped them, and they participate in shaping human behavior [5]. Often, is distinguished a symbiotic relationship of outdoor public spaces and high-rise buildings, particularly in new urban developments. These buildings in many ways influence the public spaces close to their basement. High-rise buildings often show fascinating elegant shapes, but they are liable for significant changes in the urban area's environmental conditions. The challenge of urban designers is to consider the surrounding structures and the topography in order to design a comfortable outdoor public space. It is also known that wind speed increases in open spaces. This study analyzes people's comfort and public space in order to suggest an outdoor environment with a framework to counter the desired wind conditions.

Much research is done over the years, focused on the urban space's configuration concerning people's comfort. The future of urban public space configuration is directly affected, particularly by wind speed and other environmental elements [6]. The unpleasant environmental conditions generated in an area in San Francisco, principally wind and sunlight, derived by the presence of multistory buildings [7, 8]. These studies emphasized the importance of the design under regional climatic elements. Also, environmental elements and architectural design altogether, affect the user's perception, related to distinctive places [9]. Other studies used real measurements to quantify the relationship between wind conditions and pedestrian behavior [10]. Other studies were focused in personal behavior toward rapid change in wind speed [11]. Other researchers emphasize that people comfort is related not only to environmental factors, but also to other external elements such as clothing, age, and gender, [12]. People's comfort and healthy life in public space areas is yet a major concern to many researchers [13-16]. All these researchers are focused on climatic conditions and patterns of behavior in an urban area. These studies emphasize the direct connection of people's behavior not only with physical and climatic ambiance but also to other social aspects. Hence, urban design impacts people's quality of life.

The wind is an invisible fluid hence, it is difficult predict. Therefore, the wind is widely being factorized in the urban environment by using computational tools. Several techniques have been used to assess wind flow, but it seems that only one, above all methods, prevailed over the last 50 years. If it is considered the affordability, accuracy and information availability, computational fluid dynamics (CFD) is one of the most effective methods to evaluate the building environment design [17]. On-site analysis and wind tunnel methods present incomplete information in comparison to CFD. Wind tunnel evaluates only few areas in a physical model, and it doesn't cover the whole flow field at once [18]. Because of these advantages, CFD simulations are commonly applied to analyze the wind flow in environmental sensitive domains [19]. The CFD has been used for partial information and rarely as part of a complete study on pedestrian safe and comfort [20, 21].

Several researchers highlight the Raynold-Averaged Navier-Stokes (RANS) as a CFD mathematical model [22]. RANS model is also used to determine the wind flow pattern to evaluate the influence of the domain's geometry [23]. RANS CFD simulations are an effective method to assess pedestrian wind comfort and safety in urban areas [24].

1.1 Case study.

Rapid urbanization also affected Tirana due to fast economic changes. The urban development is often chaotic, and the green space is decreasing constantly, giving space to buildings and concrete pavements. The local authorities intended to expand the future development of the city by extending the main boulevard in the northern part of it, renovating the banks of the river Tirana and the rest of the area. That part of the city presents a lot of environmental challenges such as air and water pollution, urban sprawl, waste disposal, etc. The area close to the river provides an open corridor for the wind to penetrate at high speed. In most cases, areas affected by strong wind are located along the seaside or close to riverbanks [32]. There were several proposals, but the winning one suggested a pattern of public spaces extended along the newly designed boulevard. One of the most discussed domains was the new central park positioning. This public area will be surrounded in all its contour by tall buildings adjacent to the riverbanks, (Figure 1). During the project presentation, the designers provided environmental studies by showing an ambitious urban design, but we couldn't find any study focused on wind flow. Urban areas, above all, should provide safety and comfort to their occupants. We focus this paper on pedestrian comfort, involved in various activities in this newly suggested development. The purpose is to merge the existing terrain and the future design geometry into wind comfort assessed by CFD.

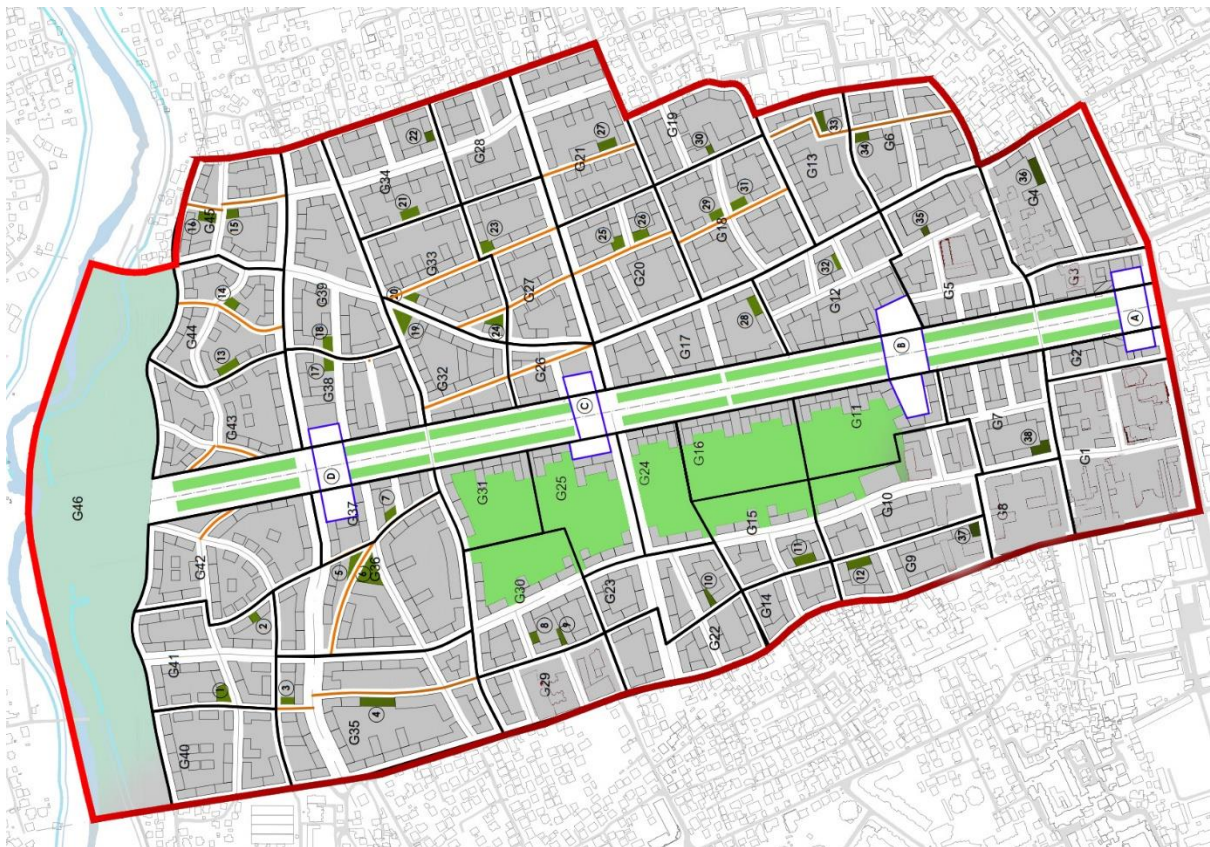


Figure 1. The winning masterplan (future park).

2. Method

2.1 Three-dimensional model and RANS Computational parameters

After being supplied with the future urban development drawing, we could create a three-dimensional model in real scale 1:1 using computer-aided design (CAD) software package. Since urban development covers a large area, we have provided none building details. Our model was not limited only to the building's main geometry but also to the surrounding buildings nearby the studied area. The CAD file is considered being topologically incorrect due to the participles (triangles) that constitute a mesh surface. These participles easily intersect with other meshes, resulting in missing geometries. That is why the 3-D model is exported as an STL file, to be used by ANSYS CFX 12.0 software package. CFD software adopts a special "shrink-wrapping" mesh topologically correct and can be therefore used as a model boundary for the simulation.

Two transport equations were used to explain the RANS turbulence parameters: the first equation is focused on kinetic energy k and it is called the transport equation. The second equation controls the transport of the dissipation rate ϵ of K . The turbulence parameters for the model were: Model of turbulence= k -epsilon. Turbulent kinetic energy= 0.015 , Turbulent dissipation rate $\epsilon = 1.7029E-06$ and Specific Dissipation rate $\omega = 0.00126143$. The wind tunnel parameters were: Kinematic Viscosity: $1.5e-005m^2/s$. Density $1.25kg/m^3$. Convergence criterion (P-Residual) = 0.001 .

2.2 Simulation; wind speed

Studies of wind comfort are a collection of three types of data: statistical meteorological data, aerodynamic information's and wind safety and wind comfort criteria [18]. The wind climate is recorded in the standards by local institutions and then broadcast to different media. The wind meteorological data was available at the Weather Spark website. This website represents the mean wind data determined over time for Tirana city. Over the course of the year, the windy days are more frequent along late Autumn, Winter, and Spring. The calmer time lasts for almost 6 months from April to October. Mean wind speed at the chosen site throughout the year varies from 0 km/h to 22km/h. Occasionally the maximum speed exceeds 35km/h approximately (10m/s).

The wind from the north at (10m/s) was chosen as the worst-case scenario. This direction coincides with the open riverbank's corridors responsible for high-speed wind gusts. Hence, this parameter was applied in the CFD simulation as a north vector. This scenario is more likely to happen from November to February. To have a fundamental understating the model was analyzed also from the other directions (East, West, South), but at a lower wind speed 5m/s. Therefore, the model was tested four times in different directions: North 0° -10m/s; East 90° -5m/s; South 180° -5m/s; West 270° -5m/s. After obtaining all the graphs and data, we can increase the awareness of the risky areas and those where comfort is provided during any season. Since the project is not yet implemented the field survey was unavailable. Albania doesn't adopt it is own standards on wind comfort and wind safety, hence we have decided to control the results accordingly [30], [28].

Various societies use different standards to set the limit values for wind comfort and wind safety. The criteria to be used for assessment of pedestrian wind conditions have been developed through research and practice. Most of these criteria try to set a limit wind speed

over a probability to happen [25]. Despite the fact that many studies are made in wind comfort criteria over the years [26, 27, 28, 29, 30, 31]. Albania doesn't apply its own standards on wind comfort yet.

3. Results

3.1 Wind tunnel parameters

Since the model uses a unique geometry, every simulation had the same fine grid in the wind tunnel made by 784,470 cells and 917,448 nodes. This grid has been proven to be efficient in terms of accuracy and computational time. For computational purposes, was used a thicker grid. The results of this model were not considered. The wind assessment is recoded mostly from a horizontal plan 1.7m high. Undoubtedly, the wind speed changes at different altitudes, but our concern was only for the pedestrian level. After the first results, we were able to place also vertical plans to have a better evaluation of the entire area of the future park. Tunnel parameters were: Dimensions: Dx=6540m; Dy= 2955m; Dz=577m; Original model drag force sum: Fx=1341kN, Fy=115kN, Fz=2937kN. Simplified model drag force sum: Fx=1455kN, Fy=167kN, Fz=2398kN. Flow parameters were in the following terms: Inlet velocity 5m/s to 10m/s; Kinematic viscosity $1.5E-005m^2/s$; Density $1.25kg/m^3$.

3.2 CFD simulations

The first simulation on the above grid was performed for the prevailing north wind direction (0°) at 10m/s. Inlet velocity 10m/s. The wind speed ratio inside the future public park areas varies from 0.1m/s-8m/s. Investigating the velocity field plan, is shown that 64% of the future park area is affected by wind high-velocity 4-6m/s with a peak wind velocity at 8.98m/s. Dangerous high wind velocities appear at these areas; ($a1=8.98m/s$); ($a2=6.32m/s$). (Figure 2a). This simulation was also supplied with a vertical plan registry showing the wind velocity at different highs. The vertical plan shows that the air moves much faster above the ground due to the absence of the obstacles. (Figure 3a).

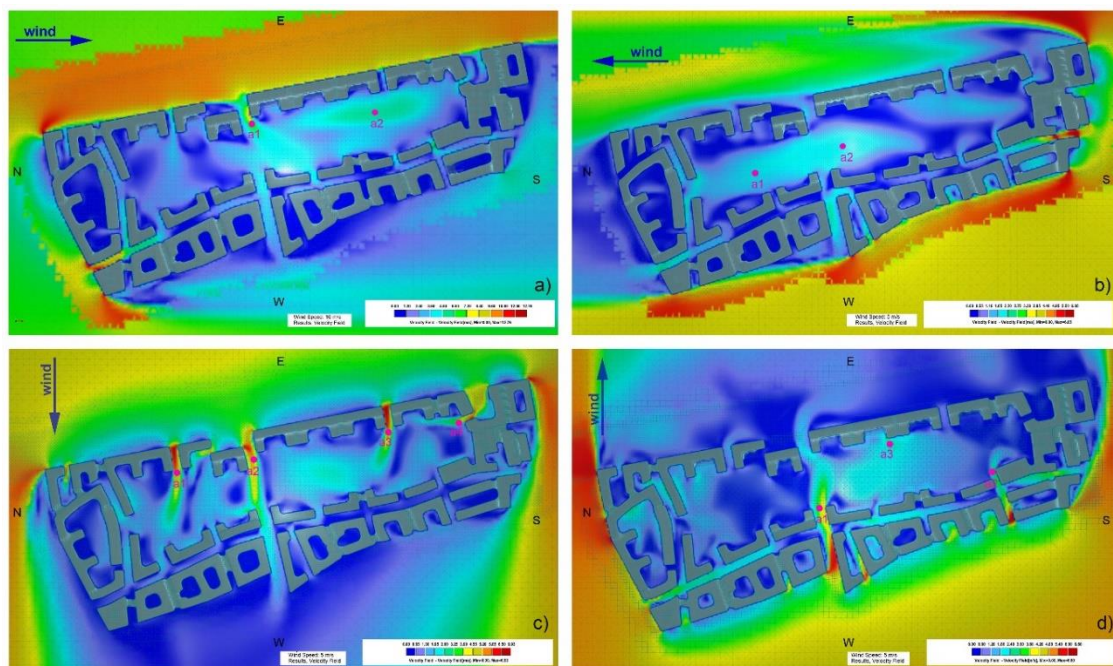


Figure 2. Wind velocity field; (a. north at 10m/s; b. south at 5m/s; c. east at 5m/s; d. west at 5m/s).

In the second simulation, was applied a lower wind speed at 5m/s prevailing from the south direction (180°). The tested speed was diminished since according to the prevailing wind in this direction and the probability it happens. Inlet velocity 5m/s. From this direction, the wind encounters other buildings with almost the same high suggested in the master-plan. Wind speed ratio inside the future public park areas varies from 0.1m/s-1.9 m/s. Investigating the velocity field plan the results show 53% of the future park area is affected by wind high-velocity 1-2m/s with a peak wind velocity at 1.92m/s. The rest of the area is affected by wind speed lower than 1m/s. High wind velocities occur at these areas; (a1=1.92m/s); (a2=1.85m/s). (Figure 2b).

The third simulation adopted the same wind speed as above (5m/s), except the prevailing direction from the east (90°). Wind speed ratio inside the future public park areas varies from 0.1m/s-6m/s. Investigating the velocity field plan the results show 81% of the future park area is affected by wind high-velocity 1-2m/s with a peak wind velocity at 6.11m/s. The outer buildings barrier seems to have several gaps in this direction. The increase of speed at these passageways happens due to a decrease in static pressure or a decrease in potential energy (Bernoulli principle on fluids). Severe wind velocities are recorded at these passages; (a1=6.11m/s); (a2=5.83m/s); (a3=5.94m/s) (a4=4.18m/s). (Figure 2c). A considerable vortex is created in this simulation (Figure 4c).

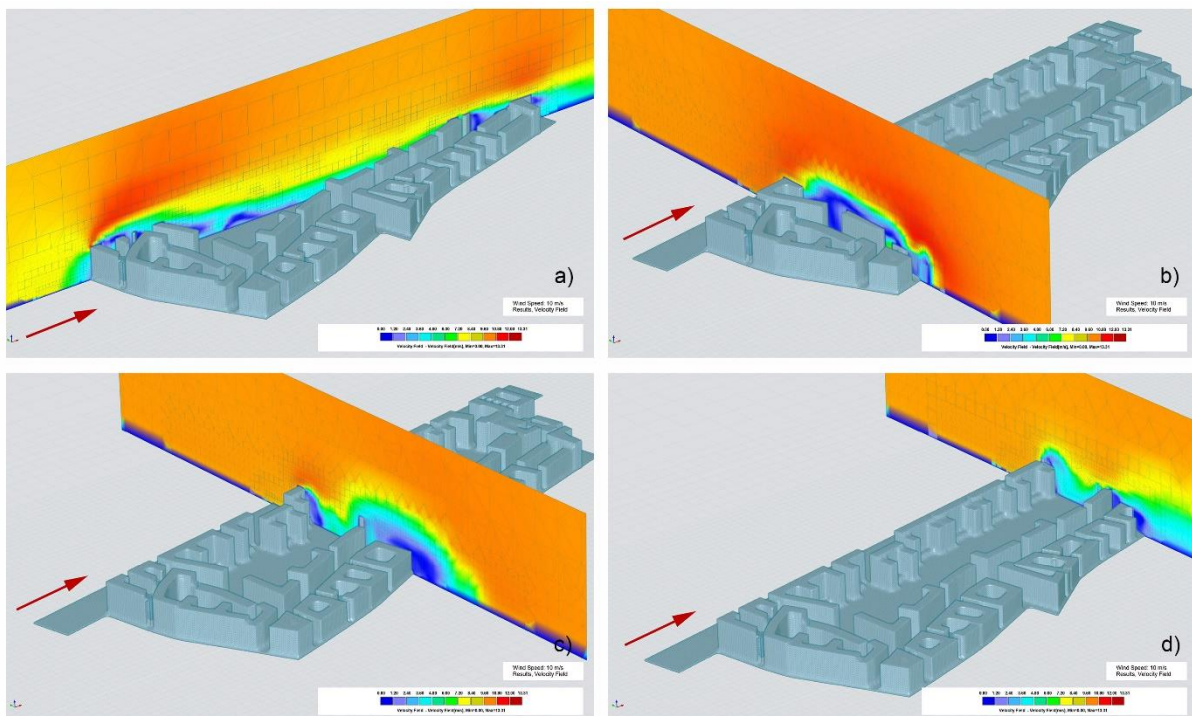


Figure 3. Wind velocity field (north at 10m/s).

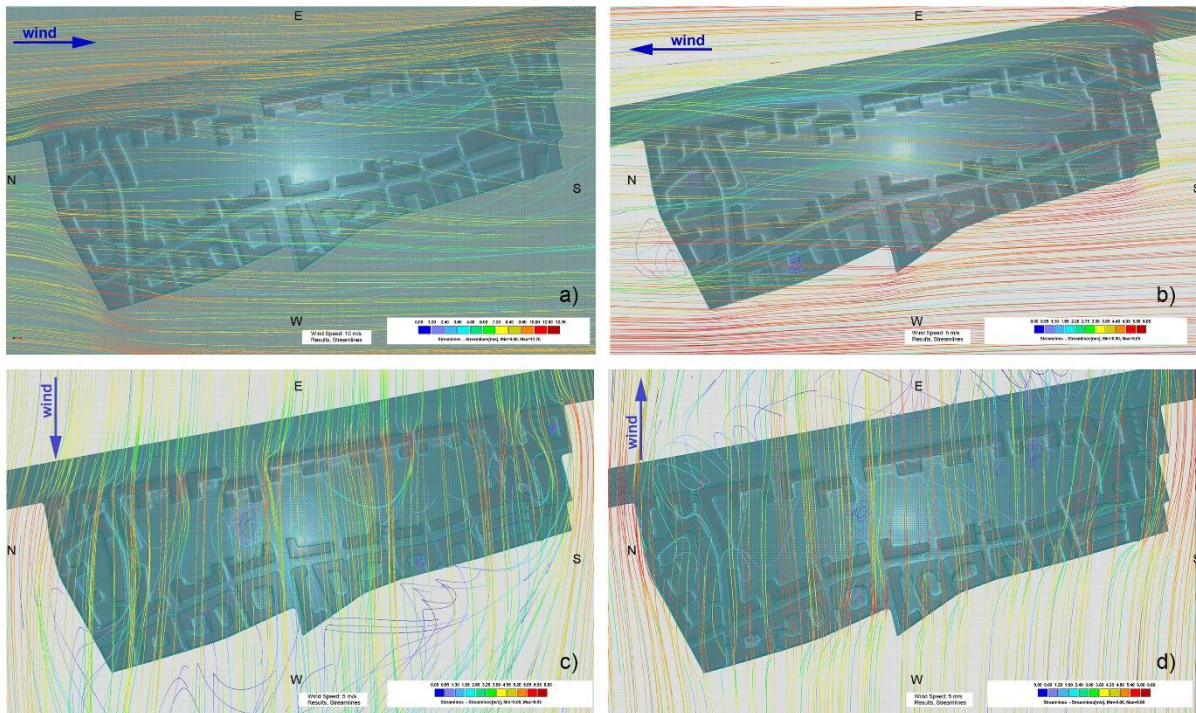


Figure 4. Wind streamlines (a. north at 10m/s; b. south at 5m/s; c. east at 5m/s; d. west at 5m/s).

As mentioned above the last simulation preserve the same wind speed at 5m/s prevailing from the west (270°). Wind speed ratio inside the future public park areas varies from 0.1m/s-4m/s. Investigating the velocity field plan the results show 58% of the future park area is affected by wind high-velocity 1-2m/s with a peak wind velocity at 4.47m/s. Critical high wind velocities appear at these areas; (a1=4.47m/s); (a2=3.20m/s); (a3=2.76m/s) (Figure 2d). Several vortices are created in this simulation (Figure 4c).

3.3 Pressure field

In the pressure field graphs, the playing area is created in the simulation b-(wind blowing from the south) and d-(wind blowing from the west). For tests running at 10m/s, results show the maximum dynamic pressure of 51.3Pa and the minimum -96.5Pa. (Figure 5a). It also reveals the lowest pressure field is also in the model-b with a maximum dynamic pressure of 12.7Pa and a minimum of -20.0Pa. (Figure 5b). The surface pressure in the building facades does not reveal any useful information to be used for evaluating the wind flow inside studied area.

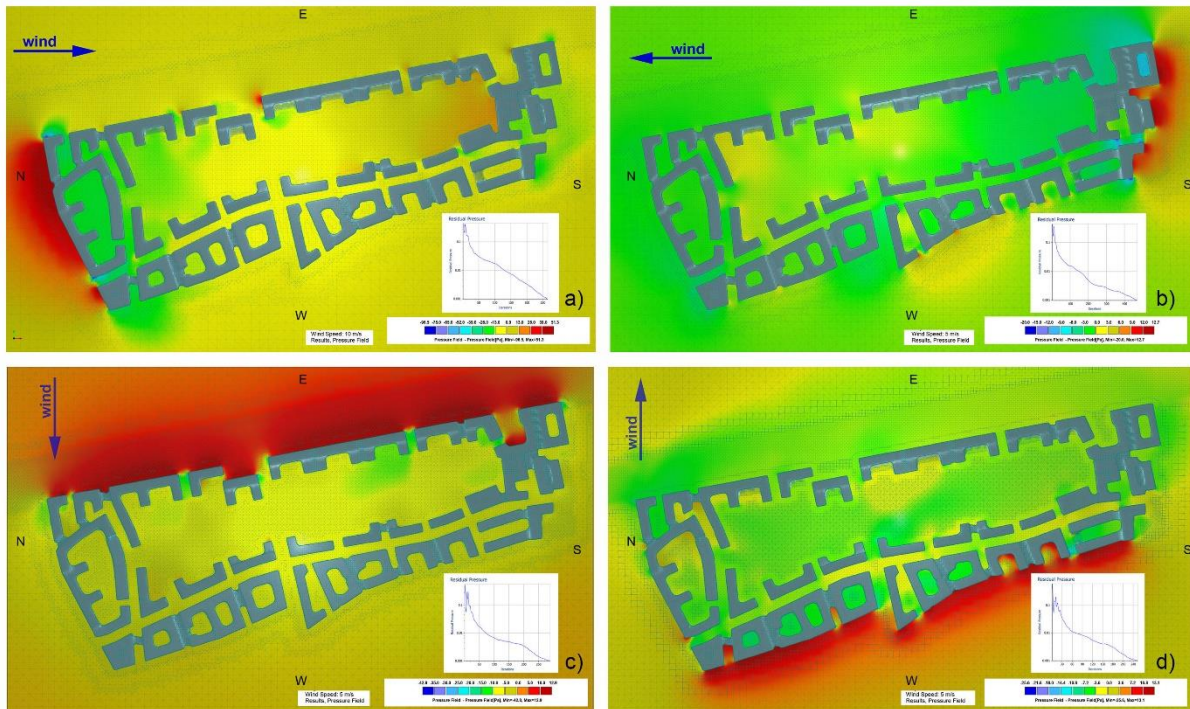


Figure 5. Dynamic pressure field (a. north at 10m/s; b. south at 5m/s; c. east at 5m/s; d. west at 5m/s).

4. Discussions

This paper has analyzed the wind speed generated in a public ambience. The studied area was unconventionally surrounded by tall buildings, and this fact raise our concern about wind flow issues. As mentioned above, the architectural proposal has not presented any study focused on the wind flow hence, we have been able to develop CFD as a method of evaluating the wind flow in the future public park area. Therefore, the short-term on-site investigation wasn't able since the master-plan we have evaluated is not yet been implemented. This study has come to important findings related to the air movement in and around the studied domain:

1. The worst-case scenario is more likely to happen in winter from November to February when the wind blows from the north (10m/s), (Figure 2a) In almost half of the area, the wind was 4-6m/s considered definitely unpleasant for sitting, moderated for strolling and good for traversing [30]. This means in most cases the area is not suitable for people seeking to relax. One of the most important factors that affect people's behavior seems to be the urban wind environment [33, 34]. As wind speeds increase, some variations can become more abrupt and of greater amplitude, such as "wind gusts" [35]. The wind gusts are defined as a short-duration (seconds) maximum of the fluctuating wind speed [36]. Hence, in the first scenario, we could discover also wind at high velocities (9m/s) but these were limited areas hence, considered a nuisance for most creative activity [28]. In this scenario, the leaves would sway creating unpleasant conditions for people standing nearby.

2. In every environmental condition and direction, the wind is not distributed in a uniform pattern, (Figure 2a). The way the air mass moves over and around the urban context is a complex fluid flow phenomenon [37]. Probably the reason for this variable is the presence of nonlinear building layout suggested in the master-plan. The difference is visible mostly in the first scenario when the wind blows from the north at 10m/s. Hence, two different approaches must be considered in the design concept for the same public park.

3. The presence of tall buildings in the park boundary was not common at these distances. These buildings direct the air at high velocity inward the public park. Tall buildings often show

captivating elegant profiles, but the higher they are, the stronger the wind blows on their top, [35]. Many studies emphasize the down-draught effect generated on high-rise buildings therefore, they are strongly influencing the wind flow causing discomfort at the pedestrian level [38]. Inspecting (Figure 3a) we could find a faster movement of the air above the ground because of the absence of the obstacles. The higher the building, the more wind at high velocity is captured and guided beneath the base of the building causing discomfort to pedestrians.

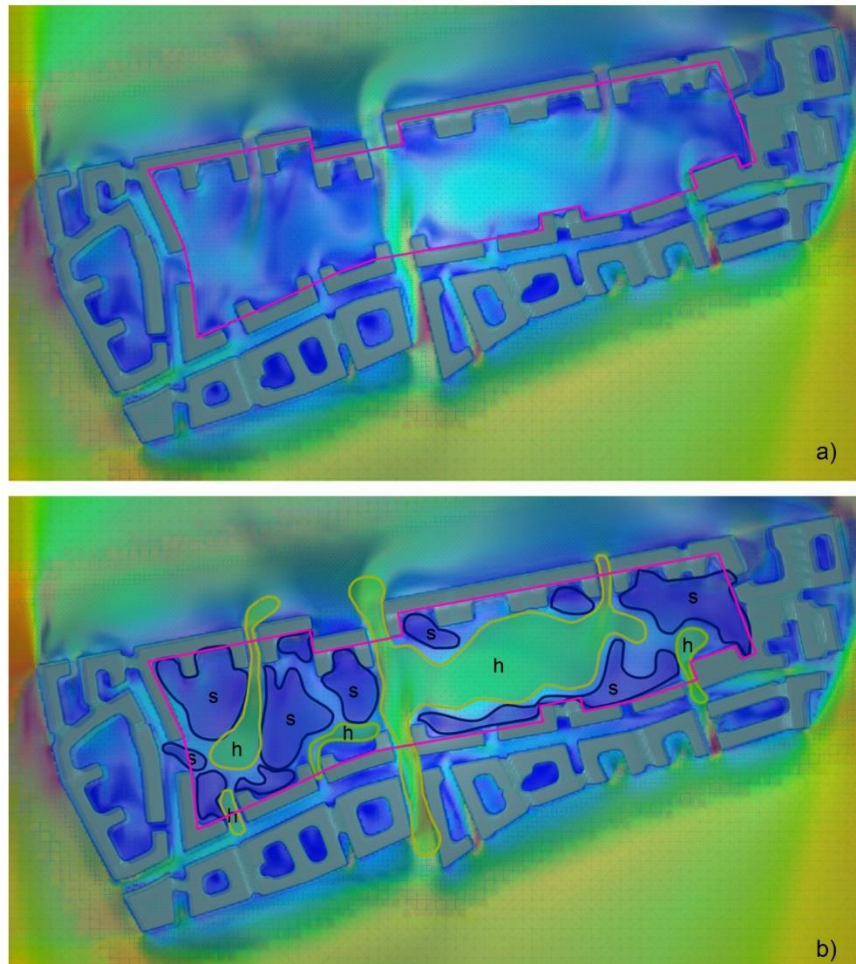


Figure 6. A hypothetical model of the park design. (h) – high speed areas; (s) – slow speed areas.

4. Wind at high velocities is obtained when the wind blows from the east, even at a lower speed (5m/s). The highest speed is generated in-between the buildings gap's (Figure 2c). The wind gains speed in the gaps due to the high pressure created in the building's facades [4]. (Figure 5c). (Figure 6c), reveal this increase in wind's pressure at the east, considering the wind finds no nearby barriers at that direction. High speed wind currents are created in the channel mostly by parallel facades and the sudden drop of pressure. The wind speed generated in the gaps wouldn't be difficult to people traversing, jogging or running but not comfortable for people sitting or resting [30], [28]. But channeling needs to be considered in higher speed prevailing winds.

5. This study provides design recommendations to avoid pedestrian discomfort. After picking up all the result, we could overlay all the graphs taken in all four scenarios in order to identify a hypothetical best-case scenario. In the (Figure 6), we have identified the high-velocity areas. Inside the green areas labeled "h" sitting and standing is unpleasant unless mitigation strategies (such as tree plants), are implemented. The blue areas labeled "s" show the slow speed areas in every wind condition. The following area reports a wind speed of 0.1m/s to 2m/s, which is

considered relevant to most creative activity [28]. Our simulations revealed in all cases, the absence of any dangerous area for pedestrians. The top speed observed in specific areas is 9m/s.

5. Conclusions

This paper was focused on wind conditions and pedestrian behavior in a public urban area. The urban context impact dramatically on urban wind patterns. Moreover, the urban wind is influencing pedestrians' wind comfort and safety. The purpose of this study was to analyze people's comfort and public space to suggest a pleasant outdoor environment. The CFD was used as an instrument to evaluate the wind impact on a public domain, included inside the pattern of the buildings. The effects of these architectural patterns in the wind conditions were discussed.

The architectural shapes are capable to impact at large the local wind by different aspects such as building dimensions, their orientation, urban density, structure articulations, etc. The study indicates that high velocity wind can be a nuisance for most creative activities in the outdoor public space. A decrease in wind speed, particularly during winter, would help urban habitants to extend their recreation time in the future park domain. This study attempts to provide urban designers with planning instruments to consider pedestrian safety and wind comfort during their creative process.

This paper provided a velocity map, (Figure 6b), for future recreational activities inside the current building pattern. Activities in the park could be designed according to the tolerated wind speed in this map. Hence, urban design impacts people's life quality.

Future research

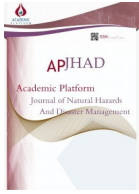
Mitigation strategies are typically recommended to improve the safety and comfort of pedestrians. Tree planting in the areas where wind speed exceeds 7-8m/s might be one of the mitigation strategies. Also, the mitigation strategies might consider a different design concept of the building units, with pedestrian comfort in mind. Other research must be done in order to improve the microclimate through trees plant typologies. They can both be used for mitigation strategies during winter and at the same time to enhance ventilation during the summer. Hence a study focusing on local season must be done in order to better evaluate the people's comfort.

6. References

- [1] United Nations. Department of Economic and Social Affairs. Population Division. World Urbanization Prospects. The 2009 Revision. CD-ROM. 2010.
- [2] UN. World Urbanization Prospects, and others: The 2018 Revision. UN. 2018.
- [3] Durgin FH, and Chock AW. Pedestrian wind levels: a brief review. *Journal of the Structural Division ASCE*, 1982;108(8):1751–1767.
- [4] Hala E. (2017) Turning the effect of urban wind into an asset: its impact in climate-sensitive urban design. *Proceedings of the International Conference for Civil Engineering*, In English, ICCE2017, 12-14 October 2017 Tirana Albania, pp.196. ISBN 978-9928-4429-2-5.
- [5] Moore N. *Dublin Docklands reinvented. The Post-Industrial Regeneration of a European City Quarter*; Four Courts Press, Dublin. 2008.
- [6] Bosselmann P, Arens E, Dunker K, Wright R, Sun, Wind, and Pedestrian Comfort: A Study of Toronto's Central Area. Center of Environmental Design Research, University of California. 1990.

- [7] Bosselmann P, Flores J, Gray W, Priestley T, Anderson R, Arens E, Kim J J. Sun, Wind, and Comfort: A Study of Open Spaces and Sidewalks in Four Downtown Areas. Berkeley, CA: Center for Environmental Design, University of California. 1984.
- [8] Arens E, Bosselmann P. Wind, Sun and Temperature—Predicting the Thermal Comfort of People in Outdoor Spaces. *Building and Environment* 1989;24(4): 315-20.
- [9] Gehl J. *Life Between Buildings. Using Public Space*, Island press, Washington, D.C. 2011.
- [10] Zacharias J, Stathopoulos T, Wu H. Microclimate and Downtown Open Space Activity. *Environment and Behavior* 2001;39: 660-84.
- [11] Jordan SC, Johnson T, Sterling M. Baker C. Evaluating and modeling the response of an individual to a sudden change in wind speed. *Building and Environment*, 2008;43: 1521-1534.
- [12] Stathopoulos T. Wind and comfort. In: 5 EACWE Proceedings, Florence, 2009;1–16.
- [13] Thorsson S, Lindqvist M, Lindqvist S. Thermal bioclimatic conditions and patterns of behavior in an urban park in Göteborg, Sweden. *International Journal of Biometeorology*, 2003;48: 149–156.
- [14] Emmanuel R, Rosenlund H, Johansson E. Urban shading—a design option for the tropics. A study in Colombo, Sri Lanka. *International Journal of Climatology*, 2007;27: 1995–2004.
- [14] Blocken B, Carmeliet J. Pedestrian wind conditions at outdoor platforms in a high-rise apartment building: generic sub-configuration validation, wind comfort assessment and uncertainty issues. *Wind and Structures*, 2008;11(1): 51–70.
- [15] Andrade H, and Alcoforado MJ. Microclimatic variation of thermal comfort in a district of Lisbon (Telheiras) at night. *Theoretical and Applied Climatology*, 2008;92(3–4): 225–237.
- [16] Qingyan (Yan) Chen. Using computational tools to factor wind into architectural environment design. *Energy and Buildings*, 2004;36: 1197-1209.
- [17] Blocken B, Janssen WD, Hooff J. CFD simulation for pedestrian wind comfort and wind safety in urban areas: General decision framework and case study for the Eindhoven University campus. *Environmental Modelling & Software*, 2012;30: 15-34.
- [18] Reiter S. Assessing wind comfort in urban planning. *Environment and Planning. Planning and Design*, 2010;37(5): 857-873.
- [19] Murakami S. Computational wind engineering. *Journal of Wind Engineering and Industrial Aerodynamics*. 1990;36(1): 517-538.
- [20] Gadilhe A, Janvier L, Barnaud G. Numerical and experimental modelling of the three-dimensional turbulent wind flow through an urban square. *Journal of Wind Engineering and Industrial Aerodynamics*. 1993;46-47: 755-763.
- [21] Blocken B, Persoon J. Pedestrian wind comfort around a large football stadium in an urban environment: CFD simulation, validation and application of the new Dutch wind nuisance standard. *Journal of Wind Engineering and Industrial Aerodynamics*, 2009;97(5–6): 255-270.
- [22] Hooff T, Blocken B, Harten M. 3D CFD simulations of wind flow and wind-driven rain shelter in sports stadia: Influence of stadium geometry”. *Building and Environment*, 2011;46(1): 22-37.
- [23] Wu H, Kriksic F, Designing for pedestrian comfort in response to local climate. *Journal of Wind Engineering and Industrial Aerodynamics*, 2012;104-106: 397–407.
- [24] Janssen WD, Blocken B, Hoof T, Pedestrian wind comfort around buildings: comparison of wind comfort criteria based on whole-flow field data for a complex case study. *Building and Environment*. 2012;59: 547-562.

- [25] Murakami S, Iwasa Y, Morikawa Y. Study on acceptable criteria for assessing wind environment on ground level based on residents' diaries. *Journal of Wind Engineering and Industrial Aerodynamics*, 1986;24: 1–18.
- [26] ASCE. *Outdoor Human Comfort and its Assessment: State of the Art*, Task Committee on Outdoor Human Comfort, American Society of Civil Engineers. 2003.
- [27] Bottema M. A method for optimization of wind discomfort criteria. *Build Environmental*, 2000;35(1): 1-18.
- [28] NEN 8100. *Wind comfort and wind danger in the built environment*. Netherland Standards. 2006.
- [29] Koss HH. On differences and similarities of applied wind comfort criteria. *Journal of Wind Engineering and Industrial. Aerodynamics*. 2006;94: 781-797.
- [30] Kusaka M, Setoguchi T, Watanabe N, Guo Zh, Paukaeva A. Human Behavior in Downtown Public Spaces during Cooling Periods in Winter Cities. *Journal of Civil Engineering and Architecture* 2018;12: 1-10.
- [31] Yang L, and Li Y. Thermal conditions and ventilation in an ideal city model of Hong Kong. *Energy and Buildings*, 2011;43: 1139-1148.
- [32] Memon RA, Leung DYC. Impacts of environmental factors on urban heating. *Journal of Environmental Sciences-China*. 2010;22: 1903-1909.
- [33] Crosbie MJ, Perry D, Smith Th. "Buildings at Risk: Wind design basics for practicing architects". The American Institute of Architects. 2008.
- [34] Suomi I, Vihma T. Wind Gust Measurement Techniques-From Traditional Anemometry to New Possibilities. *Sensors*, 2018;18(4): 1300.
- [35] Orlandi P. *Fluid flow Phenomena: A Numerical Toolkit*, Dordrecht, Kluwer. 2000.
- [36] Hala E., Nepravishta F., and Panariti A. (2019) The wind flow effects and high-rise buildings in urban spatial morphology. *Cities in Transitions, Proceedings of the 1st International Forum on Architecture and Urbanism*, 14-16 December 2017 Tirana Albania. Publisher: La scuola di Pitagora Editrice, pp 52-56, ISBN 978-88-6542-679-1, ISBN 978-88-6542-695-1.



Investigation of Effective Bending Rigidity Considering Different Code Approaches

Gokhan Dok¹ , Hakan Ozturk¹ , Aydin Demir¹ , Naci Caglar*¹ 

¹Faculty of Engineering, Department of Civil Engineering Sakarya University, Turkey

Received: / Accepted: 24.12.2019 / 09.06.2020

Abstract:

In the study, the nonlinear behavior of reinforced concrete (RC) structures was investigated considering effect of effective bending rigidity under seismic loads. The cross-sectional effective bending rigidity (EI_{eff}) of structural members was evaluated using different approaches of seismic design codes. The values of EI_{eff} given in Eurocode-8, Turkish Seismic Design Code (TSDC) 2007 and Turkish Building Earthquake Code (TBEC) 2018, were used in a case study and compared with the initial (uncracked) section rigidity. The nonlinear single mode pushover analysis was carried out to determine the nonlinear performance of a RC frame structure model in SAP2000. In nonlinear pushover analysis, the lumped plasticity and plastic hinge theory were used to define nonlinear behavior of the structural members. The plastic characteristics of structural members were also evaluated using moment-curvature relationship in Xtract. The dimension of cross-sections and reinforcing details were chosen considering the design requirements of TSDC 2007 and TBEC 2018. The structural performance of the RC frame models with different stiffnesses was compared with performance of the model in which initial rigidity used. The base reaction force vs. top displacement demand, story drifts, and plastic hinge mechanisms obtained from the analyses were selected as comparison criteria. It was observed in the analysis results that a remarkable difference occurred in force and displacement demand between the models using the different effective bending stiffnesses.

Key words: Effect of effective bending rigidity, nonlinear performance, reinforced concrete structure, pushover analysis

1. Introduction

Reinforced concrete (RC) structures might be exposed to different seismic effects during their service lives. Determination of the nonlinear behavior of these structures is the one of the most convenient ways to check structural safety. For this purpose, the structural behavior could be evaluated with different nonlinear analysis methods under the seismic effect [1-4]. To determine the proper analysis method for the nonlinear behavior of RC structures is very crucial. Pushover analysis is one of the most commonly used methods to evaluate performance of RC structures under earthquake loads [5-9]. In this method, the displacement demand of a structure is calculated by a monotonically incremental loading. This increase in seismic displacement demand should be proceeded until a reliable target displacement. Besides, the force distribution due to lateral earthquake load is taken into account in a compatible form of fundamental first mode on the structure at every story level [10-12]. In the last increment step of target displacement, demands of base shear force, top displacement, and story drifts are

* Corresponding Author,

Address: Faculty of Engineering, Department of Civil Engineering Sakarya University, 54187, Sakarya TURKEY. E-mail address: caglar@sakarya.edu.tr, Phone: +902642955752

calculated to determine plastic deformations on each structural element. The plastic deformation intensity of each structural element is crucial for the assessment of RC structures in a nonlinear analysis. In this analysis, nonlinearity of each structural element affects directly the nonlinear behavior and performance level of RC structures. The nonlinearity of elements is defined by using plastic hinge theory with lumped plasticity. Plastic deformations are observed in a plastic hinge length at the both ends of structural elements. Additionally, it is assumed that the other parts of each structural element exhibit elastic behavior [13].

On the other hand, cross-sectional properties and behavior of these elements should be known to define nonlinear behavior of RC structural elements. Moment-curvature (MC) relationship is one of the best theoretical approaches to represent the nonlinear behavior of RC elements [14-15]. Additionally, the moment-curvature relationships should be used with interaction surfaces of vertical structural elements (column, shear wall etc.). The interaction surfaces are evaluated according to the different levels of axial forces in a column or shear wall. Thus, the positive/negative effect of compression and tension forces can be taken into account by the cross-sectional analysis of a column or shear wall.

Additionally, flexural stiffness and ductility of a section can be determined using moment-curvature relationship [16]. The slope of MC relationship represents the effective bending rigidity (EI_{eff}) and is calculated by dividing the value of yield moment to the value yield curvature. Mander confined and unconfined concrete models which are one of the most commonly used models in literature to represent material behavior, are used in cross-sectional MC analysis [17]. The effect of confinement is considered for each different section.

In the study, twelve incremental single mode pushover analyses were carried out using the different values of EI_{eff} defined in different design codes. These stiffnesses were calculated according to Eurocode-8, Turkish Seismic Design Code for buildings 2007 and Turkish Building Earthquake Code 2018 (TSDC 2007 and TBEC 2018) [18-20]. Besides, Xtract [21], which is a commercial sectional analysis program was used to determine EI_{eff} of the sections and they were compared in pushover analysis. All pushover analyses were performed by using Sap2000 a commercial general finite element software [22]. According to the result of pushover analysis, the design code approaches were assessed by considering the variation of the structural demands and performances.

2. Numerical Modelling and Parametric Study

In the study, an incremental single mode pushover analysis is used to determine nonlinear displacement demand of structures under seismic loads. The displacement demand affects nonlinear deformations of structural elements directly. These deformations are evaluated using plastic hinge properties of each cross-section. Therefore, defining plastic hinge properties of cross sections is very important to determine nonlinearity of structures in pushover analysis. In this part of the study, modelling methodology is explained to create a numerical model in nonlinear analysis. In this research, twelve pushover analyses were applied to an eight-story RC structural frame model to determine effect of EI_{eff} on RC structures. In the analyses different EI_{eff} is used considering different code approaches to compare obtained results with the values obtained from Xtract. The analysis results are compared in terms of nonlinear force-displacement relationship, story drifts, plastic hinge rotation, and variation of first fundamental vibration mode of the structure.

2.1. The Model of Superstructure

Three dimensional (3D) numerical models of an eight-story RC structure, designed according to the minimum design requirements defined in TSDC 2007, are created. The dimensions of each cross-section, and reinforcement details of the structural elements are tabulated in Table 1. Moreover, reinforcement details of structural elements, and general layout and plan views of 3D numerical models are given in Figures 1 and 2 respectively.

Table 1. Material and section properties of superstructure

Name	Element	Concrete –Reinf.	Mod. of Concrete (MPa)	Mod. of Reinf. (MPa)	Yield Strength of Reinf. (MPa)	Dimensions (mm)	Long. – Trans. Reinforcement (mm)
C1	Column	C25 – S420	30000	210000	420	600x250	10 Φ 16– Φ 10/100
C2	Column	C25 – S420	30000	210000	420	250x600	10 Φ 20– Φ 10/100
C3	Column	C25 – S420	30000	210000	420	600x250	10 Φ 20– Φ 10/100
B1	Beam	C25 – S420	30000	210000	420	250x500	6 Φ 16– Φ 10/100
B2	Beam	C25 – S420	30000	210000 </td <td>420</td> <td>250x500</td> <td>6Φ20–Φ10/100</td>	420	250x500	6 Φ 20– Φ 10/100

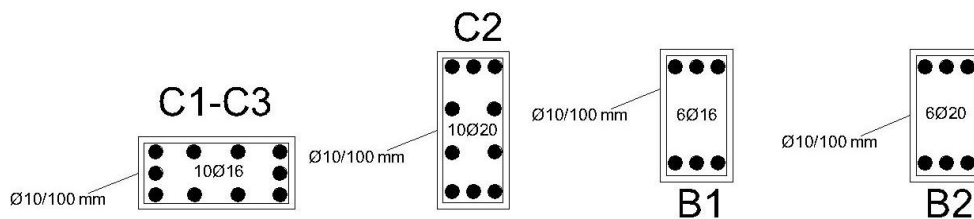


Figure 1. Reinforcement details of structural elements

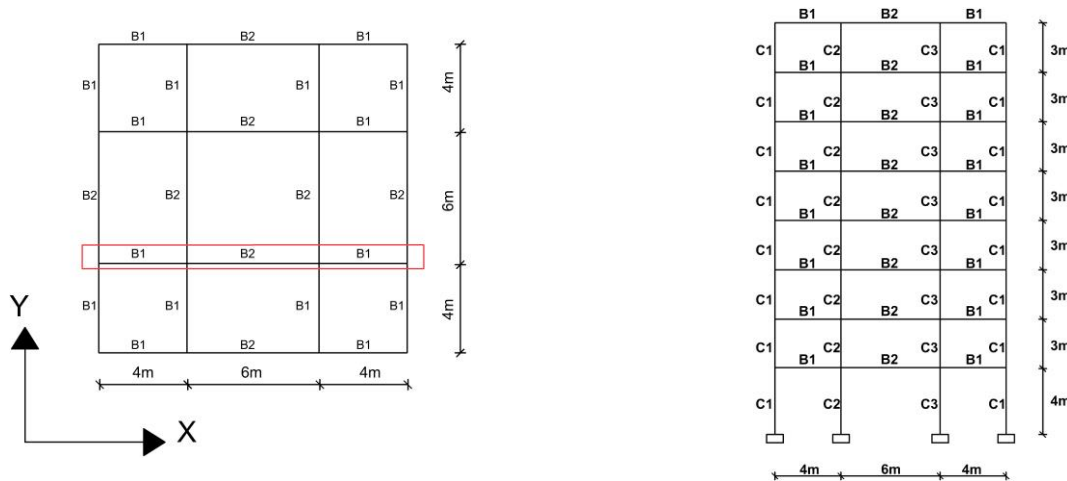


Figure 2. Plan view and general layout of structural model

It is assumed that all structural systems are constructed in a high seismic risk zone (first-degree). Therefore, they must have high ductility. Moreover, soil conditions are considered as a Z4 soil class defined in TSDC 2007 for all structural models. In TSDC 2007, it is proposed that the peak ground acceleration (A_0) should have taken as 0.4g for the first-degree seismic risk zone. Elastic-perfectly plastic behavior is defined for the stress-strain relationship of steel reinforcement. Mander [17] confined and unconfined approaches are used for the nonlinearity of concrete material.

Plastic hinge properties of each cross section are calculated by considering reinforcing details. These plastic hinges are determined according to the moment-curvature relationship of each different cross-section assigned to the end points of structural elements. The frame in red box in Fig. 2 is selected as a reference axis to be able to compare analysis results. The moment-curvature relationships of all beam and column sections are given in Figure 3.

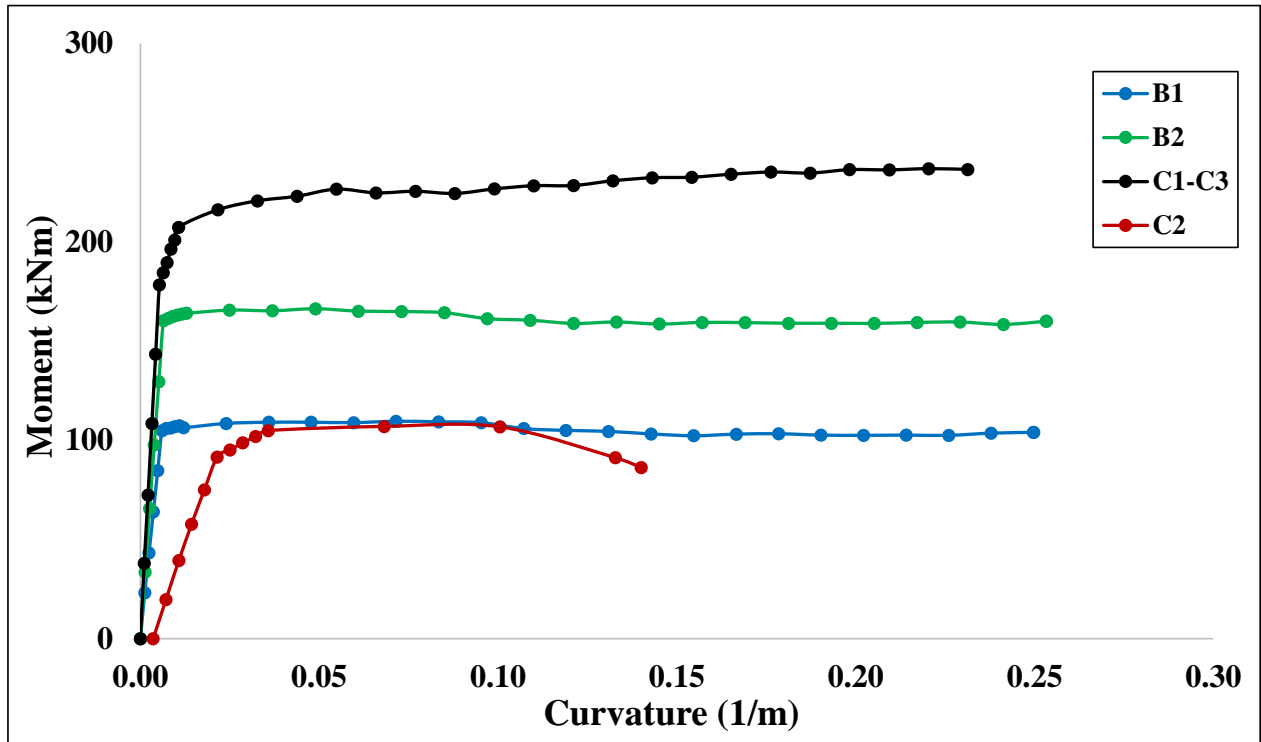


Figure 3. Moment-curvature relationships

The plastic hinge properties of beams (M3) are defined considering moment-curvature relationships. On the other hand, the flexural moment capacities are changed according to the axial force level (tension or compression) on the RC columns. Therefore, the plastic hinge properties of columns (P-M2-M3) are defined in accordance with interaction surfaces of columns. The axial forces are calculated by using interaction surfaces of columns in plastic zones. The interaction surfaces are obtained by using section designer module of SAP2000. In Sap2000, the moment-curvature analysis and the different interaction surfaces of columns are determined by using this module. During the pushover analysis, the SAP2000 software uses the default and adaptive axial forces obtained from interaction surfaces in the section designer module instead of user defined values. The interaction surfaces of columns are presented in Figure 4.

In nonlinear pushover analysis, the conventional load combinations used in linear analysis are not used to represent lateral loading procedure. In this method, the displacement demand of a structure is calculated by a monotonic incremental loading. This increase in seismic displacement demand should be proceeded until a reliable target displacement. Besides, the force distribution due to lateral earthquake load is taken into account in a compatible form of the fundamental first mode of the structure at every story level. In the last step of target displacement; the demand of the base shear force, top displacement, and story drifts are calculated to determine plastic deformations of each structural element. In pushover analysis, the initial conditions of superstructure are defined as a deformed model under the weight of

superstructure. To perform these initial conditions, a nonlinear load case is defined by using the weight of superstructure ($G+nQ$) and checked the plasticity of RC structure. The dead loads, live loads and participation factor for live loads are denoted by using symbol G , Q and n , respectively. The value of n is assumed as 0.3 for the buildings. The pushover analysis is only carried out in the “X” direction of structures and the results are compared by considering plastic deformations of RC structures in this direction.

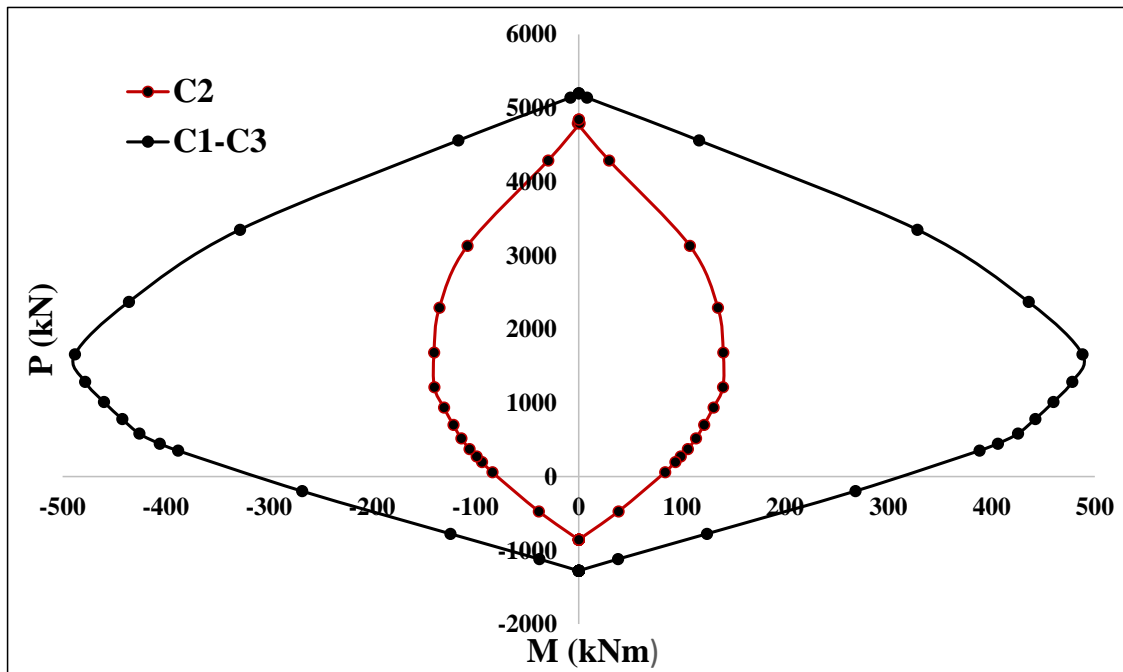


Figure 4. Axial force (P , kN)-moment (M , kNm) interaction surfaces

2.2. Parametric study

The EI_{eff} of cracked sections is a very crucial parameter in nonlinear analyses. That parameter is defined as different values in different earthquake design codes. The aim of this study is to determine different EI of cracked sections considering earthquake code approaches. Moreover, values of EI_{eff} are compared to the values obtained from Xtract program. In the study, the EI of cracked section are calculated by considering the values defined in TSDC 2007, Eurocode-8, and TBEC 2018 seismic codes. The cracked-section EI is defined as a constant value for frame beam and column elements in Eurocode-8. In TSDC 2007, the EI_{eff} for a frame beam element is constant like others. For the column elements, this value must be calculated between 0.4-0.8 of initial rigidity according to the axial load level of columns. The envelope value of axial force obtained from the mode superposition method is taken account into to determine EI_{eff} value of TSDC 2007. The envelope axial loads are calculated by using the sufficient number of modes in which the participation ratio of mass is or above %95. In Xtract program, the value of EI_{eff} can be calculated by a step by step solution for all beam and column elements. In the section analyses any axial load level can be taken into account for all column sections. The moment-curvature relationships are used when these values are calculated in Xtract. In every step of sectional analysis, the deformation of reinforcement, confined and unconfined concrete are controlled according to a limit deformation which is defined for failure mode of the material. In TBEC 2018, the design EI_{eff} values used in a design of a new building are defined in section 4 (Design Principles of Strength Based Design of The Structures under Earthquake Effect) and these values are constant for frame elements such as columns and beams. However, the performance EI_{eff} values used in a seismic performance evaluation of an existing building are

calculated by using Eqs. 1 and 2. These equations are defined by performing the moment-curvature analysis in section 5 (Assessment and Design Principles of Displacement Based Design of the Structures under Earthquake Effect). In Eq. 1, L_s , M_y and θ_y represent the shear span (can be assumed as the half of span), yield moment, and rotation respectively. The compressive strength of concrete and yield strength of reinforcements are defined by using f_{cc} and f_{ye} . In Eq. 2, ϕ_y , h and d_b indicate the yield curvature (obtained from moment-curvature analysis), height of the section and average diameter of tension reinforcement, respectively. The coefficient η is a constant value and should be accepted for a frame element such as column and beams as 1. Each EI_{eff} value for Xtract and other earthquakes codes is given as a ratio of initial rigidity in Table 2.

$$EI_{eff} = \frac{M_y}{\theta_y} \frac{L_s}{3} \quad (1)$$

$$\theta_y = \frac{\phi_y L_s}{3} + 0.015\eta \left(1 + 1.5 \times \frac{h}{L_s} \right) + \frac{\phi_y d_b f_{ye}}{8\sqrt{f_{cc}}} \quad (2)$$

Table 2. Material and sectional properties of superstructure

Name	Initial EI (kNm ²)	EI_{eff} of Eurocode-8	EI_{eff} of TSDC 2007	Design EI_{eff} of TBEC 2018	Performance EI_{eff} of TBEC 2018	EI_{eff} of Xtract
C1	135000	0.5	0.48-0.62	0.7	0.06	0.33-0.35
C2	23438	0.5	0.78	0.7	0.12	0.34
C3	135000	0.5	0.74	0.7	0.06	0.36
B1	78125	0.5	0.4	0.35	0.05	0.22
B2	78125	0.5	0.4	0.35	0.06	0.32

As it can be seen in the Table 2 that the performance approaches of TBEC 2018 are very conservative compared to the other values of EI_{eff} . It can be said that an accurate performance assessment cannot be determined by using these performance EI_{eff} values. Probably, the results of pushover analysis could be irrational compared to the other results. Therefore, in the study the design EI_{eff} values of TBEC 2018 are used due to being a more realistic assumption than the performance EI_{eff} values. These values are defined in structural models when pushover analyses are carried out in Sap2000. The nonlinear force-displacement relationship obtained from pushover curves, story displacements and drifts, plastic hinge rotation, and variation of first fundamental vibration mode of structure are selected as parameters to make a comparison between analysis results.

3. Results

3.1. Pushover curves

In the study, the pushover curve is used to explain the relationship between base shear force and roof displacement in a nonlinear analysis. In numerical analysis, displacement and force demand of structures which are obtained from pushover curves are compared in Figure 5, 6 and 7. Moreover pushover curves are also used to determine performance level of the each numerical model. In the analysis, four different EI_{eff} ratio according to the initial EI obtained from different design codes, are used and compared using pushover analysis. Firstly, only the EI_{eff} of beams are changed while the columns are considered as having a constant value of EI (initial value). Secondly, only the EI_{eff} of columns are changed as the EI_{eff} of beams are accepted as constant value (initial EI). In last part of the study, the calculated EI_{eff} calculated from design

codes and obtained from Xtract are used for both beams and columns. The results obtained from the analyses are compared in Figure 5, 6 and Figure 7.

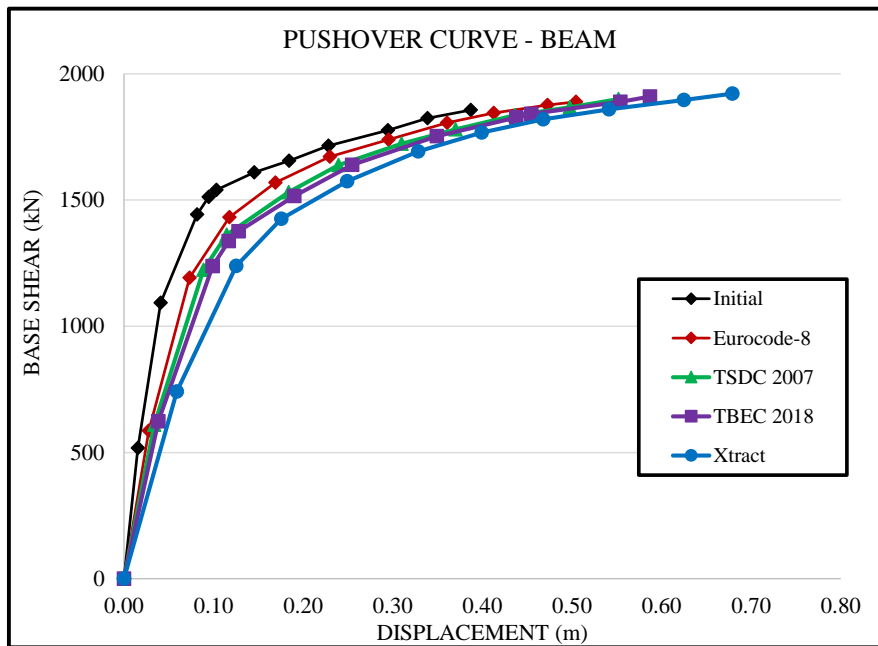


Figure 5. Pushover curves for model changed EI of only beams

When the analysis results are compared, the nonlinear force and displacement demand increases when calculated EI_{eff} obtained from Xtract is taken into account in the nonlinear analysis. Additionally, yield force and displacement change in different design code approaches. As it can be seen in the figures, the force and displacement demand of structural models using the EI_{eff} of different design codes become approximately similar. However, these demands are conservative with respect to the results of the structural model using the EI_{eff} of Xtract. Therefore, all the structural models reach to failure due to larger force and lesser displacement demand when the results of structural model using the EI_{eff} of Xtract are compared. It can be said that the models of Xtract show more ductile behavior with respect to the other structural models considering force and displacement demand.

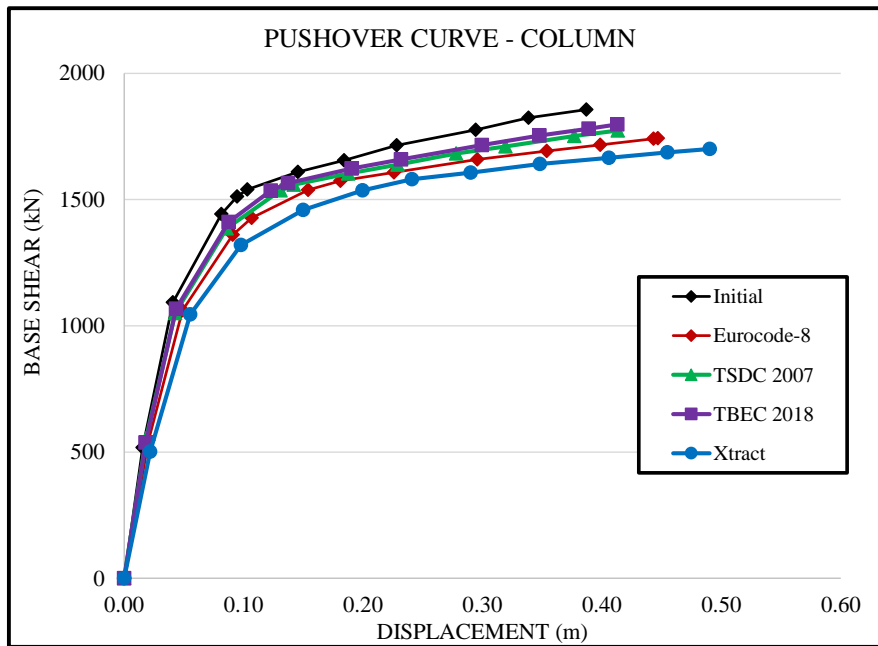


Figure 6. Pushover curves for model changed EI of only columns

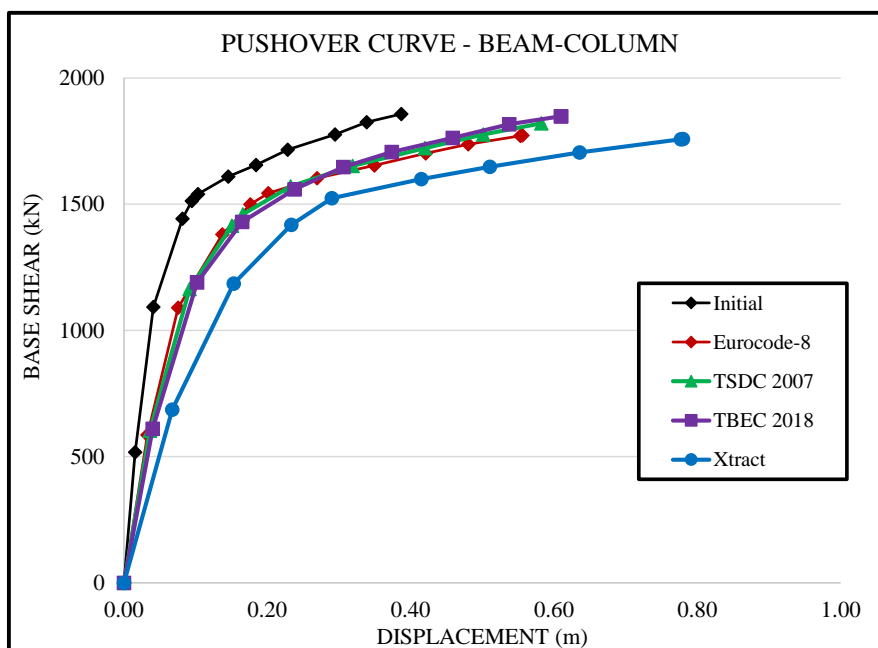


Figure 7. Pushover curves for model changed EI of both beam and columns

3.2. Structural demands

The results of pushover analyses are presented in Table 3. The difference in base shear, roof displacement, displacement ductility, and period of fundamental mode for different structural models are tabulated Table 3 considering different code approaches. Determination of target displacement values is the most crucial part of the nonlinear analysis. The plastic deformations of RC elements obtained from nonlinear analysis are calculated according to that target displacement values. These plastic deformations are used to determine the accurate nonlinear performance level of structures. Target displacements are calculated by means of measuring horizontal deflection value at the top of structures. The variations between structural models are shown for models whose EI_{eff} is changed for beams, columns, both beam and columns

separately. As it is expected, the combined use of the effective bending stiffnesses of columns and beams leads to increase in the first free vibration period of the structures. Similarly, the displacement demand increases due to the use of EI_{eff} for beams and columns together for each structural model.

Table 3. Variation of structural demands

Model		Initial	Eurocode-8	TSDC 2007	TBEC 2018	Xtract
Beam	Base Shear (kN)	1857	1890	1900	1910	1922
	Roof Disp. (m)	0.39	0.50	0.55	0.59	0.68
	Period T (s)	1.25	1.55	1.67	1.75	1.97
	Ductility	3.8	4.2	4.8	5.1	5.5
Column	Base Shear (kN)	1857	1743	1774	1798	1701
	Roof Disp. (m)	0.39	0.45	0.41	0.41	0.49
	Period T (s)	1.25	1.41	1.33	1.32	1.54
	Ductility	3.8	4.2	4.8	4.7	5.1
Beam-Column	Base Shear (kN)	1857	1773	1821	1849	1759
	Roof Disp. (m)	0.39	0.56	0.58	0.61	0.78
	Period T (s)	1.25	1.71	1.75	1.82	2.26
	Ductility	3.8	3.2	3.9	3.7	4.1

Additionally, as the displacement demand increases, the displacement ductility decreases due to combined use of EI_{eff} for beam and columns. As it can be seen in Table 3, the EI_{eff} of columns is more effective on the dynamic characteristics and seismic demand of the structure with respect to the EI_{eff} of beams. On the other hand, the first free vibration periods of the structural models using the performance EI_{eff} of TBEC 2018 change between 4-6 s. Moreover, the displacement demand is found to be between 1-2 m. The level of displacement demand and first free vibration period prove that the use the performance EI_{eff} of TBEC 2018 causes unreasonable analysis results for a multi-degree structural system. Therefore, the performance approach of EI_{eff} in TBEC 2018 should be revised considering dynamic characteristics and structural demands.

3.3. Story drifts

Story drift is calculated by dividing the difference between horizontal deflection of top and bottom of a story to the height of this story. The variations of story drifts and displacements are shown in Figure 8, 9 and 10.

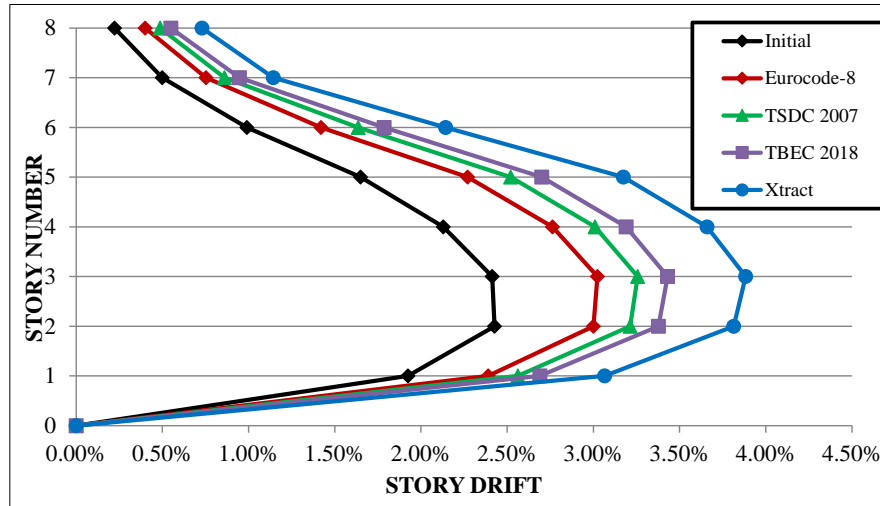


Figure 8. Story drifts for model changed EI of only beams

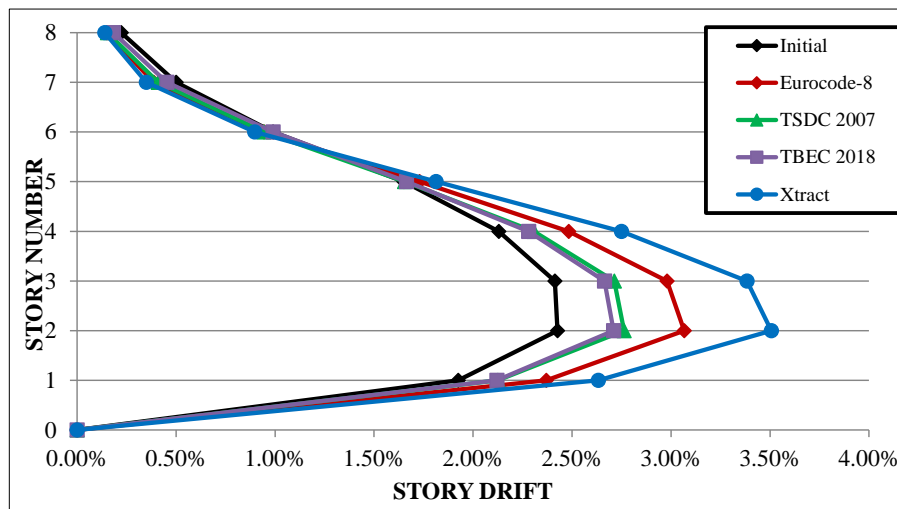


Figure 9. Story drifts for model changed EI of only columns

The story drift is one of the most direct parameters to make an assessment about the nonlinear performance level of a structure. In different earthquake design codes of different countries, some limitations are defined for story drifts while determining performance level of structures. The limitations of TSDC 2007 are used in this study and defined for immediate occupancy (IO), life safety (LS) and collapse prevention (CP) performance levels as 2%, 3% and 5% respectively. The difference in story drifts obtained from different structural models are calculated according to the story displacements. The difference in story drift ratios is more apparent when the EI_{eff} values of beams are only used. The design code approaches are very similar to determine story drift ratios. Therefore, the displacement demand of each structure in which the EI_{eff} of design codes are used, are approximately same. Additionally, the story drift ratios in the structural model using the EI_{eff} of seismic codes are conservative when the results of structural model with the EI_{eff} of Xtract are compared. According to the results of story drifts, it can be deduced that the structure can reach to the different performance level because of

application of the different EI_{eff} assumptions. In addition, the EI_{eff} obtained from the Xtract could be a more realistic to reach to the accurate performance of structures. Besides, as it can be seen in the Figs. 8, 9 and 10 that the most critical values of story drift ratios occur on the first three stories of the structures in which the first free vibration period is dominant.

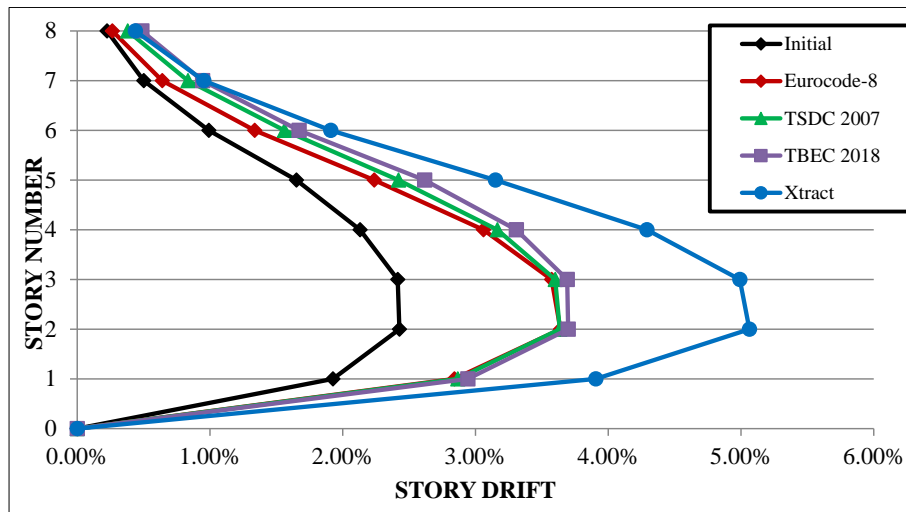


Figure 10. Story drifts for model changed EI of both beam and columns

3.4. Plastic Hinge Mechanisms

In earthquake design codes, column-beam connections are defined as one of the most crucial parts of a structure under seismic loads. To prevent brittle collapse, there are some special design rules for these connections. The strong column - weak beam analogy is generally proposed to be able to make a more ductile design for RC structures. In the study, analysis results showed that this analogy couldn't be provided due to different approaches of design codes. Moreover, some new plastic hinge mechanism can be observed in a structural system according to the values of EI_{eff} . By means of using different EI_{eff} approaches, these plastic hinge rotations can increase when the results are compared. For instance, the differences in plastic hinge formation mechanisms are shown in Figure 11. As it can be seen in Figure 11, the structural models reach to the failure mechanism with a different number of plastic hinges. In addition, the plastic deformation levels of plastic hinges are different according to the use of the different EI_{eff} . The color of pink is used to represent the yield deformation of structural elements. The color of blue, turquoise and green represent the performance of immediate occupancy (IO), life safety (LS) and collapse prevention (CP), respectively. According to the results of pushover analysis, the number and distribution (%) of the plastic hinges are presented for beams and columns in Table 4. The number and distribution of plastic hinges are classified in accordance with the performance levels defined in the seismic design codes.

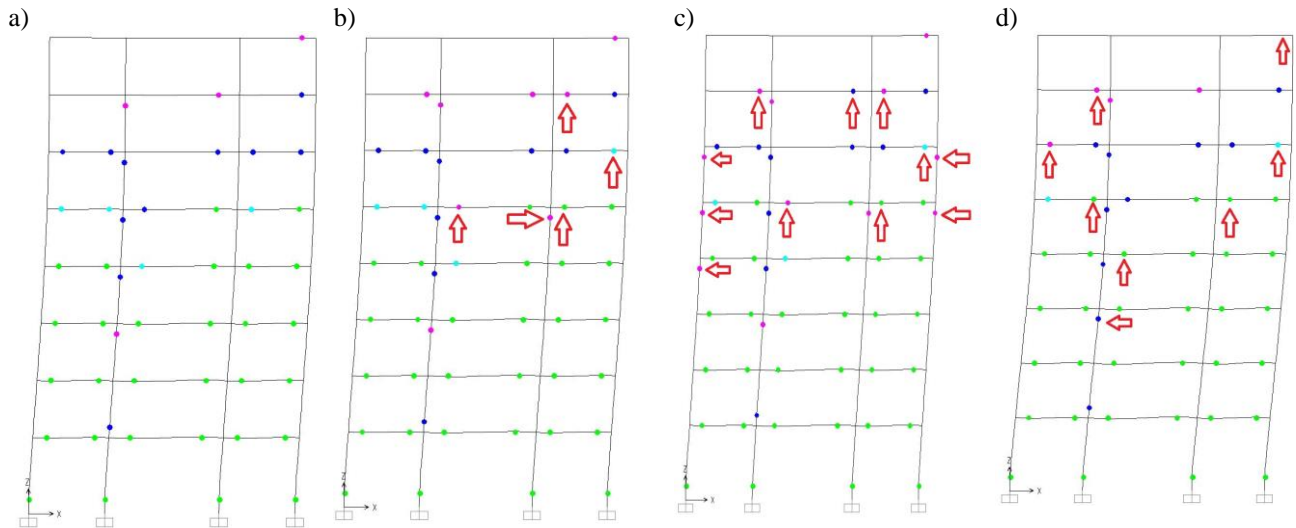


Figure 11. Plastic hinge formation a) Eurocode-8 b) TSDC 2007 c) TBEC 2018 d) Xtract

Table 4. The plastic hinge distribution of beams and columns for each performance level

	Level of plastic hinge	Beam		Column		Number of plastic hinge for failure of structure
		Number	%	Number	%	
Eurocode-8	Yield	2	4	2	4	48
	IO	7	15	4	8	
	LS	4	8	0	0	
	CP	25	52	4	8	
TSDC 2007	Yield	5	10	3	6	51
	IO	5	10	4	8	
	LS	4	8	0	0	
	CP	26	51	4	8	
TBEC 2018	Yield	4	7	7	13	55
	IO	6	11	4	7	
	LS	3	5	0	0	
	CP	27	49	4	7	
Xtract	Yield	3	6	1	2	49
	IO	5	10	6	12	
	LS	2	4	0	0	
	CP	28	57	4	8	

When the results of plastic hinges are compared, the strong column-weak beam approach is achieved due to the fact that most of the plastic hinges are formed in the beams. The plastic deformation of columns using the EI_{eff} of TSDC 2007 and TBEC 2018 are larger than the plastic deformations of other models. However, the number of plastic hinge mechanisms on beams is less than the other structural models in which different approaches are used. Therefore, the structural model using the EI_{eff} of Xtract can be accepted as the most ductile model because it reaches to the largest displacement demand with the least number of plastic hinges. Besides, the behavior of structural model using the initial EI is approximately elastic and reaches to a failure mechanism with only two plastic hinges.

4. Conclusions

In the study, the nonlinear behavior of reinforced concrete (RC) frames considering effect of effective bending rigidity under seismic loads is investigated. The cross-sectional effective bending rigidities (EI_{eff}) of structural members are determined using different approaches of seismic codes (Eurocode-8, TSDC 2007 and TBEC 2018). Twelve incremental single mode pushover analyses are carried out using the different values of EI_{eff} . The structural performance of RC frames with different stiffness is compared. Base reaction vs. force-top displacement demand, story drifts, plastic hinge mechanisms, periods, ductility, and roof displacements obtained from the analysis are selected as the comparison criteria. The effect of EI is seemed that different approaches of codes can cause a different assessment for same structures in nonlinear analysis. As the EI_{eff} decreases due to the code assumptions, performance levels of structures changes in numerical models negatively. Moreover, the numerical model whose EI_{eff} value calculated with Xtract program has more displacement capacity than other numerical models whose EI_{eff} defined according to the relevant design codes. From the analysis results, the following conclusions can be deduced:

- 1) When the pushover curves are compared, structural systems exhibit different displacement and force demands. The numerical model whose EI calculated with Xtract is less rigid than the other models. The most rigid model becomes the one EI_{eff} is not considered. The models on which EI_{eff} is considered only on beams or columns performed very similar behavior when the criteria of EuroCode-8, TSDC 2007, and TBEC 2018 are taken into account. On the other hand, those results remained between the results of initial EI and Xtract analysis.
- 2) It is seemed that the roof displacement and the displacement demand become bigger as the rigidity of structure decreases. Besides, the greatest displacement demand occurs in a numerical model whose EI_{eff} calculated with Xtract. This numerical model represents more ductile behavior than the others as well. While the minimum roof displacements were obtained from the models in which EI_{eff} is disregarded, the results obtained from seismic code approaches stayed between that values.
- 3) The story drifts can reach critical limit values with different assumptions of EI_{eff} . The difference in story drifts between numerical models decreases at the top of structures. The critical difference generally occurs at the first three stories. The results of story drifts can be observed apparently when the EI_{eff} of only beams are changed.
- 4) When the effect of EI_{eff} is taken account into in a nonlinear analysis, it is observed that some beam mechanism may change to column hinge mechanism for the numerical models. Plastic hinge rotations can reach high values with the increase in displacement demands. The differences between models are more apparent when the EI_{eff} of columns and beams are changed concurrently.
- 5) When the periods of the structural systems are evaluated, along with the decrease in EI_{eff} values the periods increase dramatically due to decrease in rigidity of the system. As the maximum period was observed in the models on which EI_{eff} values calculated by Xtract, the minimum value was obtained on the model EI_{eff} was not considered.

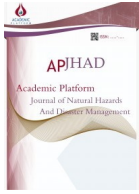
In the study, it is deduced that the structural performance of load bearing systems changes significantly according to use of different EI_{eff} . The important variations are observed on periods, ductility, roof displacements, and base shears of the building as well. The relevant

seismic codes used in this study become generally conservative in this regard. However, the results obtained from TBEC 2018 seem meaningless since it gives very small EI_{eff} values. Moreover, according to the analysis results, it is seen that EI_{eff} values of columns have a more significant effect than beams on the system. Lastly, while calculating the EI_{eff} values, the axial load on column members should be taken into account since it affects moment-curvature behavior of the sections significantly.

References

- [1] Priestley, M.J.N., 2000, Performance Based Seismic Design, 12th World Conference on Earthquake Engineering, Auckland, New Zealand, January-February 2000.
- [2] Fajfar, P., A Nonlinear Analysis Method for Performance-Based Seismic Design. *Earthquake Spectra*, 16(3), 573–592, 2000, DOI: 10.1193/1.1586128
- [3] Fajfar P. (2002) Structural analysis in earthquake engineering – A breakthrough of simplified non-linear methods. Paper No. 843, Proceedings of 12th European Conference on Earthquake Engineering, London.
- [4] M.N. Fardis (ed.), *Advances in Performance-Based Earthquake Engineering, Geotechnical, Geological, and Earthquake Engineering* 13, DOI 10.1007/978-90-481-8746-1, Springer, 2010.
- [5] Krawinkler H., Seneviratna G.D.P.K, Pros and cons of a pushover analysis of seismic performance evaluation. *Engineering Structures* 20(4–6), 452–464, 1998.
- [6] M.N., Aydinoglu, An Incremental Response Spectrum Analysis Procedure Based on Inelastic Spectral Displacements for Multi-Mode Seismic Performance Evaluation, *Bulletin of Earthquake Engineering* 1: 3–36, 2003.
- [7] A. Vijayakumar, D.L.V., Babu, Pushover Analysis of Existing Reinforced Concrete Framed Structures, *European Journal of Scientific Research*, ISSN 1450-216X, 71, 2, 2012, 195-202.
- [8] Duan, H. and Hueste M.B.D., Seismic performance of a reinforced concrete frame building in China *Engineering Structures*, 41, 77-89, 2012, DOI 10.1016/j.engstruct.2012.
- [9] Sung, Y.C., Lin, T.K., Hsiao, C.C. et al. Pushover analysis of reinforced concrete frames considering shear failure at beam-column joints. *Earthq. Eng. Eng. Vib.* 12, 373–383 (2013). DOI 10.1007/s11803-013-0179-8.
- [10] Chopra AK, Goel RK (2001): Modal pushover analysis of sac buildings, California.
- [11] Kim, S., & D’Amore, E., Push-over Analysis Procedure in Earthquake Engineering. *Earthquake Spectra*, 15(3), 417–434, 1999, DOI 10.1193/1.1586051.
- [12] A.K., Chopra, R.K., Goel, A modal pushover analysis procedure for estimating seismic demands for buildings *Earthquake Engng Struct. Dyn.* 2002; 31:561–582, DOI: 10.1002/eqe.144.
- [13] Inel, M., Ozmen, H.B. Effects of plastic hinge properties in nonlinear analysis of reinforced concrete buildings, *Engineering Structures* 28-11, 2006, 1494-1502 DOI 10.1016/j.engstruct.2006.01.017.
- [14] Caglar, N., Demir, A., Ozturk, H. and Akkaya, A. (2015). A new approach to determine the moment-curvature relationship of circular reinforced concrete columns. *Computers and Concrete*, Vol.15, pp.321-335. DOI: 10.12989/cac.2015.15.3.321
- [15] F., Saeid and Yuksel, S.B., Investigation of the moment-curvature relationship for reinforced concrete square columns. *Turkish Journal of Engineering*, Vol. 4, No. 1, 2020, 36-46.

- [16] Caglar, N., Demir, A., Ozturk, H. and Akkaya, A. (2015) - A simple formulation for effective flexural stiffness of circular reinforced concrete columns. *Engineering Applications of Artificial Intelligence* - Vol.38 - pp.79-87. DOI: 10.1016/j.engappai.2014.10.011
- [17] Mander JB, Priestley MJN, Park R. Theoretical stress-strain model for confined concrete, *Journal of Structural Engineering*; 1988.
- [18] TSDC 2007, Turkish earthquake design code for buildings, The Ministry of Environment and Urban, 2007.
- [19] EUROCODE-8. Design of structures for earthquake resistance - Part 1: General rules, seismic actions and rules for buildings. European Committee For Standardization; EN 1998-1:2003.
- [20] TBEC 2018, Turkish building earthquake code, The Ministry of Environment and Urban, 2018.
- [21] Xtract v.3.0. Cross-sectional X structural analysis of components, Imbsen Software Systems, 9912 Business Park Drive, Suite 130 Sacramento, CA 95827.
- [22] SAP2000 (2015) Integrated finite element analysis and design of structures basic analysis reference manual, Computers and Structures, Inc. California, USA



Flood Risk Analysis of Residential Areas at Downstream of the Elmali Dam

Farrokh Mahnamfar ^{1*}, Yasin Abdollahzadeh moradi ², Necati Ağırallıoğlu ³

¹ Sakarya University, Civil engineering Department, Sakarya, Turkey

² Istanbul Gelisim University, Faculty of Engineering and Architecture, Istanbul, Turkey

³ Antalya Bilim University, Civil engineering Department, Antalya, Turkey

Received: / Accepted: 30.12.2019 / 13.06.2020

Abstract

One of the natural disasters that hurts humankind is the flood. This disaster consists of climate change, geotechnical and topographic features in the region. Floods are usually influenced by the interaction of catchment-specific characteristics, such as meteorology, topography, geology and lately climate change. In addition, human activities increase flood risks. The most important causes of flood disasters in the world are uncontrolled urbanization activities and interventions in river beds near floodplains. Researchers have scientifically proven a sharp global increase in the economic risk associated with floods though flood-related fatalities might be decreasing.

The study area is located on the downstream side of the Elmali Dam built on the Goksu Creek in Beykoz District of Istanbul Province. In this study, the flood risk maps for floods that will be formed in Goksu Creek on the downstream side in the various discharge of the Elmali Dam spillway are prepared by modeling with 2D DHI MIKE 21 FM software. MIKE 21 Flow Model is a modeling system for 2D free surface flows. Also, the regions exposed to floods, the magnitude and risks of floods that will occur were evaluated with different scenarios. There were 4 scenarios in the study. As a result of the scenarios, the regions on the downstream side of the Elmali Dam are classified in terms of flood risk. The areas at risk are shown as flood maps. In the downstream area, the relation between flood flow and its area is observed linearly.

Key words: Flood, Risk analysis, Numerical model, MIKE 21.

1. Introduction

In Turkey and many countries, one of the major natural disasters which adversely affect their social and economic life such as people's life and property losses, is flood. Climatological-meteorological and geological-geomorphological features, vegetation and humanitarian interventions are among the main factors of the flood. The most important causes of flood disasters in the world are uncontrolled urbanization activities near to flood regions and interventions in river beds.

A deterministic approach is used by Mao et al. to calculate the hydraulic elements of the dam fracture. In addition, MIKE-21 dam breaking model is used to generate the hydraulic elements and generated hydraulic elements are integrated with a digital elevation model of the site downstream of the dam to map the possible affected areas. Simulation data and study results

* Corresponding Author,
Phone: +(90) 264 295 5740 e-mail: fmahnamfar@sakarya.edu.tr

can provide a socio-economic framework for downstream areas and a basis for emergency management of the dam reservoir [1].

The subject of dam flooding potential caused a prolonged flooding was considered by Diman & Tahir. Although floods are less likely to occur from dams, understanding the dam flood routing map can preserve the lives and property of downstream residents [2].

Dat et al. use a 1D and 2D model of MIKE FLOOD to simulate downstream flood of Tra Khuc-Song Ve River basin, including the breakdown of the DakDrinh. The establishment of DakDrinh flood map shows flood areas and depth of its downstream. Results obtained by Dat et al., make it possible for managers to create preventable plans and provide information to reduce disasters in vulnerable areas in the event of failure [3].

Mohd Sidek et al used the Clear Day scenario and Probable Maximum Flood scenario for dam break modeling. Flood area, flood duration and maximum flood depth in the downstream are obtained by the Mike Flood model. This result will lead to the identification of the affected location or villages located at downstream of the Susu Dam [4].

Although there is a decrease in flooding that occurs as a result of an increase in dam, ponds and stream rehabilitation works in Turkey, according to DSI data, from 860 floods occurred in the last 40 years, 660 deaths and 799,758 hectares of agricultural land have exposed to flood. Thus, the annual damage that has been caused in Turkey's economy is about 150 million Turkish Lira [5].

The biggest reason for the losses caused by the floods in Turkey occurs as a result of settlements closing the stream bed. In this case, it will inevitably overflow from its narrowed bed due to the increase in the flow rate resulting from heavy rain, and flood the settlement in front of it to reach the sea [6].

In another study, the risks of flooding that may arise from the Havran dam were taken into account. Risk analysis was carried out according to the flood return period of streams, flood scenarios that will occur with dam overflow and possible dam destruction. As a result, losses based on dam scenarios were found more destructive than other flood scenarios [7].

Abdollahzadehmoradi et al have numerically determined the flood risk of the downstream area of Samsun Mert River. Analyses were carried out according to various flood peak flows and according to risk situations, 8 different scenarios were performed with MIKE 11 software. As a result, it was observed that the streambed posed a risk in the 1000-year flood period. Thus, it was estimated that there would be a water depth of 1m from the upper level of the stream [8].

In this study, the study area is located on the downstream of Elmali Dam on Goksu Stream in Beykoz District of Istanbul Province. In this study, the flood risk maps for floods that will be formed in Goksu Creek on the downstream side in various discharge of the Elmali Dam spillway are prepared by modeling with 2D DHI MIKE 21 FM software. As a result of various simulations, risk areas on the downstream side of the Elmali Dam were identified.

2. The Study Area

Figure 1 shows the study area, which is located in Istanbul province, Beykoz district, Goksu Stream.

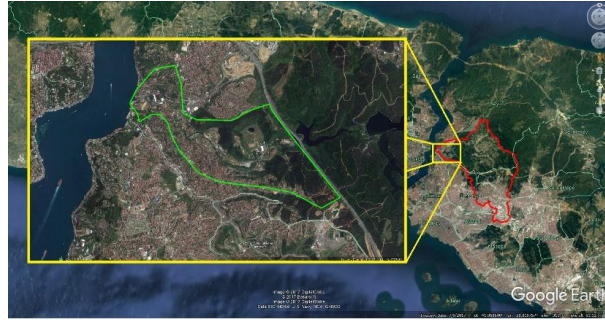


Figure 1. Study area

Flood risk analyses were made on the downstream side of the Elmali Dam. Elmali 2 Dam in 1955 and Elmali 1 Dam in 1907 have been started to operate. Elmali 1 Dam is located in Bogazici, 3.3 km southeast of Anadoluhisari and 1.2 km downstream of Elmali 2 Dam (Figure 2).



Figure 2. Plan of dam locations

The height of Elmali 1 Dam is 22 m from the foundation and its type is masonry. Type of Elmali 2 Dam is a buttress dam and height from the foundation is 49 m. The total drainage area of both dams is 81.5 km². The normal water levels of the Elmali 1 and Elmali 2 Dams are 32.40 m and 67.50 m, respectively [9, 10, 11]. The images and plans of Elmali 1 and Elmali 2 Dams are shown in figures 3 and 4.



(a)



(b)

Figure 3. Images of dams (a) Elmali 1 (b) Elmali 2

There are 3 spillways in Elmali 1 Dam, each of which is 3.75 m wide and at elevation of +31.00. In addition, there are 11 sliding spillways with a width of 4.30 m and a height of 2 m at the elevation of 29.00. Thus, Elmali 1 Dam has 14 spillways in total. The maximum flow capacity of the spillway is 540 m³/s [9].

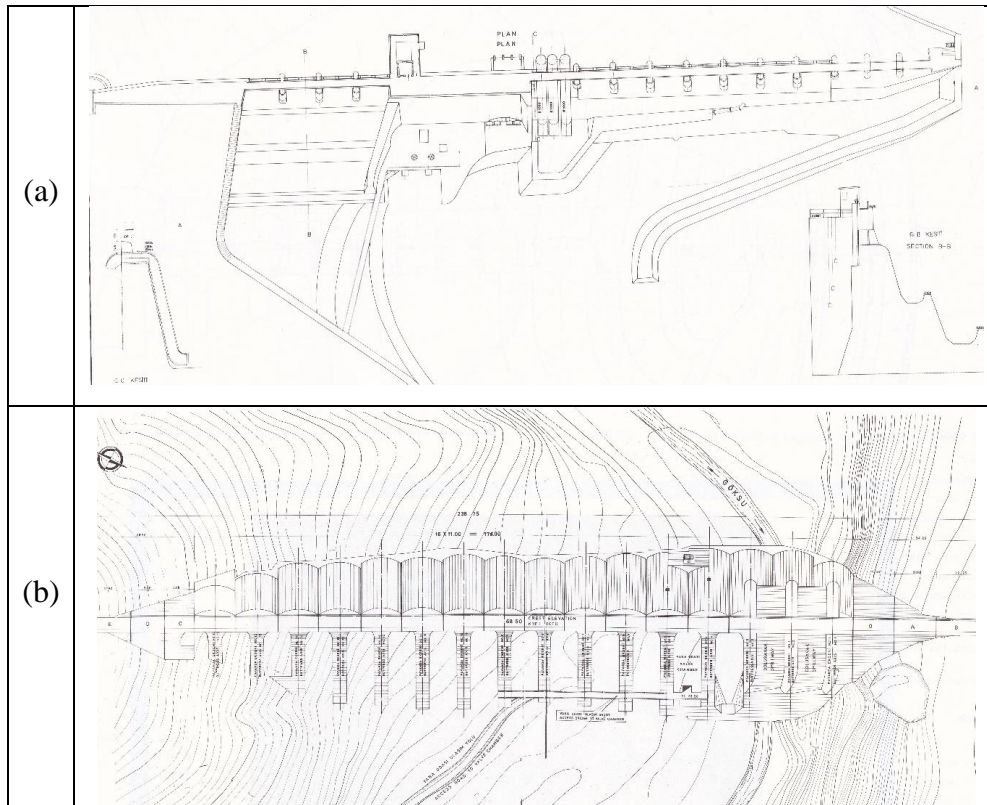


Figure 4. Plan images of dams (a) Elmali 1 (b) Elmali 2

3. Simulation Setup and Methods

In this study, the MIKE 21 FM numerical model based on the 2D Flexible Mesh approach, which is developed by the Danish Hydraulic Institute (DHI), was used as a hydrodynamic model. This model simulates the water level variations and flows velocities in response to a variety of forcing functions in a flood plain [12]. The model also includes continuity, momentum, temperature, salinity and density equations based on the numerical solution of two and three-dimensional Navier-Stokes equations with Boussinesq and hydrostatic pressure assumptions. The two-dimensional mesh consists of triangular or rectangular elements [13].

MIKE 21 Flow Model is one of the best software developed for numerical modeling of oceanographic conditions, coastal areas, river and water resources simulation. This model simulates two-dimensional flow, by using bathymetry, meteorological, tidal changes and other hydrographic conditions. Equations below represent the time-dependent, non-linear equations of continuity and conservation of momentum that solved by this model ($h=\eta+d$):

$$\frac{\partial h}{\partial t} + \frac{\partial hu}{\partial x} + \frac{\partial hv}{\partial y} = hS \tag{1.1}$$

$$\frac{\partial \bar{h}\bar{u}}{\partial t} + \frac{\partial \bar{h}\bar{u}^2}{\partial x} + \frac{\partial \bar{h}\bar{v}\bar{u}}{\partial y} = f\bar{v}\bar{h} - gh \frac{\partial \eta}{\partial x} - \frac{h}{\rho_0} \frac{\partial p_a}{\partial x} - \frac{gh^2}{2\rho_0} \frac{\partial \rho}{\partial x} + \frac{\tau_{sx}}{\rho_0} - \frac{\tau_{bx}}{\rho_0} - \frac{1}{\rho_0} \left(\frac{\partial s_{xx}}{\partial x} + \frac{\partial s_{xy}}{\partial y} \right) + \frac{\partial}{\partial x} (hT_{xx}) + \frac{\partial}{\partial y} (hT_{xy}) + hu_s S \tag{1.2}$$

$$\frac{\partial \bar{h}\bar{v}}{\partial t} + \frac{\partial \bar{h}\bar{v}^2}{\partial y} + \frac{\partial \bar{h}\bar{u}\bar{v}}{\partial x} = f\bar{u}\bar{h} - gh \frac{\partial \eta}{\partial y} - \frac{h}{\rho_0} \frac{\partial p_a}{\partial y} - \frac{gh^2}{2\rho_0} \frac{\partial \rho}{\partial y} + \frac{\tau_{sy}}{\rho_0} - \frac{\tau_{by}}{\rho_0} - \frac{1}{\rho_0} \left(\frac{\partial s_{yx}}{\partial x} + \frac{\partial s_{yy}}{\partial y} \right) + \frac{\partial}{\partial x} (hT_{xy}) + \frac{\partial}{\partial y} (hT_{yy}) + hv_s S \tag{1.3}$$

where t is time, x and y are spaces in cartesian coordinate system (m), η is water level variations (m), d is time-varying water depth (m), u is velocity component of x-direction (m/s), v is velocity component of y-direction (m/s), $f=2\Omega \sin\phi$ is Coriolis parameter (Ω (s⁻¹) is angular turnover, φ geographic latitude), g is the acceleration due to gravity (m/s²), ρ_w is the density of water, S_{xx}, S_{xy}, S_{yx} ve S_{yy} are radiation stress tensor component, P_a is atmospheric pressure (kg/m/s²), ρ₀ is reference specific mass of water, S point source discharge, u_s and v_s velocity (m/s), T_{ij} viscous, parameter including turbulence friction factors and differential transport, (τ_{sx}, τ_{sy}) ve (τ_{bx}, τ_{by}) x and y component of surface wind and floor friction stress, T temperature and S salinity [13].

In equations 1.1, 1.2 and 1.3, depth average velocity and T_{ij} values are calculated with the following equations:

$$h\bar{u} = \int_{-d}^{\eta} u dz, \quad h\bar{v} = \int_{-d}^{\eta} v dz, \quad T_{xx} = 2A \frac{\partial \bar{u}}{\partial x}, \quad T_{xy} = A \left(\frac{\partial \bar{u}}{\partial y} + \frac{\partial \bar{v}}{\partial x} \right), \quad T_{yy} = 2A \frac{\partial \bar{v}}{\partial y}$$

The mesh used in the study area is shown in Figure 5. As can be seen in Figure 5, a triangular and rectangular calculation meshes are used to include all the buildings in the study area. The number of mesh elements is 32766. As the boundary conditions, the flow values shown in Table 1 were used respectively, on the upstream (Output of the Elmali-1 Dam) for 60 minutes. Since the stream is poured into the sea (Bosporus), the seawater level value is accepted as zero. Simulated flood maps obtained the maximum depth of water at each node of the mesh.

In this study, floods caused by the Elmali 1 Dam were investigated and risky areas were identified. The percentage of the maximum overflow discharge from the spillway of the dam was used in flood risk analysis. Flood risk maps for various scenarios were created with MIKE 21 FM. There were 4 scenarios for Goksu creek and the results of the scenarios are shown in Figures 10, 11, 12 and 13. Also in Figure 14, Figures 10, 11, 12 and 13 are shown as a unified map.



Figure 5. Implemented mesh in the study area

In the first scenario, the flood map is created when 25% of the maximum capacity of the spillway is discharged. Then, flood maps consisting of 50%, 75% and 100% of the maximum capacity of the spillway were obtained. Spillway discharge and duration are given in Table 1. The maximum capacity of the spillway (Q_{max}) is $540 \text{ m}^3/\text{s}$. In all scenarios, the effect of the buildings in the Goksu stream is also reflected in the models. Thus, the effect of urbanization on flood progression is also included in the model. The buildings are shown in Figure 5 in red color.

Table 1. Flood scenarios

Scenario No.	The percentage of spillway discharge capacity	Discharge capacity of spillway (m^3/s)	Discharge duration (min)
1	%25	135	60
2	%50	270	60
3	%75	405	60
4	%100	540	60

Flood areas are classified according to 3 critical depths, 0.6, 1.0 and 3.5 m. The basis for the selection of critical depths is described as follows: In general, the height of schools and public buildings is 0.6 m from the ground. If the flood depth is more than 1.0 m, there is a possibility of loss of life. In addition, great damage is expected in agricultural production. The minimum height of sills for shelters and also for one-story buildings is usually 3.5 m. The classification of hazards according to the flood depth is given in Table 2 [14].

Table 2. Flood risk type

Flood hazard No.	Depth of flooding, d, (m)	Type of flood hazard
H ₁	$0.0 < d < 0.6$	Low
H ₂	$0.6 < d < 1.0$	Medium
H ₃	$1.0 < d < 3.5$	High
H ₄	$3.5 < d$	Extreme

In the first scenario, the flood map that will occur in the downstream of the dam is presented in Figure 6 when 25% of the maximum capacity of the spillway discharged. In Figure 6, the impact of urbanization on the flood direction and residential areas exposed to the flood are clearly understood. Also, the depth of the water reaches up to 4 m in some parts of the middle part of the stream bed. Flood is spread more in the region where the stream connects to the sea, creating large-scale risky areas. Here, the depth of water has increased up to 1.2 m in residential areas.

If there is agricultural land where the stream is connected to the sea, it is expected that this land will be damaged in case of a possible flood.

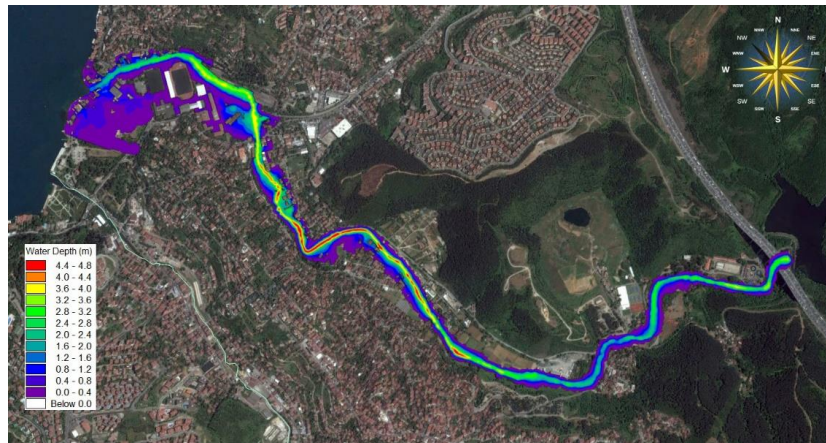


Figure 6. Flood risk map of the first scenario ($0.25Q_{max}$)

As a result of the second scenario, at points 1, 2, 3 and 4 shown in Figure 7, the flood stream bed was spread more to the surrounding land. In Scenario 2, the depth of the water in the surrounding land was more than 1 m, and in the event of a flood, there is a possibility of a loss of life and property. At point 4, flood water depth reaches up to 3 m.

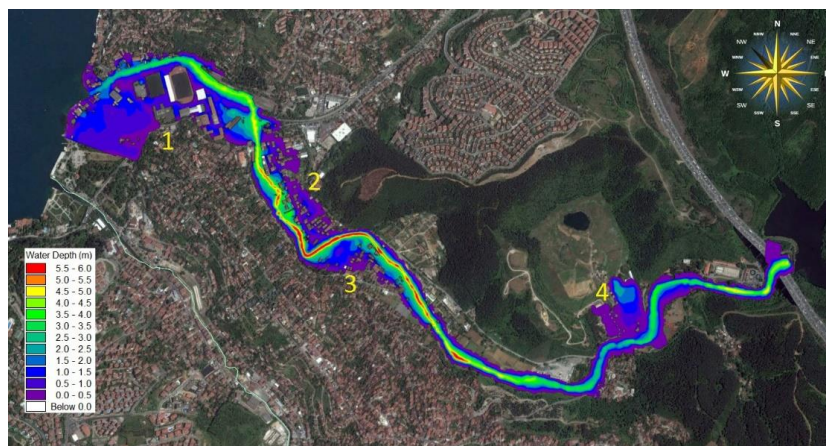


Figure 7. Flood risk map of the second scenario ($0.50Q_{max}$)

In the third scenario, flood flow is taken as $405 \text{ m}^3/\text{s}$ and this flow is equal to 75% of the maximum discharge capacity of the spillway. In this scenario, there is a 25% flow increase compared to the previous scenario. In Figure 8, when the MIKE 21 FM model is run with a flood flow of $405 \text{ m}^3/\text{h}$, the areas at risk increased as expected. When we compare it with the previous scenario, it was observed that the water depth at point 1 reached up to 2 m, and as seen in Figure 8, most of the buildings were located in the risky area. According to the result obtained from this scenario, the most dangerous area is the region marked with 3, so that the water depth has increased up to 3 meters. Based on this result, this region has been determined as H_3 according to the risk category.

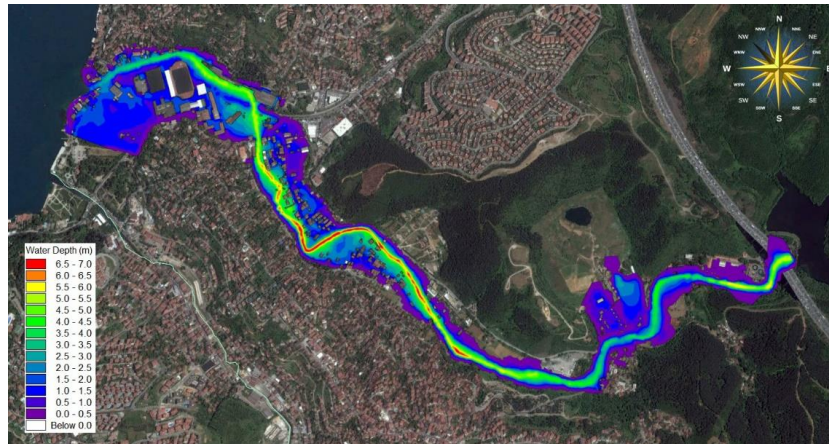


Figure 8. Flood risk map of the third scenario ($0.75Q_{max}$)

Considering the most recent scenario (Figure 9) and the most hazardous situation, there is no obvious difference in the lower parts of the stream (towards the sea) with Scenario 3, and only a slight increase in the flood depth has occurred. Considering the results of scenario 4 and 3 in the upper areas of the stream (Output of dam), the flood was spread more to the surrounding area in scenario 4 and the facility areas at the output of the dam were completely submerged (point 5).

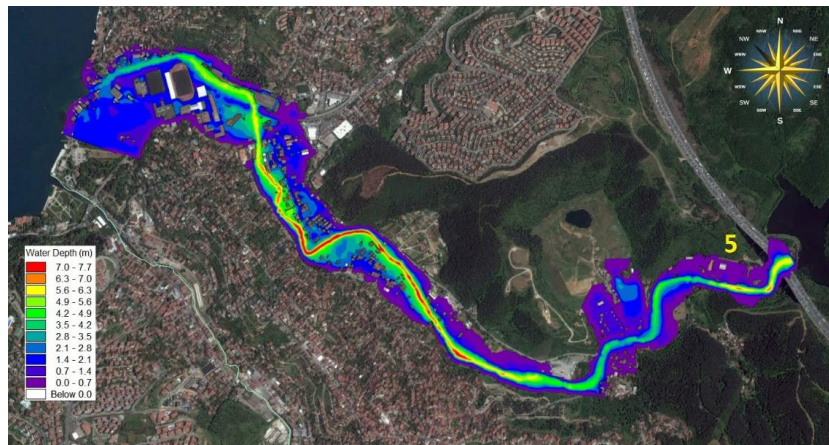


Figure 9. Flood risk map of the fourth scenario (Q_{max})

Finally, Figure 10 shows the flood map of the four Scenarios. In this map, red, orange, yellow and green areas are maps obtained from scenarios 1, 2, 3 and 4, respectively, and show the areas exposed to flooding. In the first scenario, the area exposed to floods is 0.453 km^2 . In the event of a possible flood, the buildings in this area are urban areas that are always at risk and can be damaged.

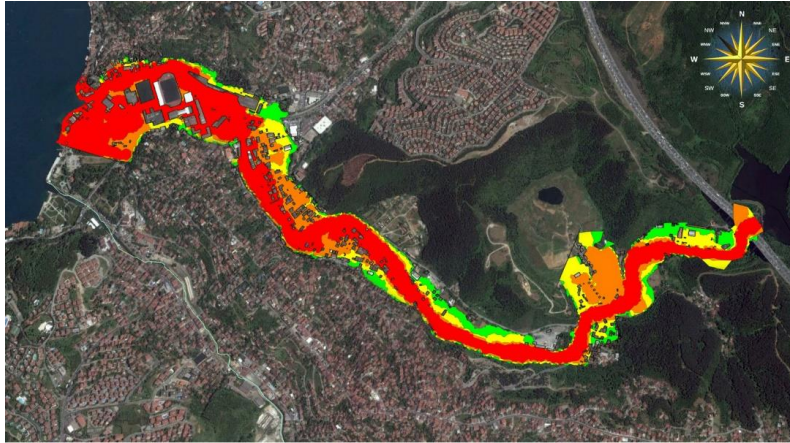


Figure 10. Unified map of four scenarios' result

The results of the second scenario are shown with orange and the area exposed to flood is 0.605 km². In this scenario, the maximum water depth created by the flood is 6 m. The areas of floods in the third (yellow) and fourth (green) scenarios are 0.732 km² and 0.820 km², respectively.

4. Conclusions and Recommendations

In this study, the floods that may occur in the Goksu stream originating from the operation of the spillway of the Elmali dam were investigated. In other words, the flood, which can occur in accordance with the operational plan of the spillway of the Elmali dam, has been investigated with a numerical model. In this study, 4 scenarios are taken into consideration. Thus, flood maps, formed by 25%, 50%, 75% and 100% of the maximum discharge capacity of the spillway, were obtained and risky areas were determined.

Areas exposed to flooding are divided into three critical depths, 0.6, 1.0 and 3.5 m. These ranges are classified into 4 groups as 0-0.6 m depth low risk zone, 0.6-1.0 m depth medium risk zone, 1.0-3.5 m depth high risk zone, and regions with more than 3.5m depth are extreme risk zone. In the First Scenario, the flood is spreading more frequently in the region where the stream is connected to the sea and constitutes high risky areas. If there are agricultural lands where the stream is connected to the sea, possible floods are expected to cause great damage to this land. In the second scenario, the flood streambed is spreading more to the surrounding land and in the event of a flood, there is a high probability of loss of life and property.

In the Third Scenario, there is a 25% discharge flow increase compared to the previous scenario and the flood flow is taken as 405 m³/s. The most hazardous region of this scenario is point 3 and is located in overly risky areas according to the flood risk type. When the last scenario with the third scenario are compared, it is seen that there is no significant difference in the flood area (towards the sea) in the downstream areas of the stream. In addition, in the upper areas of the creek (point 5 in figure 9), the areas exposed to flooding in Scenario 4, cover more land than scenario 3, and it is likely that the flood may affect dam facilities. In Figure 10, the regions where the four scenarios are exposed are shown in various colors. In this figure, red, orange, yellow and green areas are flood maps obtained from scenarios 1, 2, 3 and 4, respectively.

Dams are important structures for flood control. Although floods are less likely to occur from dams, determination of the dam flood map can protect the lives and properties of downstream residents. In the study, hazardous areas exposed to flood were determined in the case of various discharge flows from the spillway of the Elmali 1 Dam. In addition, some suggestions have been made to reduce flood damages. Thus, it is important that the dam reservoir is emptied in a controlled manner when floods can occur. One of the preventions that has been taken in this direction is the controlled structuring of urbanization in risky areas and urbanization activities

should not be allowed in H₂, H₃ and H₄ situations. In the current urbanization situation, by using high-tech communication devices, inhabitants should be informed about the immediate evacuation quickly. Another precaution during the flood that can be taken is to quickly discharge any obstacles that reduce the discharge capacity of the creek, for example, existing boats at the port of the sea.

References

- [1] Mao, J.; Wang, S.; Ni, J.; Xi, C.; Wang, J., (2017), Management System for Dam-Break Hazard Mapping in a Complex Basin Environment, *ISPRS Int. J. Geo-Inf.*, 6, 162.
- [2] Diman, C. P., & Tahir, W. (2012). Dam flooding caused a prolonged flooding. *International Journal of Civil & Environmental Engineering*, 12(6), 71-75.
- [3] Dat, T. T., Tri, D. Q., Truong, D. D., & Hoa, N. N. (2018), Application of Mike Flood Model in Inundation Simulation with the Dam-break Scenarios: a Case Study of DakDrinh Reservoir in Vietnam. *Inter. J. Earth. Sci. Eng.(SCOPUS, Q4)*.
- [4] Mohd Sidek, L., MOHD SHAH, MOHD. RASHID., Yalit, R., PONRAJ, MOHANADOSS., & Basri, H. (2017). Hydrodynamic Numerical Modelling Of Dam Failure and Impacts Assessment of Susu Dam With Mike, *E-proceedings of the 37 th IAHR World Congress*, Kuala Lumpur.
- [5] DSİ, (2013), “Water resources development working group report” *forestry and water council*, 12 March. (In Turkish)
- [6] Özcan O., Musaoglu N., Seker D.Z., Tanik A. (2008), Determination of flood risk in Sakarya sub basin using remotely sensed data and GIS, *Fresenius Environmental Bulletin*, 17(11b), 1964-1971.
- [7] Özdemir, H., (2007). Flood risk analysis according to various scenarios: The Case of Havran creek. *Proceedings book of TMMOB disaster symposium*, Balikesir, Turkey. (In Turkish)
- [8] Abdollahzadehmoradi, Y., Erdik, T., Mahnamhar, F., Özger, M., Altunkaynak, A., (2013). “Determination of the flooding risk in the slum areas of ÇAY district, İLKADIM County of SAMSUN province.” *Flood and Landslide Symposium*, Trabzon, Turkey. (In Turkish)
- [9] Ağırlioğlu, N., Altunkaynak, A., Özger, M., (2015), “Elmali - I and II dams engineering studies technical report” İSKİ. (In Turkish)
- [10] Ural, O.M. and Urgan, Ü., (1967) Large Dams in Turkey, DSİ.
- [11] Orhon, M., Esendal, S., Kazak M.A., (1991), Dams in Turkey, DSİ general directorate.
- [12] Kadama, P. and Sen, D., (2012). Flood inundation simulation in Ajoy River using MIKE-FLOOD, *ISH Journal of Hydraulic Engineering*, Vol. 18, No. 2, June 2012, 129–141.
- [13] DHI, 2010. MIKE 21 & MIKE 3 Flow Model FM. Hydrodynamic and Transport Module Scientific Documentation, Release 2010, (D.H.I). *Danish Hydraulic Institute*.
- [14] Tingsanchali, T., ve Karim, M.F. (2005), “Flood Hazard and Risk Analysis in the Southwest Region of Bangladesh”, *Hydrological Processes*, 19, 2055-2069.